

Electronic Thesis and Dissertation Repository

6-3-2021 10:00 AM

Rapid Recovery Of Cerebral Blood Content And Oxygenation In Adults From Time-Resolved Near-Infrared Spectroscopy

David J. F. Cohen, *The University of Western Ontario*

Supervisor: Diop, Mamadou, *Lawson Health Research Institute and University of Western Ontario*

A thesis submitted in partial fulfillment of the requirements for the Master of Science degree in Medical Biophysics

© David J. F. Cohen 2021

Follow this and additional works at: <https://ir.lib.uwo.ca/etd>



Part of the [Investigative Techniques Commons](#)

Recommended Citation

Cohen, David J. F., "Rapid Recovery Of Cerebral Blood Content And Oxygenation In Adults From Time-Resolved Near-Infrared Spectroscopy" (2021). *Electronic Thesis and Dissertation Repository*. 7841. <https://ir.lib.uwo.ca/etd/7841>

This Dissertation/Thesis is brought to you for free and open access by Scholarship@Western. It has been accepted for inclusion in Electronic Thesis and Dissertation Repository by an authorized administrator of Scholarship@Western. For more information, please contact wlsadmin@uwo.ca.

Abstract

Patient neurological outcomes following cardiac surgery are improved when near-infrared spectroscopy (NIRS) is used to optimize intraoperative cerebral oxygen delivery. However, current NIRS analysis methods have difficulties monitoring adult brains due to contamination from the extracerebral layer (ECL).

The objective of this thesis is to develop a time-resolved (TR) NIRS data analysis method for monitoring adult cerebral oxygen saturation (ScO₂) and total hemoglobin (HbT) by assuming the head is composed of two layers – the ECL and the brain. We tested the validity of this assumption using *in silico* data from an adult human head using two approaches; a few-wavelength, single detector method, and a hyperspectral, two-detector method that does not require prior knowledge of exact ECL thickness. Both methods were able to recover ScO₂ and HbT with mean percent differences below 3%. Additionally, the hyperspectral method requires only 0.22 seconds per measurement, enabling quasi-real-time adult neuromonitoring.

Keywords

Near-infrared spectroscopy, Time-resolved near-infrared spectroscopy, Two-layer diffusion approximation, Monte Carlo, Cerebral Oxygen Saturation, Hemoglobin, Oxyhemoglobin, Deoxyhemoglobin, Brain, Adult, Hyperspectral

Summary for Lay Audience

Cardiac surgery is associated with high incidence of brain injury during and after the operation, occurring in approximately 6% of patients. These injuries include stroke, seizures, and other types of brain damage, and can have lasting impacts on patient quality of life. There is growing evidence that patient neurological outcomes are improved when near-infrared spectroscopy (NIRS) is used to optimize cerebral oxygen delivery during the operation. NIRS uses near-infrared light to non-invasively monitor brain health by measuring cerebral oxygen saturation (ScO_2) and total hemoglobin concentration (HbT). However, current NIRS analysis methods have difficulties monitoring adult brains due to contamination from the scalp, skull, and cerebrospinal fluid, collectively referred to as the extracerebral layers (ECL).

The objective of this thesis is to develop a time-resolved (TR) NIRS data analysis method for monitoring adult ScO_2 and HbT by assuming the head is composed of two layers – the ECL and the brain. A TR-NIRS system releases pulses of light into the tissue and records how long the light takes to reach a detector. The detected light is then analyzed to measure the physiological parameters of interest. We tested the validity of the two-layer assumption using simulated data of light transport in an adult human head using two approaches. The approaches differ primarily in two ways: the number of wavelengths of light used, and the number of detectors. The first approach uses data from a single source-detector pair at four wavelengths to estimate ScO_2 and HbT with a mean percent difference of 2.3% and 2.9%, respectively. The second method recovers the same parameters from 150 wavelengths (referred to as hyperspectral) and uses two detectors. The added information provided by using more wavelengths and a second detector allows the hyperspectral method to estimate the thickness of the ECL, making it more versatile. The accuracy of the hyperspectral method is comparable to the few-wavelength alternative, recovering ScO_2 and HbT with mean percent differences of 2.4% each. The hyperspectral method can analyze TR-NIRS data in near-real-time, requiring only 0.22 seconds per measurement, which is a major step towards real-time monitoring of the brain during cardiac surgery.

Co-Authorship Statement

Chapter 2 of this thesis is adapted from a published proceeding paper, while Chapter 3 is an unpublished journal article currently being prepared for submission. As the first author on both articles, I contributed significantly to all aspects of the work, including study design, data generation, analysis, interpretation of results, and preparation of the manuscripts. As my supervisor and the primary investigator, Dr. Mamadou Diop oversaw and provided support for each study from conception to completion, providing his expertise where necessary. Dr. Diop also secured funding for both studies, aided with interpretation of the results, and edited the manuscripts and approved them for publication. Both of the following manuscripts include a list of co-authors that contributed significantly to the work, and their individual contributions are listed for their respective chapters below.

Chapter 2 is adapted from a proceeding paper titled: “Estimating adult cerebral oxygen saturation from time-resolved near-infrared spectroscopy measurements with few discrete wavelengths at a single source-detector distance” published in *Proceedings Volume 11639, Optical Tomography and Spectroscopy of Tissue XIV* in 2021 by David Jonathan Fulop Cohen, Natalie C. Li, and Mamadou Diop. Natalie C. Li aided in the development of the data analysis method. Natalie C. Li and Mamadou Diop both edited the manuscript and approved it for submission.

Chapter 3 is an unpublished work titled “Fast Estimation of Adult Cerebral Oxygen Saturation and Total Hemoglobin using Hyperspectral Time-Resolved Near-Infrared Spectroscopy” by David Jonathan Fulop Cohen, Natalie C. Li, Seva Ioussoufovitch, Vladislav Toronov, and Mamadou Diop. Natalie C. Li aided in the development of the late-photon analysis method and in editing the manuscript. Seva Ioussoufovitch and Vladislav Toronov aided in the development of the two-layer hyperspectral time-resolved analysis method. Mamadou Diop was involved throughout the work from data generation to analysis and edited the manuscript.

Dedication

I would like to dedicate this thesis first and foremost to my family for their constant love and support. To my mom and dad, Addrienne Fulop and Sam Cohen, thank you for always supporting me in every manner that you can. Your love, support, and encouragement have been key in keeping me motivated throughout my Masters, and throughout my life. I could not have gotten to where I am now without you both guiding me along the way. I would especially like to thank my mom for all the editing she has done throughout my graduate and undergraduate degrees; she can probably explain my research as well as I can at this point.

To my sister, Mackenzie Cohen, thank you for making me laugh constantly and supporting me in anyway you can. You are my biggest cheerleader, and I appreciate your support more than I can ever express.

To my Bubbie, Papa, and Papi (Mariam and Ignatz Fulop and Maurice Cohen), thank you for being such amazing grandparents and supporting me throughout my journey, and praying for my success. To my late Mémé (Fortune Cohen), thank you for looking out for me. I would like to think you would be proud of everything I have accomplished. May your memory be a blessing.

To my martial arts instructor, Guru Pak Chan, thank you for teaching me the dedication and perseverance required to be successful. I will always remember the first lesson you taught me, “It takes 30 days to make a habit, but only 3 days to break it.” Your guidance and support throughout the years has been valuable beyond measure.

Finally, to my many friends and family who have given me a home away from home. The memories and experiences I have made with you will last me a lifetime. I dedicate this work to you all.

Acknowledgments

I am eternally grateful for all the help, mentorship, and support I have received over the years from the many people at Western University. The work in this thesis would not have been possible without each and every one of you.

First off, I want to thank my supervisor and mentor, Dr. Mamadou Diop. Joining your lab for my third-year undergraduate research project was one of the best decisions I have ever made. You are not only an incredible researcher and mentor, but an amazing leader as well. None of the scholarships, conference presentations, or awards I have received would have been possible without your invaluable input and guidance. Thank you for introducing me to the world of biomedical optics, research, and scientific writing. I truly appreciate the countless hours you have put into improving my writing and pushing me to achieve my goals.

I would also like to thank my lab-mate and good friend Seva Ioussoufovitch for being my constant sounding board over the past 4 years. Thank you for patiently listening to me complain about how my code is not working during the hundreds of hours we spent in the lab together and offering useful feedback where appropriate. You have helped to show me how exciting research can be, even when it's not going perfectly.

To my lab-mate and friend Natalie Li, thank you for listening to my ideas for the late-photon analysis method. The brain storming conversations we have had on the topic helped develop the method into what it is today.

This thesis would not have gotten written if not for Laura Mawdsley. The hours we spent on Zoom keeping each other on track are entirely responsible for this thesis being written in any reasonable amount of time. You managed to make what is usually a very difficult and time-consuming experience into an entertaining one.

I would like to thank Lawrence Yip and Drs. Ajay Rajaram, Daniel Milej, and Androu Abdalmalak for their input and guidance over the years for my various projects. Your feedback has helped me become a better presenter and taught me how to formulate more complete answers.

To my committee members, Drs. Keith St. Lawrence and Ali Khan, thank you for taking the time to help point my project in the right direction. Your guidance and insight helped ensure this project stayed on track and within scope.

To Dr. Vladislav Toronov, thank you for your input into how to code the two-layer time-resolved analytical model. The insights and code you provided saved me several months of work and effort, and I am extremely grateful for it.

This acknowledgement section would be incomplete without thanking the incredible administrative staff from the Department of Medical Biophysics (Jennifer Devlin, Kathleen Petts, and Kathleen Mendelson). I deeply appreciate all the help and kindness you have provided me since becoming a student in the department in the third year of my undergraduate degree. I am also grateful to Dr. Daniel Goldman for providing me the opportunity to be the teaching assistant for MEDBIO 3507. The leadership and teaching experience has been a valuable experience for me and helped me better develop my ability to communicate complex topics in understandable ways.

Finally, I would like to thank the following sources of funding, without which this work would not have been possible: Natural Sciences and Engineering Council (NSERC), Queen Elizabeth II Graduate Scholarship in Science and Technology (QEII-GSST), the Lawson Health Research Institute, Western University, Schulich School of Medicine and Dentistry, and the Department of Medical Biophysics.

Table of Contents

Abstract.....	ii
Summary for Lay Audience.....	iv
Co-Authorship Statement.....	v
Dedication.....	vi
Acknowledgments.....	vii
Table of Contents.....	ix
List of Tables.....	xii
List of Figures.....	xiii
List of Appendices.....	xvi
List of Abbreviations.....	xvii
Chapter 1.....	1
1 Introduction.....	1
1.1 Clinical Motivation.....	1
1.1.1 Brain Injury during cardiac surgery.....	1
1.1.2 Current Methods of Detecting Brain Injury.....	3
1.2 Near-Infrared Spectroscopy.....	4
1.2.1 Background and Uses.....	4
1.2.2 Optical Properties.....	5
1.2.3 Tissue Optical Properties.....	6
1.2.4 Beer-Lambert Law.....	12
1.2.5 Diffusion Approximation.....	14
1.2.6 Blood, Oxygen, and the Brain.....	18
1.3 Continuous-wave NIRS.....	20
1.4 Time-Resolved NIRS.....	21

1.4.1	General Theory and Uses.....	21
1.4.2	Multi-spectral and Hyperspectral TR-NIRS	23
1.5	Research Objectives.....	24
1.6	Monte-Carlo Simulations.....	24
1.7	Thesis Outline	25
1.7.1	Chapter 2: Estimating adult cerebral oxygen saturation from time-resolved near-infrared spectroscopy measurements with few discrete wavelengths at a single source-detector distance	25
1.7.2	Chapter 3: Fast Estimation of Adult Cerebral Oxygen Saturation and Total Hemoglobin using Hyperspectral Time-Resolved Near-Infrared Spectroscopy	26
1.7.3	Chapter 4: Conclusion and Future Work	26
	References	27
	Chapter 2.....	44
2	Estimating adult cerebral oxygen saturation from time-resolved near-infrared spectroscopy measurements with few discrete wavelengths at a single source-detector distance.....	44
2.1	Abstract.....	44
2.2	Introduction.....	45
2.3	Methods.....	46
2.3.1	Monte Carlo Simulations	46
2.3.2	Data Analysis	47
2.4	Results.....	49
2.4.1	Simulations	49
2.4.2	Data analysis	49
2.5	Discussion.....	52
2.6	Conclusion	54
2.7	Acknowledgements.....	54
2.8	References.....	55

Chapter 3.....	58
3 Fast Estimation of Adult Cerebral Oxygen Saturation and Total Hemoglobin using Hyperspectral Time-Resolved Near-Infrared Spectroscopy	58
3.1 Introduction.....	58
3.2 Methods.....	60
3.2.1 Phase 1: Estimation of baseline chromophore concentrations.....	61
3.2.2 Phase 2: Rapid Cerebral Concentration Recovery	65
3.2.3 Validation.....	66
3.3 Results.....	68
3.3.1 Phase 1: Baseline chromophore concentrations.....	68
3.3.2 Phase 2: Active Monitoring	71
3.4 Discussion and Conclusion	72
3.5 References	76
Chapter 4.....	81
4 Conclusion	81
4.1 Research Objectives.....	81
4.2 Summary of Chapters	83
4.2.1 Chapter 2: Estimating adult cerebral oxygen saturation from time-resolved near-infrared spectroscopy measurements with few discrete wavelengths at a single source-detector distance	83
4.2.2 Chapter 3: Fast Estimation of Adult Cerebral Oxygen Saturation and Total Hemoglobin using Hyperspectral Time-Resolved Near-Infrared Spectroscopy	83
4.3 Limitations	84
4.4 Future Work	85
4.5 Conclusion	85
4.6 References.....	87
Appendices.....	92

List of Tables

Table 1.1: Anisotropic Factor and Refractive Index of Tissues	7
Table 1.2: The values for the scattering coefficients at 500 nm (a) for Scalp, Skull, and Brain tissue, and their respective scattering powers (b).	8

List of Figures

Figure 1.1: Wavelength Dependent Scattering Coefficients. For the scalp, skull, and brain, the values are found using Eq 1.2 and the values from Table 1.2 for every wavelength between 650 nm and 950 nm. For the cerebrospinal fluid, the values were assumed to be 0.0001 mm^{-1} for every wavelength.	8
Figure 1.2: Sample absorption spectra of the four tissue types that compose the head. The brain spectrum (yellow) is for a brain containing $55 \mu\text{M}$ of hemoglobin with 70% ScO_2 , and 80% water.	9
Figure 1.3: Extinction coefficient spectra of water on the right axis and oxy- and deoxyhemoglobin on the left axis.	10
Figure 1.4: Sample absorption coefficient (μa) spectra for brain tissue depending on the concentrations of oxy- (HbO_2) and deoxyhemoglobin (Hb). The total hemoglobin is equal to $55 \mu\text{Mol}$ in each spectrum, meaning the differences in the curves are due to the proportions of oxy- and deoxyhemoglobin.	12
Figure 1.5: A) Transmittance: The source (red) and detector (green) are on opposite faces of the tissue. B) Reflectance: The source (red) and detector (green) are on the same face of the tissue.	15
Figure 1.6: The one- and two-layer solutions to the diffusion approximation (DA). Optical properties in both layers of the two-layer solution are the same for a direct comparison to the homogeneous semi-infinite solution. Absorption is 0.0161 mm^{-1} , reduced scattering coefficient is 0.840 mm^{-1} , and the refractive index is assumed to be 1.4.	18
Figure 1.7: Late-photon analysis. The log of the time-of-flight curve approaches a linear slope as time increases. The region in red corresponds with the late-arriving photons and provides sufficient signal-to-noise ratio for analysis in an <i>in vivo</i> setting. The dotted black line is a linear fitting of the region of interest, and its slope is equal to the denominator of the right part of Eq. 1.22 and is related to the absorption coefficient of the medium.	23

Figure 2.1: Four-layer adult head model used for the Monte Carlo simulations: A) full head model and B) cross-section along the source-detector plane. The four layers are the scalp (dark blue), skull (cyan), cerebrospinal fluid (orange), and brain tissue (yellow). Though the full head was segmented, only the portion shown in colour was used in the simulations due to GPU memory limitations. The source (red star) and the detector (green star) are located 3 cm apart..... 47

Figure 2.2: Recovered cerebral oxy- (A) and deoxyhemoglobin (B) concentrations for each ScO₂. The values plotted in blue are the recovered values, while the dotted black line represents the inputted concentrations. (C) and (D) show the percent differences between the recovered concentrations and the simulated values..... 51

Figure 2.3: Recovered ScO₂ (A) and total hemoglobin concentration (B) for each simulated ScO₂. In both cases, the mean and standard deviation values are calculated across skin oxygenation, for each inputted ScO₂. The recovered values are plotted in blue, while the dotted black line represents the true values. (C) and (D) show the percent differences between the recovered values and the ground truth..... 52

Figure 3.1: Flowchart of the two-phase hyperspectral TR-NIRS algorithm: Phase 1 revolves around the recovery of the absolute chromophore concentrations in the deep tissue (brain) using a two-layer analytical model of light transport in diffuse media. Phase 2 uses the absolute concentrations, estimated from Phase 1, to correct for the contribution of the ECL to late-arriving photon (from the tail of the TPSFs), allowing for quasi-real-time monitoring of cerebral blood content and oxygenation. 60

Figure 3.2: The outputs of the three rounds of homogenous fitting on the absorption (A) and scattering (B) coefficients. 62

Figure 3.3: Adult head with source (red) and detectors (purple). The detectors are 2 cm and 3 cm away from the source. The tissues shown are skin (dark blue), skull (light blue), cerebrospinal fluid (orange), and brain (yellow). Due to GPU limitations, only the right upper octant of the head was simulated, as shown above (grey tissues not simulated). The voxel size in the model is 1 mm³. 67

Figure 3.4: A) Recovered absorption coefficient from the 40%, 50%, 60%, and 70% brain oxygen saturations with skin oxygen saturation set to 70% and the true (inputted) values. B) Recovered and true (inputted) absorption coefficient spectra from 50%, 60%, and 70% skin oxygen saturation at 70% brain oxygen saturation. 69

Figure 3.5: Results from Phase 1; for every cerebral oxygen saturation, three skin saturations were evaluated. A) The recovered brain SO_2 , B) recovered oxyhemoglobin, C) recovered deoxyhemoglobin, and D) recovered total hemoglobin plotted versus the inputted ScO_2 . The dotted black lines are the expected values. E) The recovered top layer thickness versus the inputted ScO_2 . The true thickness of the ECL is approximately 12 mm. F) and G) show the percent difference for SO_2 and total hemoglobin. 70

Figure 3.6: Results from Phase 1 with known ECL thickness; for every cerebral oxygen saturation, three skin saturations were evaluated. A) The recovered brain SO_2 , B) recovered oxyhemoglobin, C) recovered deoxyhemoglobin, and D) recovered total hemoglobin plotted versus the inputted ScO_2 . The dotted black lines are the expected values. E) and F) show the percent difference for SO_2 and total hemoglobin. 71

Figure 3.7: Results of Phase 2 analysis when using the concentrations estimated from Phase 1 for brain and skin oxygen saturation at 70%. A) The recovered brain ScO_2 , B) recovered oxyhemoglobin, C) recovered deoxyhemoglobin, and D) recovered total hemoglobin plotted versus the inputted ScO_2 . The dotted black lines are the expected values. 72

List of Appendices

Appendix A: Permission for Reproduction of Scientific Articles	92
Appendix B: Curriculum Vitae.....	93

List of Abbreviations

a	Scattering coefficient at 500 nm
A	Attenuation
b	Scattering power
CABG	Coronary artery bypass graft
CCO	Cytochrome C Oxidase
CSF	Cerebrospinal fluid
CT	Computed tomography
CW	Continuous-wave
CW-NIRS	Continuous-wave near-infrared spectroscopy
DA	Diffusion approximation
DTOF	Distribution Time of Flight
DWI	Diffusion-weighted imaging
ECL	Extracerebral layer
EEG	Electroencephalogram
GPU	Graphics Processing Unit
Hb	Deoxyhemoglobin
HbO ₂	Oxyhemoglobin

HbT	Total Hemoglobin
IRF	Instrument Response Function
MCX	Monte Carlo Extreme
MRI	Magnetic resonance imaging
n	Refractive Index
NIRS	Near-infrared spectroscopy
OR	Operating room
RTE	Radiative Transfer Equation
ScO ₂	Cerebral oxygen saturation
SO ₂	Blood oxygen saturation
TCD	Transcranial Doppler ultrasound
TIA	Transient ischemic attack
TPSF	Temporal Point-Spread Function
TR	Time-resolved
TR-NIRS	Time-resolved near-infrared Spectroscopy
WF	Water fraction
λ	Wavelength
Φ	Fluence rate
C	Concentration

R	Reflectance rate
g	Anisotropic factor
t	time
v	Speed of light in a medium
ε	Molar extinction coefficient
μ'_s	Reduced scattering coefficient
μ_a	Absorption coefficient
μ_s	Scattering coefficient

Chapter 1

1 Introduction

A core tenet of medicine is the concept of non-maleficence; do no harm. Physicians weigh the risks and benefits of each course of treatment, ensuring it is the right option for their patient. One of these crucial decisions is if a patient should undergo cardiac surgery. Despite surgery being necessary to correct many heart conditions, it carries with it a high risk of neurological injury. There is growing evidence that continuous intraoperative neuromonitoring is needed to detect cerebral complications as they occur, allowing physicians to provide early medical intervention. Near-infrared spectroscopy (NIRS) is a promising optical spectroscopy technique to accomplish just that. However, the majority of NIRS neuromonitoring methods have low brain sensitivity in adult populations; the population where they are often most needed.

This introductory chapter provides the background knowledge required to understand the NIRS neuromonitoring methods developed throughout this thesis. It starts by providing an understanding of the clinical need for adult neuromonitoring during cardiac surgery, the neuromonitoring methods currently available, and the current limitations of those neuromonitoring techniques. The subsequent section will provide the reader with the necessary background for understanding the theory behind NIRS analysis. Finally, the research objectives will be explained, and a brief overview of the subsequent chapters is included.

1.1 Clinical Motivation

1.1.1 Brain Injury during cardiac surgery

The brain is extremely vulnerable during the time surrounding cardiac surgery, and perioperative brain injury is a major complication of cardiac operations¹⁻³. Under standard conditions the brain is protected from fluctuations in oxygen delivery via a process called cerebral autoregulation, which maintains homeostasis in the brain by regulating the flow and pressure of the cerebral blood supply^{4,5}. When the cerebral perfusion pressure is between 60 mmHg and 150 mmHg, cerebral autoregulation ensures

the brain is protected from dramatic changes in oxygen delivery by regulating resistance in the cerebral arteries⁴. However, cerebral autoregulation can be heavily impaired outside of this pressure range, leaving the brain at a higher risk for ischemic injury^{6,7}. An article by Ono *et. al.* in 2012 reported that 20% of patients who undergo cardiopulmonary bypass suffer from impaired cerebral autoregulation during the operation⁷. There is a high risk of various types of brain injuries during cardiac operations due to the various disruptions to blood flow associated with heart surgery and the manipulation of major vessels commonly resulting in dislodging plaque from vessel walls⁸.

The American College of Cardiology and American Heart Association Task Force classify neuronal deficits resulting from cardiac surgery in two categories⁹. Type 1 brain injuries are those which are focal injuries, including a focal stroke, transient ischemic attack (TIA), and fatal cerebral injuries; these are insults that have a clear point source. In contrast, Type 2 deficits are typically global brain injuries, often associated with a decrease in intellectual function or memory, increases in confusion or agitation, or seizures without evidence of a focal point. Examples of Type 2 injuries include encephalopathy, neurocognitive dysfunction, and delirium. A study by Roach *et al.* found that the prevalence of postoperative brain injuries is evenly split between these two types (3.1% for Type 1 and 3.0% for Type 2) and are present in approximately 6.1% of cardiac surgery patients who undergo a coronary artery bypass graft (CABG)². Type 1 and 2 brain injuries are also associated with higher mortality rates (21% for type 1, 10% for type 2, and 2% for those without cerebral injury) and longer hospitalizations (25 days for Type 1 and 21 days for Type 2, versus 10 days for those without cerebral injury)². More recent studies using magnetic resonance imaging (MRI) with diffusion-weighted imaging (DWI) have found that between 18% and 26% of low-risk patients undergoing a CABG surgery suffer from acute perioperative brain ischemia^{10,11}. That range increases to as high as 45% to 62% for high-risk patients^{12,13}. As such, perioperative brain injury not only negatively impacts patient outcomes, but also greatly increases treatment costs.

It is estimated that over 1 million cardiac surgeries are performed each year worldwide, and this number is expected to significantly increase as the population ages¹⁴. Even with the current numbers, approximately 60,000 patients suffer from cardiac surgery related

cerebral complications each year. As such, there is a clear need for intraoperative brain monitoring during cardiac surgery to permit timely interventions that can prevent permanent brain injury.

1.1.2 Current Methods of Detecting Brain Injury

There are several methods for diagnosing brain injuries, including neurological examination, MRI, computed tomography (CT), transcranial doppler ultrasound (TCD), electroencephalography (EEG), and NIRS¹⁵. Each of these modalities have their own strengths and limitations that make them better suited for certain applications than others. Neurological examinations can be used to evaluate changes in memory, attention, and motor skills, and may reveal conditions that are not readily detectable by other modalities^{15,16}. However, neurological examination has the obvious setback of requiring the patient to be conscious, which is not feasible during cardiac surgery. MRI with DWI has been shown to be highly sensitive to postoperative cerebral injury¹⁷, but due to the large size of MRIs and the strong magnetic fields inherent to the technology, it is not practical to use in an operating room (OR) for continuous monitoring. While CTs are smaller than MRIs, the use of ionizing radiation similarly reduces the practicality of the modality for continuous intraoperative monitoring as doing so would significantly increase a patient's radiation dose¹⁸. Despite being unsuitable for intraoperative monitoring, the high sensitivity and specificity of these three modalities make them reliable pre- and post-operative neurodiagnostic tools.

Unlike the three aforementioned modalities, TCD, EEG, and NIRS are well suited for intraoperative neuromonitoring due to their small size, non-invasiveness, and lack of ionizing radiation. TCD can measure changes in blood flow velocity in arteries such as the middle cerebral artery; however, TCD cannot directly measure tissue perfusion, but instead provides an estimate of blood flow from the velocity and a predefined average artery size¹⁹⁻²¹. Additionally, it is easy to misdiagnose an embolic event as an artifact, requiring a skilled interpreter to maximize the effectiveness of this modality. EEGs work by monitoring for changes in the electrical potentials produced by neurons and is the most used modality for intraoperative monitoring^{19,20,22}. However, EEGs also require skilled interpreters and have the additional limitation of being influenced by general

anaesthesia, body temperature, and cerebral oxygen content, limiting its suitability for cardiac surgery²².

The third intraoperative monitor, NIRS, uses near-infrared light to measure light attenuation by tissue and interprets that optical signal to calculate changes in cerebral oxygen saturation (ScO₂) and total hemoglobin concentration^{23–26}. NIRS output provides objective metrics that are more easily interpreted by physicians than EEG or TCD, without the need for specialized training²⁷. Additionally, it has been shown that maintaining the ScO₂ as close to the preoperative baseline as possible results in a significant reduction in the incidence of post-operative stroke²⁸. The major limitation of NIRS when attempting to non-invasively probe the adult brain is that the extracerebral tissues (ECL) significantly contaminate the optical signal²⁹. As will be discussed in greater detail throughout this thesis, the methods described in Chapters 2 and 3 solve this limitation by assuming the head is composed of two layers: one layer is the ECL, and the other layer is the brain tissue.

1.2 Near-Infrared Spectroscopy

1.2.1 Background and Uses

NIRS is a non-destructive optical spectroscopy method that uses safe, nonionizing near-infrared light to probe media^{23,30–32}. While NIRS has many applications, including in astronomy^{33,34}, agriculture^{35,36}, and material sciences^{37–39}, this work will focus on its biomedical applications. The first report of the use of NIRS for monitoring biological tissue was by Jöbsis in 1977 at Duke University⁴⁰. Since that initial publication, NIRS has found many biomedical applications ranging from musculoskeletal^{41–44}, to diabetes^{45–50}, kinetic modeling of blood flow^{51–54}, and brain monitoring^{28,29,52,55,56}.

The wavelengths of light used for NIRS varies depending on the application but are typically within the first optical window (650 nm to 1000 nm)^{57,58}. This range of wavelengths is ideal for probing biological tissue because of the relatively low absorption and scattering of the tissue in the near infrared range. Notably, light is highly absorbed by blood below 650 nm, while above 1000 nm the absorption of water impedes the use of NIRS, greatly reducing the amount of signal available for analysis⁵⁹. It is important to

note that NIRS is primarily sensitive to the microvasculature, as light experiences nearly-complete attenuation in vessels larger than 1 mm^{60,61}.

1.2.2 Optical Properties

Unlike X-rays, near-infrared light does not travel in a straight line between the source and detector in tissue. By comparison, the light within the near-infrared range experiences significant scattering when passing through biological tissues, resulting in the stochastic path of the photons^{59,62}. There are four primary optical properties that describe the behavior of light in biological tissues. These properties are the absorption coefficient, scattering coefficient, anisotropic factor, and refractive index^{59,63-65}.

The absorption coefficient represents the amount of light expected to be absorbed by a medium after traveling a specific distance and is primarily affected by the chemical composition of tissue⁵⁹. The concentrations of light absorbing chemicals (chromophores) are directly related to the strength of the absorption in the tissue.

The scattering coefficient is the fraction of light that changes its direction of propagation when it passes through a medium, divided by the medium thickness⁶⁵⁻⁶⁷. The primary form of photon scattering in biological tissues is Mie scattering, which is a type of elastic scattering – the photon conserves its energy while its direction changes. Mie scattering is primarily due to the light interacting with cellular structures in the tissue such as the nuclei, organelles, and the cell membranes. Both the absorption and scattering coefficient of tissue are typically expressed in units of cm^{-1} or mm^{-1} ⁵⁹.

The anisotropy factor is a measure of how much of the forward direction (i.e., along its original trajectory) is retained after each scattering event^{59,68}. The values of the anisotropic factor range from -1 to 1 and are unitless. A photon in a medium with an anisotropic factor of 1 is perfectly scattered in the forward direction, giving the impression that no scattering event has occurred. Conversely, a photon which has been scattering in a medium with an anisotropic factor of -1 will be perfectly backscattered, resulting in the photon appearing as if it has reversed directions along its vector. Finally,

a medium with an anisotropic factor of 0 is considered isotropic, meaning the photon has an equal chance of being scattered in any direction.

The final optical property is the refractive index, which is the ratio of the speed of light in a vacuum to the speed of light in the tissue^{59,69}. The refractive index also defines how the direction of the light will change at tissue boundaries using Snell's Law⁷⁰.

All four optical properties are independent of each other and depend on the wavelength of light⁵⁹. As such, they must be independently estimated in order to accurately model light transport in a given tissue for a specified wavelength. However, in a highly scattering media such as most biological tissues, the net scattering of photons quickly becomes random, resulting in homogenous scattering after a few millimeters. As a result, the scattering coefficient (μ_s) and anisotropic factor (g) can be combined into the reduced scattering coefficient (μ'_s), which can be calculated using the following equation^{59,71}:

$$\mu'_s = \mu_s(1 - g) \quad (1.1)$$

1.2.3 Tissue Optical Properties

While the adult head contains many tissues, in this thesis it is assumed that the head consists of scalp, skull, cerebrospinal fluid (CSF), and brain tissue. While this is obviously a simplification, it is noteworthy that these four tissues compose the bulk of the adult head, and this decomposition is a fair approximation. In this thesis the terms scalp and skin are used interchangeably. Further, the optical properties of these four tissues have been well studied in the literature, and in 2013 Steven Jacques conducted an extensive review of tissue optical properties⁵⁹. Table 1.1 shows typical values for anisotropic factor and refractive index for the scalp, skull, CSF, and brain tissue⁵⁹.

Table 1.1: Anisotropic Factor and Refractive Index of Tissues

Tissue	Anisotropic factor (g)	Refractive index (n)
Scalp	0.85	1.4
Skull	0.85	1.4
Cerebrospinal fluid (CSF)	0.8	1.33
Brain	0.85	1.4

While the anisotropic factor and refractive index are dependent of wavelength, there is negligible change in the value of these variables over the wavelengths used throughout this work⁵⁹. As such, the values in Table 1.1 are assumed to be true for all wavelengths.

The absorption and scattering coefficients vary considerably between the various tissues and wavelengths⁵⁹. Figure 1.1 shows the scattering coefficients for the four tissue types between 650 nm and 950 nm. The scattering coefficients can be modeled using Eq 1.2:

$$\mu_s = \frac{a(\frac{\lambda}{500})^{-b}}{(1-g)} \quad (1.2)$$

where a is the scattering coefficient at 500 nm for that tissue, b characterizes the wavelength dependence and is called the scattering power, and λ is the wavelength (in nm). Table 1.2 lists the values of a and b for the skin, skull, and brain tissues. The scattering coefficient of the CSF is effectively that of water ($\sim 0.0001 \text{ mm}^{-1}$)^{72,73}, and is consequently assumed to be a negligible throughout this thesis.

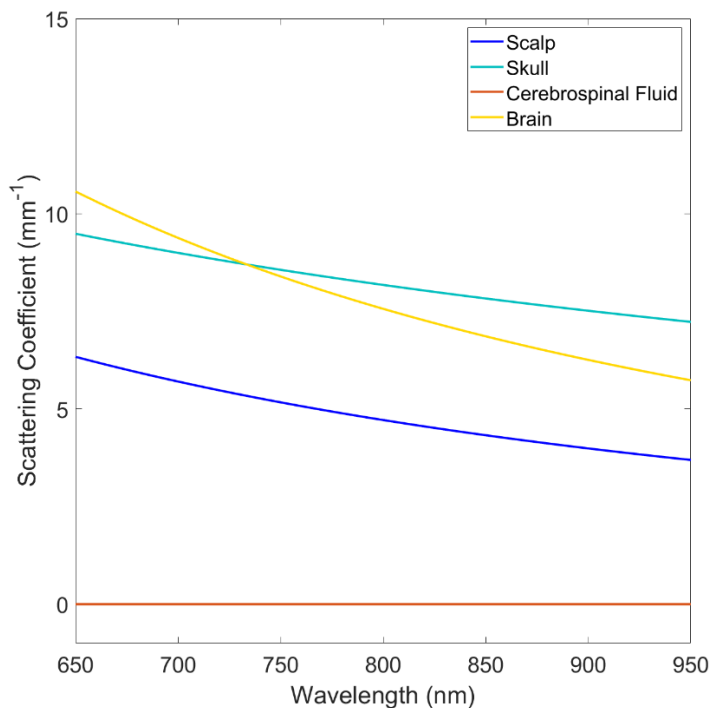


Figure 1.1: Wavelength Dependent Scattering Coefficients. For the scalp, skull, and brain, the values are found using Eq 1.2 and the values from Table 1.2 for every wavelength between 650 nm and 950 nm. For the cerebrospinal fluid, the values were assumed to be 0.0001 mm^{-1} for every wavelength.

Table 1.2: The values for the scattering coefficients at 500 nm (a) for Scalp, Skull, and Brain tissue, and their respective scattering powers (b).

Tissue	a (mm^{-1})	b
Scalp	4.60	1.42
Skull	2.29	0.72
Brain	2.42	1.61

The absorption spectra (i.e., the absorption coefficients of a tissue over a wide range of consecutive wavelengths) of tissues have been widely studied in the literature⁵⁹. Sample absorption spectra for skin, bone, CSF, and brain tissue are shown in Figure 1.2.

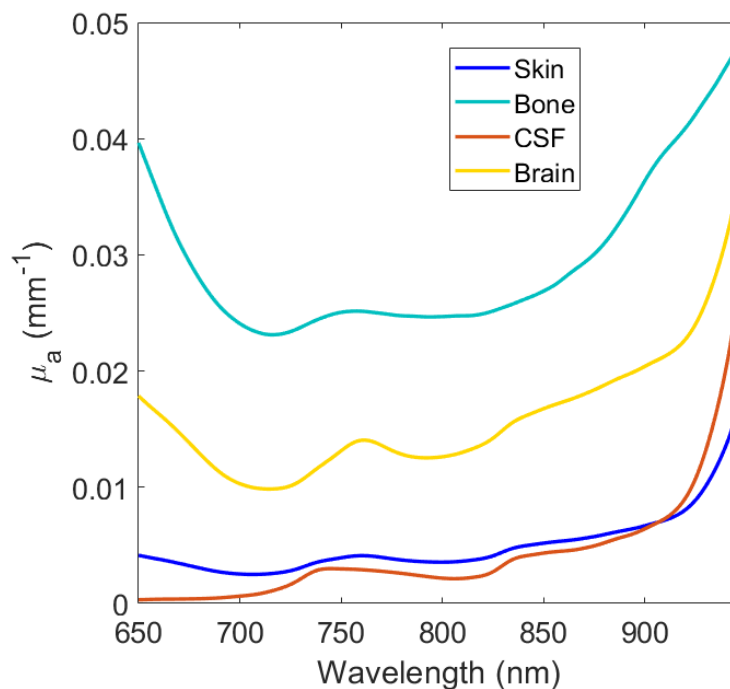


Figure 1.2: Sample absorption spectra of the four tissue types that compose the head. The brain spectrum (yellow) is for a brain containing 55 μM of hemoglobin with 70% ScO_2 , and 80% water.

As mentioned in Section 1.2.2, the absorption coefficient depends on the chemical composition of the tissue. Chromophores absorb different wavelengths of light in varying amounts, and the amount of absorption at a given wavelength, normalized against its concentration, is given by the extinction coefficient (units $\text{mm}^{-1}\mu\text{M}^{-1}$). The left axis of Figure 1.3 shows the extinction spectra for oxy- and deoxyhemoglobin between 650 nm and 950 nm⁷⁴⁻⁷⁶.

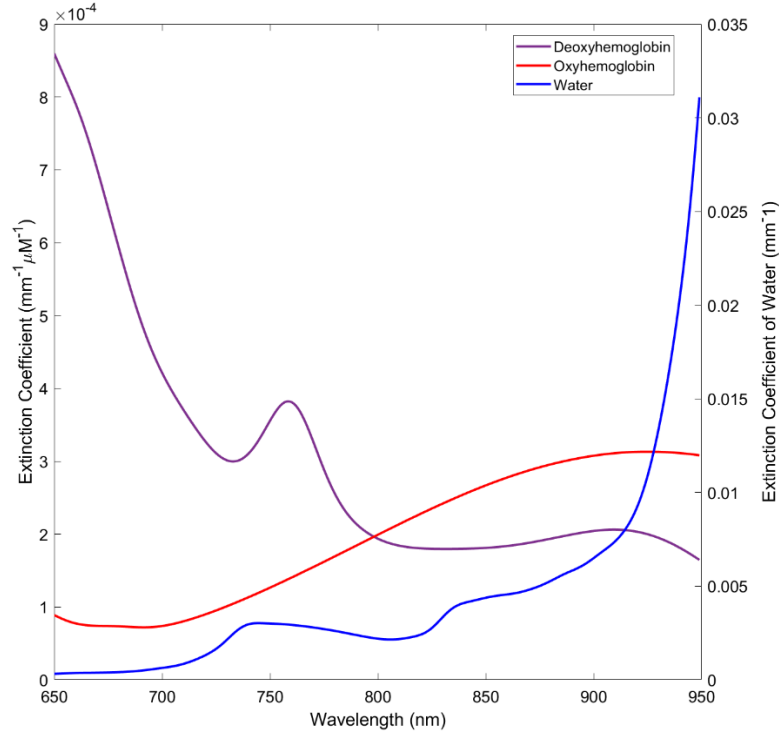


Figure 1.3: Extinction coefficient spectra of water on the right axis and oxy- and deoxyhemoglobin on the left axis.

Eq 1.3 can be used to estimate the absorption coefficient (μ_a) of a tissue by knowing the extinction coefficients of its chromophores (ϵ_i) and their concentrations⁵⁹:

$$\mu_a(\lambda) = \sum_i (C_i * \epsilon_i(\lambda)) \quad (1.3)$$

where C_i is the concentration of a given chromophore in the tissue. While the brain and skin have many chromophores, the major contributors to near-infrared light absorption are water, oxyhemoglobin, and deoxyhemoglobin^{59,77,78}. As such, the absorption coefficient of the brain and scalp can be estimated from the concentrations of these three chromophores using the following equation:

$$\mu_a(\lambda) = \epsilon_{Water}(\lambda) * WF + C_{HbO_2} * \epsilon_{HbO_2}(\lambda) + C_{Hb} * \epsilon_{Hb}(\lambda) \quad (1.4)$$

where ϵ_{Water} , ϵ_{Hb} , and ϵ_{HbO_2} are the extinction coefficients of water, deoxyhemoglobin, and oxyhemoglobin, respectively, and WF (water fraction), C_{Hb} , and C_{HbO_2} are their respective tissue concentrations. Notice that extinction coefficients of water have the

units mm^{-1} instead of $\text{mm}^{-1}\mu\text{M}^{-1}$. This is due to being based on a volume that is 100% water and is the reason why water absorption coefficient is expressed in terms of water fraction, which is the percent of tissue volume occupied by water. The right axis of Figure 1.3 shows the extinction coefficients of water between 650 nm and 950 nm^{74,75}.

The water fraction in the adult brain is well known and quite consistent across many species⁷⁹. The adult human brain is composed of approximately 80% water^{79,80} and is expected to be constant over short periods of time, such as during cardiac surgery. Additionally, it has been shown in the literature that inaccurate recovery of the brain's water fraction has a negligible impact on the recovery of the ScO_2 ^{78,81,82}. In the skin the water fraction is approximately 50%, and similarly is relatively constant over short periods of time⁸³. As both brain and scalp water fractions should be stable over short time-frames, major changes in the absorption coefficient of the brain and skin can be attributed to changes in the oxy- and deoxyhemoglobin concentrations. Figure 1.4 shows three sample brain absorption coefficient spectra that are possible over the course of a cardiac surgery depending on the concentrations of oxy- and deoxyhemoglobin.

It is important to note that the optical properties of the skin may vary during procedures due to many variables, including whether the patient is awake vs asleep and skin temperature variation at the measurement site⁸⁴. Because of this, in my simulations I investigate the effects of changing the skin physiological parameters on the recovered brain parameters.

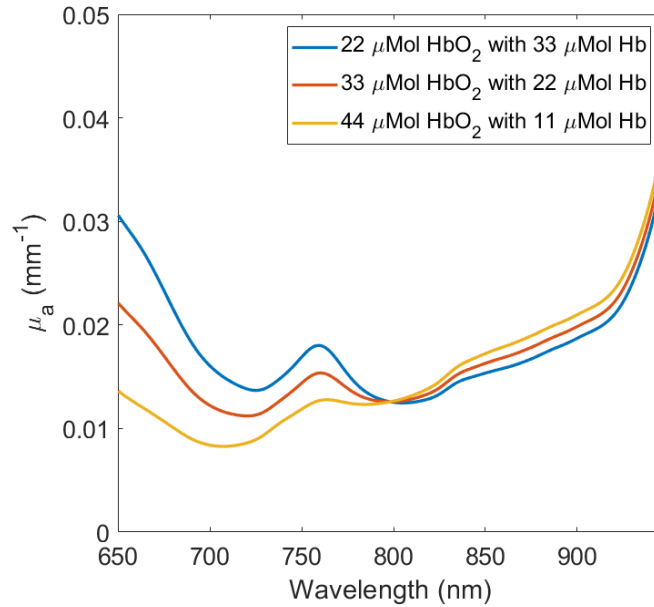


Figure 1.4: Sample absorption coefficient (μ_a) spectra for brain tissue depending on the concentrations of oxy- (HbO₂) and deoxyhemoglobin (Hb). The total hemoglobin is equal to 55 μ Mol in each spectrum, meaning the differences in the curves are due to the proportions of oxy- and deoxyhemoglobin.

1.2.4 Beer-Lambert Law

In 1729, Pierre Bouguer discovered that the amount of light absorbed by a tissue is directly related to the thickness of the medium the light travels through⁸⁵. This law would later be reported by Johann Heinrich Lambert in *Photometria*, his seminal book published in 1760 on the measurement of light^{86,87}. This property of light was further expanded by August Beer in 1852, when he discovered that the attenuation of light is also related to the concentration of light absorbers in the medium^{88,89}. The combined law is commonly referred to as the Beer-Lambert law (Eq. 1.5):

$$A(\lambda) = \log_{10}\left(\frac{I_0(\lambda)}{I(\lambda)}\right) = \sum_i \varepsilon_i(\lambda) C_i d_i \quad (1.5)$$

where A is the attenuation, $I_0(\lambda)$ is the reference light intensity and $I(\lambda)$ is the light intensity after it travels through the sample, for a given wavelength. The Beer-Lambert law relates the light attenuation to the sum of the product of the extinction coefficient (ε),

concentration (C), and physical thickness (d) for each light absorber present in the sample. The Beer-Lambert law can be combined with Eq. 1.3 to calculate attenuation in terms of absorption coefficient:

$$A(\lambda) = \sum_i \mu_{a_i} d_i \quad (1.6)$$

Eq. 1.6 shows a clear proportional relationship between the attenuation of a sample and the thickness of the medium. However, the Beer-Lambert law has a major limitation; it is only valid for non-scattering media. The Beer-Lambert law assumes that light travels along the line-of-sight between the source and the detector. As mentioned earlier, this is not the case in biological tissues. Near-infrared light in tissue experiences significant scattering, resulting in a substantial increase in photon pathlength in the medium and thus greater attenuation than would be expected. This results in the attenuation no longer being linearly related to the absorption coefficient. Furthermore, scattering produces attenuation even when there is no light absorption. As such, the Beer-Lambert law needs to be modified to accommodate this change in light behavior in tissue^{90,91}:

$$A(\lambda) = DP(\lambda) \sum_i \varepsilon_i(\lambda) C_i + G(\lambda) = DP(\lambda) \sum_i (\mu_{a_i}(\lambda)) + G(\lambda) \quad (1.7)$$

where DP is the differential pathlength and G is a term that accounts for light attenuation due to scattering. Differential pathlength represents the mean distance traveled by the light in the scattering medium and is typically three to six times the distance between the point of entry to and point of exit from the medium (i.e., the distance between the source and detector). The differential pathlength is equal to the physical distance between the source and detector times the differential pathlength factor (DPF). Furthermore, the differential pathlength is dependent on the absorption and reduced scattering coefficients of the medium^{92,93}:

$$DP(\lambda) = DPF(\lambda) \times d \approx \frac{1}{2} \sqrt{\frac{3\mu'_s(\lambda)}{\mu_a(\lambda)}} \times d \quad (1.8)$$

As shown in Equation 1.8, the differential pathlength factor depends on the optical properties of the tissue⁹⁴. In some techniques the differential pathlength is assumed to be constant. However, there are many procedures where the absorption coefficient of the

tissue may change rapidly^{84,95}. Thus, assuming a constant differential pathlength factor may confound the results and lead to uncertainty in the estimation.

1.2.5 Diffusion Approximation

A more advanced method for quantifying the optical properties of a medium is to use the radiative transfer equation (RTE). The RTE is a theory based on observations describing the transfer of energy through a scattering medium. Unfortunately, the RTE does not have a practical solution, making it difficult to solve^{59,96}. Approximations are often made to reduce the complexity of the problem, with the diffusion approximation (DA) being the most commonly used approach. The DA to the RTE assumes that the light is traveling through a highly scattering medium, meaning the light transport can be treated as diffuse throughout the medium. The DA provides a differential equation that expresses the photon fluence rate, $\Phi(r, t)$, in the tissue as a function of the optical properties⁹⁷:

$$\frac{1}{v} \frac{\partial}{\partial t} \Phi(r, t) - D \nabla^2 \Phi(r, t) + \mu_a \Phi(r, t) = S(r, t) \quad (1.9)$$

where v is the speed of light in the medium, r is the position in the tissue, t is time, D is the photon diffusion coefficient, and $S(r, t)$ describes the light source. The photon diffusion coefficient is given by^{96,97}:

$$D = \frac{1}{3(\mu'_s + \mu_a)} \quad (1.10)$$

The solution to the diffusion approximation depends on the boundary conditions, but before the boundary conditions can be discussed the two primary measurement orientations used in NIRS will be introduced. The first orientation is to have the detector positioned directly across the tissue. This is referred to as transmittance and can be seen in Figure 1.5A^{50,98}. This orientation is limited by the thickness of the tissue, as the light must travel through its entirety before reaching the detector. Common applications of such measurement geometry are finger and earlobes, for which short source-detector distances are possible. The other measurement orientation is reflectance wherein a NIRS system is set up such that both the source and detector are on the same surface, as shown in Figure 1.5B^{50,98}. This setup requires a highly scattering medium, such as biological

tissues, to redirect the photons back towards the surface. Reflectance mode is typically used for larger tissues such as the human head or leg muscles, for which measurements in transmittance mode would be challenging due to absorption. The analysis methods throughout this thesis use the reflectance geometry, as it is better suited for the adult head.

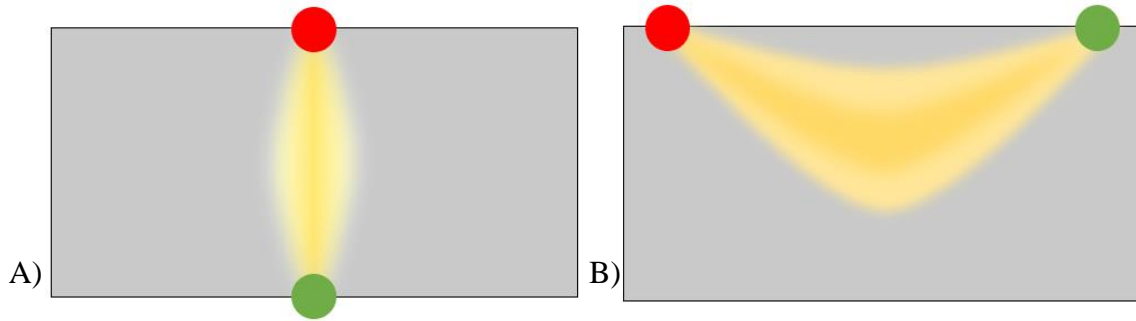


Figure 1.5: A) Transmittance: The source (red) and detector (green) are on opposite faces of the tissue. B) Reflectance: The source (red) and detector (green) are on the same face of the tissue.

The most common boundary conditions used for the adult head is to assume an optically semi-infinite medium, with the light source and detector located on the surface of the medium⁹⁶. This postulate is based on the fact that light does not effectively reach the opposite side of the adult head due to its size, strong light scattering, and absorption, which justify the semi-infinite medium assumption. Under these boundary conditions the reflectance (R) at the detector can be expressed as a function of the photon fluence rate⁹⁶:

$$R(\rho, t) = 0.118\Phi(\rho, z = 0, t) + 0.306R_f \quad (1.11)$$

where ρ is the source-detector distance, z is the distance to the tissue boundary and is set to 0 since the detectors are typically placed on the tissue surface, and R_f is the diffuse reflectance from the medium across the tissue boundary⁹⁶. For a pulsed light source behaving as a delta function (both spatially and temporally) under these boundary conditions, the fluence rate (Φ) can be expressed as⁹⁶:

$$\Phi(\rho, z, t) = \frac{v}{(4\pi Dvt)^{\frac{3}{2}}} \times e^{-\mu_a vt} \times \left(e^{-\frac{(z-z_0)^2 + \rho^2}{4Dvt}} - e^{-\frac{(z+z_0+2z_b)^2 + \rho^2}{4Dvt}} \right) \quad (1.12)$$

where z_0 and z_b are given by equations 1.13 and 1.14, respectively.

$$z_0 = \frac{1}{(\mu_a + \mu'_s)} \quad (1.13)$$

$$z_b = \frac{1+R_{eff}}{1-R_{eff}} 2D \quad (1.14)$$

In Eq 1.14, R_{eff} is the fraction of the light that is internally reflected at the tissue boundary and is approximately 0.493 for the refractive index is 1.4 such as in tissues. The diffuse reflectance due to the tissue boundary (R_f) in Eq 1.11 is given by Eq 1.15:

$$R_f(\rho, t) = \frac{1}{2} (4\pi Dv)^{-\frac{3}{2}} t^{-\frac{5}{2}} e^{-\mu_a vt} * \left(z_0 e^{-\frac{(z_0^2 + \rho^2)}{4Dvt}} + (z_0 + 2z_b) e^{-\frac{((z_0 + 2z_b)^2 + \rho^2)}{4Dvt}} \right), \quad (1.15)$$

A major limitation of using these boundary conditions when solving the DA is that it assumes the sample is a homogenous medium⁹⁶. This means there is no distinction between the ECL and the brain, resulting in contamination when these analytical solutions are used to analyze NIRS brain measurements. This issue is negligible in neonates due to their thin skulls; however, in adult measurements, 50-80% of the optical signal come from the ECL even when the source and detector distance is at 3 cm, resulting in significant contamination²⁹.

The two-layer solution to the DA addresses this issue by assigning different optical properties for the top (i.e., ECL) and bottom (i.e., brain) layers. The two-layer DA solution developed by Kienle et. al. in 1998 uses a fast Fourier transform to calculate the time-resolved solution from the frequency-domain solution at many frequencies⁹⁹. The two-layer DA solution in the frequency domain is given by Eq 1.16:

$$R^{(f)}(\rho, \omega) = 0.118\Phi_1^{(f)}(\rho, z = 0, \omega) + 0.306D \frac{\partial}{\partial z} \Phi_1^{(f)}(\rho, z, \omega) \Big|_{z=0} \quad (1.16)$$

where the $\Phi_1^{(f)}$ is the two-layer DA fluence solution, and ω is the angular frequency of the light source. The superscript (f) is used to represent variables that are in the frequency domain. The two-layer DA fluence solution in the frequency domain is given by Eq 1.17⁹⁹:

$$\Phi_1^{(f)}(\rho, z) = \frac{1}{2\pi} \int_0^\infty \phi_1^{(f)}(z, s) s J_0(s\rho) ds \quad (1.17)$$

In Eq 1.17 s is an integration variable, J_0 is the zeroth order Bessel function of the First kind (Eq. 1.18), and $\phi_1^{(f)}$ is given by eq. 1.19 when the source is located on the tissue surface⁹⁹:

$$J_0(s\rho) = \sum_{k=0}^{\infty} \frac{(-1)^k \left(\frac{s\rho}{2}\right)^{2k}}{k! \Gamma(k+1)} \quad (1.18)$$

$$\phi_1^{(f)}(z, s) = \frac{\sinh(\alpha_1(z_b+z_0))}{D_1\alpha_1} * \frac{D_1\alpha_1 \cosh[\alpha_1(l-z)] + D_2\alpha_2 \sinh[\alpha_1(l-z)]}{D_1\alpha_1 \cosh[\alpha_1(l+z)] + D_2\alpha_2 \sinh[\alpha_1(l+z)]} - \frac{\sinh[\alpha_1(z_0-z)]}{D_1\alpha_1}, \quad (1.19)$$

where l is the top layer thickness and D_1 and D_2 are calculated using Eq. 1.10 for with the optical properties of the top (1) and bottom (2) layers. α_1 and α_2 are provided in Eq. 1.20 for their respective tissue:

$$\alpha_i = \sqrt{\frac{D_i s^2 + \mu_{ai} + \frac{\sqrt{-1}\omega}{v}}{D_i}} \quad (1.20)$$

After solving the equation at many frequencies, the Fast Fourier Transform converts the solutions from the frequency domain into the time domain⁹⁹. Figure 1.6 shows a comparison of the homogeneous DA and the two-layer DA, both as a function of time. As shown, the two solutions are highly comparable when the optical properties of the top and bottom layers are identical, and the same as those of the homogenous semi-infinite medium.

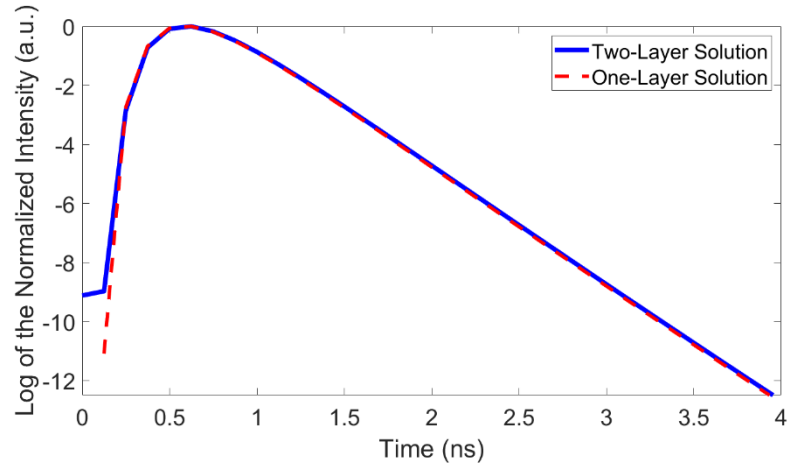


Figure 1.6: The one- and two-layer solutions to the diffusion approximation (DA). Optical properties in both layers of the two-layer solution are the same for a direct comparison to the homogeneous semi-infinite solution. Absorption is 0.0161 mm^{-1} , reduced scattering coefficient is 0.840 mm^{-1} , and the refractive index is assumed to be 1.4.

1.2.6 Blood, Oxygen, and the Brain

Oxygen is the terminal electron acceptor from the electron transport chain and thus a key component in the cellular respiration process¹⁰⁰. Without a constant supply of oxygen brain tissues quickly become hypoxic, eventually leading to necrosis and brain damage^{101,102}. The heart constantly pumps blood throughout the body to ensure there is sufficient oxygen reaching all organs, particularly the brain. While there is a small amount of oxygen freely diffusing in the blood, much of the circulatory oxygen is bound to hemoglobin molecules inside erythrocytes (red blood cells)¹⁰³. While a description of the exact biochemical structure of hemoglobin is beyond the scope of this thesis, it can be simply described as a protein comprised of four globular protein subunits, each containing a heme group bound to an iron atom¹⁰³. The hemoglobin protein can bind up to 4 oxygen molecules, facilitating circulatory oxygen transport. There are two primary forms of hemoglobin that are of interests for this project: oxyhemoglobin and deoxyhemoglobin. Oxyhemoglobin refers to the hemoglobin molecules that have bound four oxygen atoms, while deoxyhemoglobin refers to the fully unbound hemoglobin

protein. Throughout this thesis, the terms hemoglobin and total hemoglobin are used interchangeably to refer to the sum of oxy- and deoxyhemoglobin in the tissue.

The distinct absorption of oxy- and deoxyhemoglobin in the first optical window and their critical importance to cell viability make them ideal chromophores for NIRS. As mentioned in Section 1.2.4, the extinction spectra for the two states of hemoglobin are major contributors to light absorption in the brain^{82,104,105}. Thus, NIRS measurements at several wavelengths can be used to compute the concentrations of oxy- and deoxyhemoglobin in the probed tissue^{31,77,106}. From the concentrations of oxy- and deoxyhemoglobin, the blood oxygen saturation (SO_2) in the tissue can be calculated using Eq 1.21³¹:

$$SO_2 = \frac{HbO_2}{HbO_2 + Hb} \quad (1.21)$$

Tissue oxygen saturation (i.e., tissue blood oxygen saturation) is a useful biomarker of tissue viability because it provides direct information about the oxygen availability to the tissues of interest, informing physicians about the balance between oxygen delivery and tissue oxygen consumption^{53,107}. Thus, low tissue oxygen saturation can lead to hypoxia, which can produce a cascade of failures potentially leading to tissue death^{101–103}. The side effects are especially devastating in cerebral hypoxia, which can lead to temporary or permanent memory loss, loss of mobility, shortened attention span, and impaired decision making, or more serious side effects such as seizures or brain death^{15,108}. Further, knowing the absolute concentrations of oxy- and deoxyhemoglobin instead of only the ratio between the two is important because it provides additional information about the cerebral blood flow and blood content. Sudden changes in these measures can indicate changes in tissue perfusion or metabolism¹⁰⁹.

Furthermore, in contrast to a pulse oximeter that only monitors for systemic blood oxygen saturation (i.e., arterial blood oxygen saturation), NIRS is capable of directly monitoring the oxygen saturation in specific regions of interest¹⁰⁷. This is particularly important during cardiac surgery, since there can be vascular injuries that only impact specific brain regions, causing no change in the pulse oximeter reading and thus would

not be detected. An ideal NIRS system for neuromonitoring during cardiac surgery would have multiple source-detector pairs sampling the 8 cerebral vascular territories¹¹⁰.

1.3 Continuous-wave NIRS

The vast majority of commercial NIRS systems are based on continuous-wave (CW) NIRS, which is the simplest NIRS method¹⁰⁷. In CW-NIRS, a beam of near-infrared light of fixed intensity is directed into the tissue and the attenuation of the beam is measured over an extended period of time. The changes in the light intensity are then analyzed to estimate changes in tissue composition, such as the ratio of oxy- and deoxyhemoglobin^{81,105,111}. Like many optical spectroscopy techniques, CW-NIRS typically uses measurements acquired at several wavelengths, ranging from two wavelengths to a full spectrum, to estimate tissue chromophore content.

CW-NIRS is especially well suited for neonates due to their thin skulls¹¹²⁻¹¹⁴. The ECL in a neonate is typically less than 2 mm, growing to approximately 4 mm by the time they are 3 years old¹¹⁵. The thinner ECL leads to less contamination of the optical signal compared to adult brain measurements, where the thickness of the ECL is 10-15 mm¹¹⁶. Additionally, the thicker adult ECL makes CW-NIRS more sensitive to changes in the scalp, which may be mistaken for changes in the brain. Selb *et. al.* showed that the sensitivity to the brain for CW-NIRS is only 8% in adults at a 3 cm source-detector distance, while the sensitivity to the scalp is approximately 88% at that same distance¹¹⁷.

Despite this low brain sensitivity, CW-NIRS analysis methods continue to be widely used because they are computationally efficient, allowing for the rapid recovery of changes in tissue absorption coefficients. However, because commercial CW-NIRS analysis methods primarily rely on the modified Beer-Lambert law, they are unable to calculate absolute values for the chromophore concentrations. This is due to the uncertainty in their photon pathlength resulting from the scattering nature of tissue¹⁰⁷. This reduces the suitability of CW-NIRS for longitudinal studies as a new baseline must be established for each session, as well as limits inter-subject comparability.

Several more advanced methods have been developed to address these issues, and the most common methods for correcting for the ECL involves increasing the source-detector distance and the number of detectors¹¹⁸. Increasing the distance between the source and detector can increase brain sensitivity, since depth penetration is related to the source-detector distance¹¹⁷. In contrast, increasing the number of detectors does not improve depth sensitivity but allows users to better differentiate which tissue layer is responsible for changes in the optical signal¹¹⁹. A third method for increasing sensitivity is to utilize additional wavelengths, leveraging the spectral features of oxy- and deoxyhemoglobin to aid in their recovery^{23,81,82,105}. Hyperspectral CW-NIRS systems, also referred to as broadband NIRS, have proven to have greater accuracy than those that use few wavelengths. Hyperspectral CW-NIRS systems also have the additional ability to calculate absolute cerebral concentrations of oxy- and deoxyhemoglobin, though the accuracy of this recovery decreases as ECL thickness increases¹⁰⁵.

1.4 Time-Resolved NIRS

1.4.1 General Theory and Uses

Despite the recent advancements in CW-NIRS, it is well known that time-resolved (TR) NIRS is the superior NIRS method as it provides a greater amount of information⁵⁴. TR-NIRS systems use pulses of near-infrared light (typically only a few picoseconds in duration) instead of a continuous beam^{107,111,120}. TR-NIRS detectors produce time-of-flight curves such as those seen earlier in Figure 1.6 by recording the time it takes for photons to travel from the light source to the detector¹⁰⁷. These time-of-flight curves are also called temporal point spread functions (TPSFs), which is the nomenclature used throughout this work. The amount of time the photons take to reach the detector is directly related to their travel distance because the speed of light in the tissues are relatively constant⁵⁹. Consequently, later arriving photons travel longer distances in the tissue and are more likely to have probed deeper tissue layers. Thus, to increase sensitivity to the brain, it is important to analyze later arriving photons.

TR-NIRS has a few disadvantages compared to CW-NIRS. For one, TR-NIRS requires more expensive and more complex equipment than CW-NIRS, including pulsed lasers

that operate at high frequencies, sensitive detectors such as photomultiplier tubes to detect individual photons, and high-precision electronics to precisely measure the arrival time of each photon with respect to the laser pulse¹²¹. As well, TR-NIRS analysis methods are typically more computationally intensive than those associated with CW-NIRS. This is because they typically involve a larger number of datapoints, compared to CW-NIRS, and often require the use of more computationally intensive mathematical operations, such as the Fourier Transform^{96,99,106,122}. Nevertheless, the increased information gained with the use of TR-NIRS makes the technique extremely valuable in many applications including adult neuromonitoring.

An important benefit of TR-NIRS is that the scattering and absorption coefficients become uncoupled in the time-of-flight curves, allowing for the recovery of their absolute values^{123,124}. As shown in Figure 1.7, the natural log of the reflectance approaches linearity as time progresses. The slope of the late-arriving photons in this region has a quasi-linear dependence on the absorption coefficient of the medium¹²³:

$$\mu_a(\lambda) = -\frac{\frac{\partial}{\partial t} \log(R(t \rightarrow \infty, \lambda))}{v} \quad (1.22)$$

The later the time, the greater the decoupling and the more accurate the estimate of absorption coefficient from the tail of the TPSF. However, the trade-off with using later time points is that the noise in the data increases as there are fewer photons in the tail of the TPSF. It is important when using TR-NIRS that there is a high signal-to-noise ratio to ensure the data being analyzed is representative of the tissue optical properties.

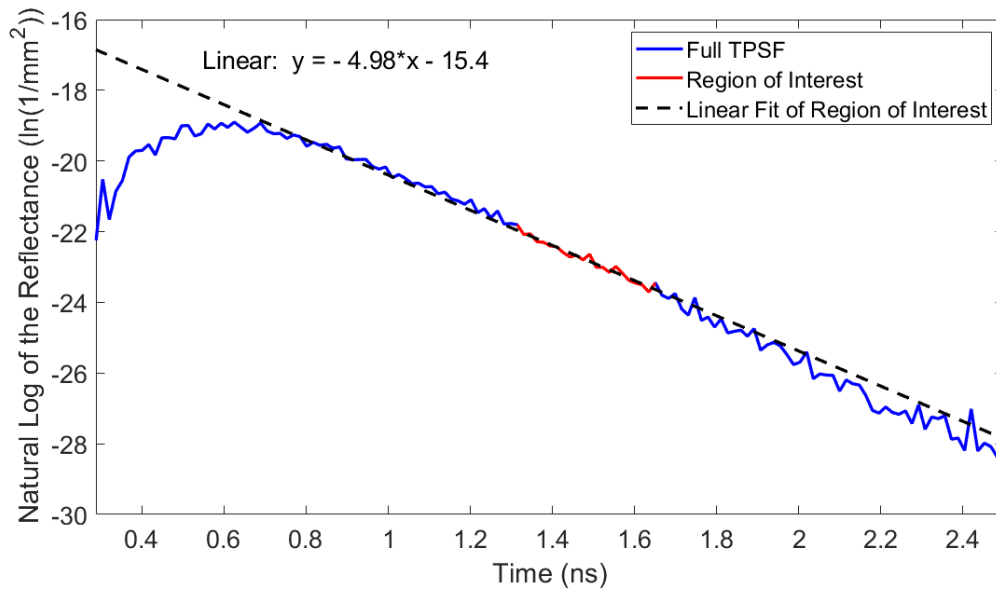


Figure 1.7: Late-photon analysis. The log of the time-of-flight curve approaches a linear slope as time increases. The region in red corresponds with the late-arriving photons and provides sufficient signal-to-noise ratio for analysis in an *in vivo* setting. The dotted black line is a linear fitting of the region of interest, and its slope is equal to the denominator of the right part of Eq. 1.22 and is related to the absorption coefficient of the medium.

1.4.2 Multi-spectral and Hyperspectral TR-NIRS

As mentioned in Section 1.2, the optical properties of the tissue are dependent on the wavelengths chosen. The concentrations of oxy- and deoxyhemoglobin can be more accurately recovered by using additional wavelengths to leverage their spectral features⁸². Most TR-NIRS systems use two to four wavelengths, though some have used up to sixteen in the past¹⁰⁶. These systems are typically referred to as multi-spectral TR-NIRS or few-wavelength TR-NIRS. The wavelengths chosen in these systems typically correspond with the absorption peaks of oxy- and deoxyhemoglobin to minimize crosstalk between chromophores¹⁰⁶.

An alternative approach is to use a hyperspectral system¹²⁴. A hyperspectral TR-NIRS system uses a much larger number of wavelengths spanning a wide range. Hyperspectral TR-NIRS is a novel approach and there is currently a limited body of work in this field. I

previously demonstrated during my undergraduate studies that hyperspectral TR-NIRS can increase sensitivity to adult brain oxygen saturation¹²⁴. These results confirmed the benefit of using hyperspectral approaches in TR-NIRS and laid the foundation for the current work.

1.5 Research Objectives

The goal of the research project reported in this master's thesis was to develop a TR-NIRS data analysis method that achieves a fast computation time without sacrificing accuracy to allow for quasi-real-time monitoring of adult ScO₂ and total cerebral hemoglobin concentration. There were two primary objectives:

1. Develop a two-layer fitting approach for few-wavelength TR-NIRS to recover ScO₂ and total hemoglobin in adults using a single detector with high accuracy.
2. Develop a hyperspectral TR-NIRS fitting algorithm based on the two-layer approach developed in objective 1 and the hyperspectral late-photon analysis method I previously developed in order to achieve near-real-time adult neuromonitoring with high accuracy.

The analysis methods developed in pursuit of these objectives are validated using Monte-Carlo simulations of photon transport in biological tissues.

1.6 Monte-Carlo Simulations

The Monte-Carlo method is a statistics-based computational algorithm that generates accurate solutions by estimating the probability of random events occurring¹²⁵. As mentioned earlier, modeling light transport in biological tissues is difficult to accurately achieve due to the many random events that can occur, drastically changing a given photon's travel path. Instead of attempting to precisely model the outcome with a single analytical solution, a Monte-Carlo simulation will conduct millions of independent random trials to calculate independent photon-paths¹²⁶⁻¹²⁸. With sufficient photon-paths calculated, the results begin to approach a realistic solution based on the probability of a given event occurring. This is analogous to flipping a coin; you may get a few heads in a row, but eventually you will approach the expected 50-50 distribution.

Monte Carlo Extreme (MCX) is a photon simulation platform that uses GPUs (Graphics Processing Units) to calculate many photon-paths in parallel, thereby increasing the speed of a given simulation by 300-fold^{127,128}. The accuracy of MCX simulations has been previously validated¹²⁸. The methods developed in pursuit of objectives one and two are validated using MCX simulations conducted in a four-layer adult head model with appropriate optical properties. More information about the simulations can be found in Chapters 2 and 3.

MCX simulations are used instead of *in vivo* experiments for the validation of these methods because they provide exact values to which the analysis methods can be compared. Additionally, conducting these experiments *in silico* rather than *in vivo* provides greater control of the experimental environment than would be otherwise possible. In an *in vivo* experiment there would be some degree of uncertainty in terms of the baseline optical properties. Conducting the validation *in silico* also allows for these methods to be validated over a wide variety of conditions without the need to conduct extensive *in vivo* studies. Unlike *in vivo* studies, an *in silico* study has no risk to patients or animals, is less burdensome, and can be easily scaled to include as many samples as required¹²⁹.

1.7 Thesis Outline

This thesis will present the development of two fast and reliable TR-NIRS analysis methods. The following two chapters will focus on addressing the above stated research objectives, with the method described in Chapter 3 addressing many of the limitations in Chapter 2. Chapter 4 will provide a summary and discussion of the major findings of this work and provide a conclusion.

1.7.1 Chapter 2: Estimating adult cerebral oxygen saturation from time-resolved near-infrared spectroscopy measurements with few discrete wavelengths at a single source-detector distance

Chapter 2 focuses on addressing objective 1, which is to develop an accurate TR-NIRS method that uses a single detector and few-wavelengths to recover adult ScO₂ and total cerebral hemoglobin content. This was accomplished using a two-layer analytical fitting

approach. The work presented in this chapter is adapted from my proceeding paper published by SPIE (Photonic West 2021), titled “Estimating adult cerebral oxygen saturation from time-resolved near-infrared spectroscopy measurements with few discrete wavelengths at a single source-detector distance,” by David Jonathan Fulop Cohen, Natalie Li, and Mamadou Diop.

1.7.2 Chapter 3: Fast Estimation of Adult Cerebral Oxygen Saturation and Total Hemoglobin using Hyperspectral Time-Resolved Near-Infrared Spectroscopy

Chapter 3 focuses on addressing objective 2, which is to develop an analysis method that can quickly and accurately recover adult ScO₂ and total cerebral hemoglobin from Hyperspectral TR-NIRS measurements. The approach taken in this chapter is a two-stage approach which allows for the accurate estimation of the initial baseline tissue hemoglobin and blood oxygenation, followed by the rapid recovery of these parameters during subsequent measurements. This chapter is adapted from an upcoming publication titled “Fast Estimation of Adult Cerebral Oxygen Saturation and Total Hemoglobin using Hyperspectral Time-Resolved Near-Infrared Spectroscopy” by David Jonathan Fulop Cohen, Natalie C. Li, Seva Ioussoufovitch, Vladislav Toronov, and Mamadou Diop.

1.7.3 Chapter 4: Conclusion and Future Work

Chapter 4 summarizes the major findings of the research provided as well as discusses its implications and limitations. The objectives and goal of this thesis will be revisited, and future work will be discussed. Finally, an overall conclusion will be provided.

References

1. Grogan K, Stearns J, Hogue CW. Brain Protection in Cardiac Surgery. *Anesthesiology Clinics*. 2008;26(3):521-538. doi:10.1016/j.anclin.2008.03.003
2. Roach GW, Kanchuger M, Mangano CM, et al. Adverse Cerebral Outcomes after Coronary Bypass Surgery. *New England Journal of Medicine*. 1996;335(25):1857-1864. doi:10.1056/NEJM199612193352501
3. Mangano DT, Mangano CM. Perioperative Stroke, Encephalopathy, and Central Nervous System Dysfunction. *Journal of Intensive Care Medicine*. 1997;12(3):148-160. doi:10.1177/088506669701200305
4. Paulson OB, Strandgaard S, Edvinsson L. Cerebral autoregulation. *Cerebrovascular and brain metabolism reviews*. 1990;2(2):161-192. doi:10.1161/01.str.15.3.413
5. Armstead WM. Cerebral Blood Flow Autoregulation and Dysautoregulation. *Anesthesiology Clinics*. 2016;34(3):465-477. doi:10.1016/j.anclin.2016.04.002
6. Kainerstorfer JM, Sassaroli A, Tgavalekos KT, Fantini S. Cerebral autoregulation in the microvasculature measured with near-infrared spectroscopy. *Journal of Cerebral Blood Flow and Metabolism*. 2015;35(6):959-966. doi:10.1038/jcbfm.2015.5
7. Ono M, Joshi B, Brady K, et al. Risks for impaired cerebral autoregulation during cardiopulmonary bypass and postoperative stroke. *British Journal of Anaesthesia*. 2012;109(3):391-398. doi:10.1093/bja/aes148
8. Hogue CW, Gottesman RF, Stearns J. *Mechanisms of Cerebral Injury from Cardiac Surgery*. Vol 24.; 2008.
9. Eagle KA, Guyton RA, Davidoff R, et al. ACC/AHA Guidelines for Coronary Artery Bypass Graft Surgery: A report of the American College of Cardiology/American Heart Association Task Force on Practice Guidelines

- (Committee to Revise the 1991 Guidelines for Coronary Artery Bypass Graft Surgery). *Journal of the American College of Cardiology*. 1999;34(4):1262-1347. doi:10.1016/S0735-1097(99)00389-7
10. Bendszus M, Reents W, Franke D, et al. Brain damage after coronary artery bypass grafting. *Archives of Neurology*. 2002;59(7):1090-1095. doi:10.1001/archneur.59.7.1090
 11. Floyd TF, Shah PN, Price CC, et al. Clinically Silent Cerebral Ischemic Events After Cardiac Surgery: Their Incidence, Regional Vascular Occurrence, and Procedural Dependence. *Annals of Thoracic Surgery*. 2006;81(6):2160-2166. doi:10.1016/j.athoracsur.2006.01.080
 12. Djaiani G, Fedorko L, Borger M, et al. Mild to moderate atheromatous disease of the thoracic aorta and new ischemic brain lesions after conventional coronary artery bypass graft surgery. *Stroke; a journal of cerebral circulation*. 2004;35(9). doi:10.1161/01.str.0000138783.63858.62
 13. Knipp SC, Matatko N, Wilhelm H, et al. Evaluation of brain injury after coronary artery bypass grafting. A prospective study using neuropsychological assessment and diffusion-weighted magnetic resonance imaging☆. *European Journal of Cardio-Thoracic Surgery*. 2004;25(5):791-800. doi:10.1016/j.ejcts.2004.02.012
 14. Veluz JS, Leary MC. Cerebrovascular Complications of Cardiac Surgery. In: *Primer on Cerebrovascular Diseases: Second Edition*. Elsevier Inc.; 2017:650-655. doi:10.1016/B978-0-12-803058-5.00126-0
 15. Ahonen J, Salmenperä M. Brain injury after adult cardiac surgery. *Acta Anaesthesiologica Scandinavica*. 2004;48(1):4-19. doi:10.1111/j.1399-6576.2004.00275.x
 16. Harvey PD. Clinical applications of neuropsychological assessment. *Dialogues in Clinical Neuroscience*. 2012;14(1):91-99. doi:10.31887/dcns.2012.14.1/pharvey

17. Wityk RJ, Goldsborough MA, Hillis A, et al. Diffusion- and perfusion-weighted brain magnetic resonance imaging in patients with neurologic complications after cardiac surgery. *Archives of Neurology*. 2001;58(4):571-576. doi:10.1001/archneur.58.4.571
18. Smith-Bindman R, Lipson J, Marcus R, et al. Radiation dose associated with common computed tomography examinations and the associated lifetime attributable risk of cancer. *Archives of Internal Medicine*. 2009;169(22):2078-2086. doi:10.1001/archinternmed.2009.427
19. Kowalczyk AK, Bachar BJ, Liu H. Neuromonitoring during adult cardiac surgery. *Journal of Biomedical Research*. 2016;30(3):171-173. doi:10.7555/JBR.30.20150159
20. Grocott HP. Monitoring the brain in cardiac surgery - an evolving area for research. *Anaesthesia*. 2012;67(3):216-219. doi:10.1111/j.1365-2044.2012.07076.x
21. Grocott HP, Amory DW, Croughwell ND, Newman MF. Transcranial Doppler blood flow velocity versus ¹³³Xe clearance cerebral blood flow during mild hypothermic cardiopulmonary bypass. *Journal of Clinical Monitoring and Computing*. 1998;14(1):35-39. doi:10.1023/A:1007493422230
22. Lewis C, Parulkar SD, Bebawy J, Sherwani S, Hogue CW. Cerebral Neuromonitoring During Cardiac Surgery: A Critical Appraisal With an Emphasis on Near-Infrared Spectroscopy. *Journal of Cardiothoracic and Vascular Anesthesia*. 2018;32(5):2313-2322. doi:10.1053/j.jvca.2018.03.032
23. Diop M, Elliott JT, Tichauer KM, Lee TY, Lawrence K. A broadband continuous-wave multichannel near-infrared system for measuring regional cerebral blood flow and oxygen consumption in newborn piglets. *Review of Scientific Instruments*. 2009;80(5):054302. doi:10.1063/1.3123347

24. Brown DW, Picot PA, Naeini JG, Springett R, Delpy DT, Lee TY. Quantitative near infrared spectroscopy measurement of cerebral hemodynamics in newborn piglets. *Pediatric Research*. 2002;51(5):564-570. doi:10.1203/00006450-200205000-00004
25. Tichauer KM, Hadway JA, Lee TY, Lawrence KS. Measurement of cerebral oxidative metabolism with near-infrared spectroscopy: A validation study. *Journal of Cerebral Blood Flow and Metabolism*. 2006;26(5):722-730. doi:10.1038/sj.jcbfm.9600230
26. Brown DW, Hadway J, Lee TY. Near-Infrared Spectroscopy Measurement of Oxygen Extraction Fraction and Cerebral Metabolic Rate of Oxygen in Newborn Piglets. *Pediatric Research*. 2003;54(6):861-867. doi:10.1203/01.PDR.0000090928.93045.BE
27. Stepan J, Hogue CW. Cerebral and tissue oximetry. *Best Practice and Research: Clinical Anaesthesiology*. 2014;28(4):429-439. doi:10.1016/j.bpa.2014.09.002
28. Goldman S, Sutter F, Ferdinand F, Trace C. Optimizing intraoperative cerebral oxygen delivery using noninvasive cerebral oximetry decreases the incidence of stroke for cardiac surgical patients. *Heart Surgery Forum*. 2004;7(5):392-397. doi:10.1532/HSF98.20041062
29. Milej D, Abdalmalak A, Rajaram A, Lawrence K. Direct assessment of extracerebral signal contamination on optical measurements of cerebral blood flow, oxygenation, and metabolism. *Neurophotonics*. 2020;7(04). doi:10.1117/1.nph.7.4.045002
30. Cohen DJF, Diop M. In silico investigation of near-infrared light propagation in the joints of the human hand. In: Fantini S, Taroni P, Tromberg BJ, Sevick-Muraca EM, eds. *Optical Tomography and Spectroscopy of Tissue XIII*. Vol 10874. SPIE; 2019:78. doi:10.1117/12.2508933

31. Mawdsley L, Abayomi N, Rajaram A, et al. Using near infrared spectroscopy and diffuse correlation spectroscopy to determine the microvascular effects of phenylephrine in vivo. In: Fantini S, Taroni P, eds. *Optical Tomography and Spectroscopy of Tissue XIV*. Vol 11639. SPIE; 2021:31. doi:10.1117/12.2577237
32. Boas DA, Franceschini MA. Haemoglobin oxygen saturation as a biomarker: The problem and a solution. *Philosophical Transactions of the Royal Society A: Mathematical, Physical and Engineering Sciences*. 2011;369(1955):4407-4424. doi:10.1098/rsta.2011.0250
33. Quinlan F, Ycas G, Osterman S, Diddams SA. A 12.5 GHz-spaced optical frequency comb spanning >400 nm for near-infrared astronomical spectrograph calibration. *Review of Scientific Instruments*. 2010;81(6):063105. doi:10.1063/1.3436638
34. Wilken T, Curto G lo, Probst RA, et al. A spectrograph for exoplanet observations calibrated at the centimetre-per-second level. *Nature*. 2012;485(7400):611-614. doi:10.1038/nature11092
35. Batten GD. An Appreciation of the Contribution of NIR to Agriculture. *Journal of Near Infrared Spectroscopy, Vol 6, Issue 1, pp 105-114*. 1998;6(1):105-114. Accessed April 22, 2021. <https://www.osapublishing.org/abstract.cfm?uri=jnirs-6-1-105>
36. García-Sánchez F, Galvez-Sola L, Martínez-Nicolás JJ, Muelas-Domingo R, Nieves M. Using Near-Infrared Spectroscopy in Agricultural Systems. In: *Developments in Near-Infrared Spectroscopy*. InTech; 2017. doi:10.5772/67236
37. Takeuchi M, Martra G, Coluccia S, Anpo M. Investigation of the Photoinduced Hydrophilic Properties of TiO₂ Surface by Near Infrared Spectroscopy. In: *Studies in Surface Science and Catalysis*. Vol 172. Elsevier; 2007:441-444. doi:10.1016/b978-0-444-53202-2.50099-3

38. Schwalm R. The UV Curing Process. In: *UV Coatings*. Elsevier; 2007:19-61. doi:10.1016/b978-044452979-4/50002-0
39. Fink JK. Cyanate Ester Resins. In: *Reactive Polymers: Fundamentals and Applications*. Elsevier; 2018:345-366. doi:10.1016/b978-0-12-814509-8.00010-5
40. Jöbsis FF. *Noninvasive, Infrared Monitoring of Cerebral and Myocardial Oxygen Sufficiency and Circulatory Parameters*. Vol 23.; 1977.
41. Hamaoka T, McCully KK, Quaresima V, Yamamoto K, Chance B. Near-infrared spectroscopy/imaging for monitoring muscle oxygenation and oxidative metabolism in healthy and diseased humans. *Journal of Biomedical Optics*. 2007;12(6):062105. doi:10.1117/1.2805437
42. Ioussoufovitch S, Morrison LB, Desjardins L, et al. Quantification of joint blood flow by dynamic contrast-enhanced near-infrared spectroscopy: application to monitoring disease activity in a rat model of rheumatoid arthritis. *Journal of Biomedical Optics*. 2020;25(01):1. doi:10.1117/1.jbo.25.1.015003
43. Maikala R v. Medical Utility of near Infrared Spectroscopy in Low Back Musculoskeletal Health and Disorders. *Journal of Near Infrared Spectroscopy*. 2012;20(1):151-184. doi:10.1255/jnirs.979
44. Perrey S, Thedon T, Bringard A. Application of near-infrared spectroscopy in preventing work-related musculoskeletal disorders: Brief review. *International Journal of Industrial Ergonomics*. 2010;40(2):180-184. doi:10.1016/j.ergon.2009.01.009
45. McManus R, Ioussoufovitch S, Froats E, St Lawrence K, van Uum S, Diop M. Dynamic response of cerebral blood flow to insulin-induced hypoglycemia. *Scientific Reports*. 2020;10(1):1-10. doi:10.1038/s41598-020-77626-6
46. Li Y, Guo L, Li L, et al. Early Diagnosis of Type 2 Diabetes Based on Near-Infrared Spectroscopy Combined With Machine Learning and Aquaphotomics. *Frontiers in Chemistry*. 2020;8:580489. doi:10.3389/fchem.2020.580489

47. Brown CD, Davis HT, Ediger MN, Fleming CM, Hull EL, Rohrscheib M. Clinical assessment of near-infrared spectroscopy for noninvasive diabetes screening. *Diabetes Technology and Therapeutics*. 2005;7(3):456-466. doi:10.1089/dia.2005.7.456
48. Molinari F, Acharya UR, Martis RJ, de Luca R, Petraroli G, Liboni W. Entropy analysis of muscular near-infrared spectroscopy (NIRS) signals during exercise programme of type 2 diabetic patients: Quantitative assessment of muscle metabolic pattern. *Computer Methods and Programs in Biomedicine*. 2013;112(3):518-528. doi:10.1016/j.cmpb.2013.08.018
49. Robinson MR, Eaton RP, Haaland DM, et al. Noninvasive Glucose Monitoring in Diabetic Patients: A Preliminary Evaluation. *Clinical Chemistry*. 1992;38(9):1618-1622. doi:10.1093/clinchem/38.9.1618
50. Jeon KJ, Hwang ID, Hahn S, Yoon G. Comparison between transmittance and reflectance measurements in glucose determination using near infrared spectroscopy. *Journal of Biomedical Optics*. 2006;11(1):014022. doi:10.1117/1.2165572
51. St Lawrence K, Verdecchia K, Elliott J, et al. Kinetic model optimization for characterizing tumour physiology by dynamic contrast-enhanced near-infrared spectroscopy. *Physics in medicine and biology*. 2013;58(5):1591-1604. doi:10.1088/0031-9155/58/5/1591
52. Milej D, Abdalmalak A, Desjardins L, et al. Quantification of blood-brain barrier permeability by dynamic contrast-enhanced NIRS. *Scientific Reports*. 2017;7(1):1-8. doi:10.1038/s41598-017-01922-x
53. Busch DR, Balu R, Baker WB, et al. Detection of Brain Hypoxia Based on Noninvasive Optical Monitoring of Cerebral Blood Flow with Diffuse Correlation Spectroscopy. *Neurocritical Care*. 2019;30(1):72-80. doi:10.1007/s12028-018-0573-1

54. Diop M, Tichauer KM, Elliott JT, Migueis M, Lee T-Y, Lawrence K. Time-resolved near-infrared technique for bedside monitoring of absolute cerebral blood flow. In: Vo-Dinh T, Grundfest WS, Mahadevan-Jansen A, eds. *Advanced Biomedical and Clinical Diagnostic Systems VIII*. Vol 7555. SPIE; 2010:75550Z. doi:10.1117/12.842521
55. Abdalmalak A, Milej D, Cohen DJF, et al. Using fMRI to investigate the potential cause of inverse oxygenation reported in fNIRS studies of motor imagery. *Neuroscience Letters*. 2020;714:134607. doi:10.1016/j.neulet.2019.134607
56. Cohen DJF. Monte-Carlo Simulations of Near-infrared Light Propagation in the Adult Human Head. *2019 Undergraduate Awards*. Published online January 1, 2019. Accessed April 22, 2021. https://ir.lib.uwo.ca/undergradawards_2019/8
57. Lane LA, Xue R, Nie S. Emergence of two near-infrared windows for in vivo and intraoperative SERS. *Current Opinion in Chemical Biology*. 2018;45:95-103. doi:10.1016/j.cbpa.2018.03.015
58. Shi L, Sordillo LA, Rodríguez-Contreras A, Alfano R. Transmission in near-infrared optical windows for deep brain imaging. *Journal of Biophotonics*. 2016;9(1-2):38-43. doi:10.1002/jbio.201500192
59. Jacques SL. Optical properties of biological tissues: A review. *Physics in Medicine and Biology*. 2013;58(11):R37. doi:10.1088/0031-9155/58/11/R37
60. Barstow TJ. Understanding near infrared spectroscopy and its application to skeletal muscle research. *Journal of Applied Physiology*. 2019;126(5):1360-1376. doi:10.1152/jappphysiol.00166.2018
61. Cui W, Kumar C, Chance B. Experimental study of migration depth for the photons measured at sample surface. In: *Time-Resolved Spectroscopy and Imaging of Tissues*. Vol 1431. SPIE; 1991:180-191. doi:10.1117/12.44189

62. Delpy DT, Cope M. Quantification in tissue near-infrared spectroscopy. *Philosophical Transactions of the Royal Society B: Biological Sciences*. 1997;352(1354):649-659. doi:10.1098/rstb.1997.0046
63. Beek JF, Blokland P, Posthumus P, et al. In vitro double-integrating-sphere optical properties of tissues between 630 and 1064 nm. *Physics in Medicine and Biology*. 1997;42(11):2255-2261. doi:10.1088/0031-9155/42/11/017
64. Cheong WF, Prahl SA, Welch AJ. A Review of the Optical Properties of Biological Tissues. *IEEE Journal of Quantum Electronics*. 1990;26(12):2166-2185. doi:10.1109/3.64354
65. Anderson RR, Parrish JA. Optical Properties of Human Skin. In: *The Science of Photomedicine*. Springer US; 1982:147-194. doi:10.1007/978-1-4684-8312-3_6
66. Spectral linear scattering coefficient | CIE. Accessed April 22, 2021. <https://cie.co.at/eilvterm/17-24-084>
67. Abdalmalak A. Detecting Command-Driven Brain Activity in Patients with Disorders of Consciousness Using TR-fNIRS. *Electronic Thesis and Dissertation Repository*. Published online June 15, 2020. Accessed April 22, 2021. <https://ir.lib.uwo.ca/etd/7055>
68. Fukutomi D, Ishii K, Awazu K. Determination of the scattering coefficient of biological tissue considering the wavelength and absorption dependence of the anisotropy factor. *Optical Review*. 2016;23(2):291-298. doi:10.1007/s10043-015-0161-y
69. Schmitt JM, Kumar G. Turbulent nature of refractive-index variations in biological tissue. *Optics Letters*. 1996;21(16):1310. doi:10.1364/ol.21.001310
70. Bryant F. Snell's Law of Refraction. *Physics Bulletin*. 1958;9(12):317-317. doi:10.1088/0031-9112/9/12/004

71. Douplik A, Saiko G, Schelkanova I, Tuchin V v. The response of tissue to laser light. In: *Lasers for Medical Applications: Diagnostics, Therapy and Surgery*. Elsevier Ltd; 2013:47-109. doi:10.1533/9780857097545.1.47
72. Pogue BW, Jiang S, Dehghani H, et al. Characterization of hemoglobin, water, and NIR scattering in breast tissue: analysis of intersubject variability and menstrual cycle changes. *Journal of Biomedical Optics*. 2004;9(3):541. doi:10.1117/1.1691028
73. John D. *Effects of Light Absorption and Scattering in Water Samples on OBS® Measurements.*; 2008.
74. Matcher SJ, Cope M, Delpy DT. Use of the water absorption spectrum to quantify tissue chromophore concentration changes in near-infrared spectroscopy. *Physics in Medicine and Biology*. 1994;39(1):177-196. doi:10.1088/0031-9155/39/1/011
75. Matcher SJ, Elwell CE, Cooper CE, Cope M, Delpy DT. Performance comparison of several published tissue near-infrared spectroscopy algorithms. *Analytical Biochemistry*. 1995;227(1):54-68. doi:10.1006/abio.1995.1252
76. Hollis VS. Non-invasive monitoring of brain tissue temperature by near-infrared spectroscopy. *Doctoral thesis, UCL (University College London)* . Published online 2002.
77. Rajaram A, Milej D, Suwalski M, et al. Optical monitoring of cerebral perfusion and metabolism in adults during cardiac surgery with cardiopulmonary bypass. *Biomedical Optics Express*. 2020;11(10):5967. doi:10.1364/boe.404101
78. Durduran T, Zhou C, Buckley EM, et al. Optical measurement of cerebral hemodynamics and oxygen metabolism in neonates with congenital heart defects. *Journal of Biomedical Optics*. 2010;15(3):037004. doi:10.1117/1.3425884
79. Keep RF, Hua Y, Xi G. Brain Water Content: A Misunderstood Measurement? *Translational Stroke Research*. 2012;3(2):263-265. doi:10.1007/s12975-012-0152-2

80. Fatouros PP, Marmarou A. Use of magnetic resonance imaging for in vivo measurements of water content in human brain: Method and normal values. *Journal of Neurosurgery*. 1999;90(1):109-115. doi:10.3171/jns.1999.90.1.0109
81. Yeganeh HZ, Toronov V, Elliott JT, Diop M, Lee T-Y, Lawrence K. Broadband continuous-wave technique to measure baseline values and changes in the tissue chromophore concentrations. *Biomedical Optics Express*. 2012;3(11):2761. doi:10.1364/boe.3.002761
82. Kewin M, Rajaram A, Milej D, et al. Evaluation of hyperspectral NIRS for quantitative measurements of tissue oxygen saturation by comparison to time-resolved NIRS. *Biomedical Optics Express*. 2019;10(9). doi:10.1364/BOE.10.004789
83. Caspers PJ, Lucassen GW, Carter EA, Bruining HA, Puppels GJ. In vivo confocal raman microspectroscopy of the skin: Noninvasive determination of molecular concentration profiles. *Journal of Investigative Dermatology*. 2001;116(3):434-442. doi:10.1046/j.1523-1747.2001.01258.x
84. Iorizzo TW, Jermain PR, Salomatina E, Muzikansky A, Yaroslavsky AN. Temperature induced changes in the optical properties of skin in vivo. *Scientific Reports*. 2021;11(1):754. doi:10.1038/s41598-020-80254-9
85. Bouguer P. *Essai d'optique Sur La Gradation de La Lumière*. Claude Jombert; 1729. Accessed April 26, 2021. https://archive.org/details/UFIE003101_TO0324_PNI-2703_000000
86. Hahlweg C, Meißner B, Zhao W, Rothe H. The idea of the Lambertian surface: history, idealization, and system theoretical aspects and part 1 of a lost chapter on multiple reflection. In: Gu Z-H, Hanssen LM, eds. *Reflection, Scattering, and Diffraction from Surfaces II*. Vol 7792. SPIE; 2010:779202. doi:10.1117/12.860172

87. Lambert JH. *Photometria Sive de Mensura et Gradibus Luminis, Colorum et Umbrae*. Eberhardt Klett; 1760. Accessed April 26, 2021.
https://archive.org/details/TO0E039861_TO0324_PNI-2733_000000
88. Beer. Bestimmung der Absorption des rothen Lichts in farbigen Flüssigkeiten. *Annalen der Physik*. 1852;162(5):78-88. doi:10.1002/andp.18521620505
89. Beer–Lambert law (or Beer–Lambert–Bouguer law). In: *IUPAC Compendium of Chemical Terminology*. IUPAC; 2008. doi:10.1351/goldbook.b00626
90. Delpy DT, Cope M, van der Zee P, Arridge S, Wray S, Wyatt J. Estimation of optical pathlength through tissue from direct time of flight measurement. *Physics in Medicine and Biology*. 1988;33(12):1433-1442. doi:10.1088/0031-9155/33/12/008
91. Kocsis L, Herman P, Eke A. The modified Beer-Lambert law revisited. *Physics in Medicine and Biology*. 2006;51(5):N91. doi:10.1088/0031-9155/51/5/N02
92. Delpy DT, Cope M, van der Zee P, Arridge S, Wray S, Wyatt J. Estimation of optical pathlength through tissue from direct time of flight measurement. *Physics in Medicine and Biology*. 1988;33(12):1433-1442. doi:10.1088/0031-9155/33/12/008
93. Hiraoka M, Firbank M, Essenpreis M, et al. A Monte Carlo investigation of optical pathlength in inhomogeneous tissue and its application to near-infrared spectroscopy. *Physics in Medicine and Biology*. 1993;38(12):1859-1876.
doi:10.1088/0031-9155/38/12/011
94. Delpy DT, Cope M, van der Zee P, Arridge S, Wray S, Wyatt J. Estimation of optical pathlength through tissue from direct time of flight measurement. *Physics in Medicine and Biology*. 1988;33(12):1433-1442. doi:10.1088/0031-9155/33/12/008
95. Auger H, Bherer L, Boucher É, Hoge R, Lesage F, Dehaes M. Quantification of extra-cerebral and cerebral hemoglobin concentrations during physical exercise

- using time-domain near infrared spectroscopy. *Biomedical Optics Express*. 2016;7(10):3826. doi:10.1364/boe.7.003826
96. Kienle A, Patterson MS. Improved solutions of the steady-state and the time-resolved diffusion equations for reflectance from a semi-infinite turbid medium. *Journal of the Optical Society of America A*. 1997;14(1):246. doi:10.1364/josaa.14.000246
97. Kacprzak M, Liebert A, Sawosz P, Żolek N, Maniewski R. Time-resolved optical imager for assessment of cerebral oxygenation. *Journal of Biomedical Optics*. 2007;12(3):034019. doi:10.1117/1.2743964
98. Patterson MS, Chance B, Wilson BC. Time resolved reflectance and transmittance for the noninvasive measurement of tissue optical properties. *Applied Optics*. 1989;28(12):2331. doi:10.1364/ao.28.002331
99. Kienle A, Glanzmann T, Wagnières G, van den Bergh H. Investigation of two-layered turbid media with time-resolved reflectance. *Applied Optics*. 1998;37(28):6852. doi:10.1364/ao.37.006852
100. Alberts B, Johnson A, Lewis J, Raff M, Roberts K, Walter P. Electron-Transport Chains and Their Proton Pumps. In: *Molecular Biology of the Cell*. 4th ed. Garland Science; 2002. Accessed April 27, 2021. <https://www.ncbi.nlm.nih.gov/books/NBK26904/>
101. Miyamoto O, Auer RN. Hypoxia, hyperoxia, ischemia, and brain necrosis. *Neurology*. 2000;54(2):362-371. doi:10.1212/wnl.54.2.362
102. Sendoel A, Hengartner MO. Apoptotic Cell Death Under Hypoxia. *Physiology*. 2014;29(3):168-176. doi:10.1152/physiol.00016.2013
103. Pittman RN. Regulation of Tissue Oxygenation. In: *Regulation of Tissue Oxygenation*. Morgan & Claypool Life Sciences; 2011. Accessed April 27, 2021. <https://www.ncbi.nlm.nih.gov/books/NBK54103/>

104. Arifler D, Zhu T, Madaan S, Tachtsidis I. Optimal wavelength combinations for near-infrared spectroscopic monitoring of changes in brain tissue hemoglobin and cytochrome c oxidase concentrations. *Biomedical Optics Express*. 2015;6(3):933. doi:10.1364/boe.6.000933
105. Rajaram A, Bale G, Kewin M, et al. Simultaneous monitoring of cerebral perfusion and cytochrome c oxidase by combining broadband near-infrared spectroscopy and diffuse correlation spectroscopy. *Biomedical Optics Express*. 2018;9(6):2588. doi:10.1364/boe.9.002588
106. Gagnon L, Gauthier C, Hoge RD, Lesage F, Selb J, Boas DA. Double-layer estimation of intra- and extracerebral hemoglobin concentration with a time-resolved system. *Journal of Biomedical Optics*. 2008;13(5):054019. doi:10.1117/1.2982524
107. Denault AY, Shaaban-Ali M, Cournoyer A, Benkreira A, Mailhot T. Near-Infrared Spectroscopy. In: *Neuromonitoring Techniques*. Elsevier; 2018:179-233. doi:10.1016/B978-0-12-809915-5.00007-3
108. Wilson BA. Cognitive functioning of adult survivors of cerebral hypoxia. *Brain Injury*. 1996;10(12):863-874. doi:10.1080/026990596123846
109. Lange F, Tachtsidis I. Clinical Brain Monitoring with Time Domain NIRS: A Review and Future Perspectives. *Applied Sciences*. 2019;9(8):1612. doi:10.3390/app9081612
110. The Radiology Assistant : Vascular territories. Accessed June 9, 2021. <https://radiologyassistant.nl/neuroradiology/brain-ischemia/vascular-territories>
111. Diop M, Tichauer KM, Elliott JT, Migueis M, Lee T-Y, Lawrence K st. Comparison of time-resolved and continuous-wave near-infrared techniques for measuring cerebral blood flow in piglets. *Journal of Biomedical Optics*. 2010;15(5):057004. doi:10.1117/1.3488626

112. Ijichi S, Kusaka T, Isobe K, et al. Developmental changes of optical properties in neonates determined by near-infrared time-resolved spectroscopy. *Pediatric Research*. 2005;58(3):568-573. doi:10.1203/01.PDR.0000175638.98041.0E
113. Rajaram A, Yip LCM, Milej D, et al. Perfusion and Metabolic Neuromonitoring during Ventricular Taps in Infants with Post-Hemorrhagic Ventricular Dilatation. *Brain Sciences*. 2020;10(7):452. doi:10.3390/brainsci10070452
114. Arora R, Ridha M, Lee DSC, et al. Preservation of the metabolic rate of oxygen in preterm infants during indomethacin therapy for closure of the ductus arteriosus. *Pediatric Research*. 2013;73(6):713-718. doi:10.1038/pr.2013.53
115. Li Z, Park BK, Liu W, et al. A statistical skull geometry model for children 0-3 years old. *PLoS ONE*. 2015;10(5). doi:10.1371/journal.pone.0127322
116. Selb J, Ogden TM, Dubb J, Fang Q, Boas DA. Comparison of a layered slab and an atlas head model for Monte Carlo fitting of time-domain near-infrared spectroscopy data of the adult head. *Journal of Biomedical Optics*. 2014;19(1):016010. doi:10.1117/1.JBO.19.1.016010
117. Selb J, Boas DA, Chan S-T, Evans KC, Buckley EM, Carp SA. Sensitivity of near-infrared spectroscopy and diffuse correlation spectroscopy to brain hemodynamics: simulations and experimental findings during hypercapnia. *Neurophotonics*. 2014;1(1):015005. doi:10.1117/1.NPh.1.1.015005
118. Strangman GE, Li Z, Zhang Q. Depth Sensitivity and Source-Detector Separations for Near Infrared Spectroscopy Based on the Colin27 Brain Template. Zuo X-N, ed. *PLoS ONE*. 2013;8(8):e66319. doi:10.1371/journal.pone.0066319
119. Wojtkiewicz S, Sawosz P, Milej D, Treszcjanowicz J, Liebert A. Development of a Multidistance Continuous Wave Near-Infrared Spectroscopy Device with Frequency Coding. In: *Biomedical Optics 2014 (2014), Paper BM3A.24*. The Optical Society; 2014:BM3A.24. doi:10.1364/biomed.2014.bm3a.24

120. Abdalmalak A, Milej D, Diop M, et al. Can time-resolved NIRS provide the sensitivity to detect brain activity during motor imagery consistently? *Biomedical Optics Express*. 2017;8(4):2162. doi:10.1364/boe.8.002162
121. Pifferi A, Contini D, Mora AD, Farina A, Spinelli L, Torricelli A. New frontiers in time-domain diffuse optics, a review. *Journal of Biomedical Optics*. 2016;21(9):091310. doi:10.1117/1.jbo.21.9.091310
122. Milej D, Abdalmalak A, McLachlan P, Diop M, Liebert A, st. Lawrence Keith. Subtraction-based approach for enhancing the depth sensitivity of time-resolved NIRS. *Biomedical Optics Express*. 2016;7(11):4514. doi:10.1364/boe.7.004514
123. Helton M, Mycek M-A, Vishwanath K. Direct estimation of the reduced scattering coefficient from experimentally measured time-resolved reflectance via Monte Carlo based lookup tables. *Biomedical Optics Express*. 2020;11(8):4366. doi:10.1364/boe.398256
124. Cohen DJF, Diop M. Late-photons hyperspectral near-infrared spectroscopy improves the sensitivity to cerebral oxygenation in adults. In: *Optics InfoBase Conference Papers*. Vol Part F176-BRAIN-2020. OSA - The Optical Society; 2020:BTh3C.2. doi:10.1364/BRAIN.2020.BTh3C.2
125. Reiter D. The Monte Carlo method, an introduction. *Lecture Notes in Physics*. 2008;739:63-78. doi:10.1007/978-3-540-74686-7_3
126. Rubinstein RY, Kroese DP. *Simulation and the Monte Carlo Method*. John Wiley & Sons, Inc.; 2007. doi:10.1002/9780470230381
127. Yan S, Fang Q. Hybrid mesh and voxel based Monte Carlo algorithm for accurate and efficient photon transport modeling in complex bio-tissues. *Biomedical Optics Express*. 2020;11(11):6262. doi:10.1364/boe.409468
128. Fang Q, Boas DA. Monte Carlo Simulation of Photon Migration in 3D Turbid Media Accelerated by Graphics Processing Units. *Optics Express*. 2009;17(22):20178. doi:10.1364/oe.17.020178

129. Badano A. In silico imaging clinical trials: cheaper, faster, better, safer, and more scalable. *Trials*. 2021;22(1):64. doi:10.1186/s13063-020-05002-w

Chapter 2

2 Estimating adult cerebral oxygen saturation from time-resolved near-infrared spectroscopy measurements with few discrete wavelengths at a single source-detector distance

This chapter is adapted from a proceeding paper titled: “Estimating adult cerebral oxygen saturation from time-resolved near-infrared spectroscopy measurements with few discrete wavelengths at a single source-detector distance” published in Proceedings Volume 11639, Optical Tomography and Spectroscopy of Tissue XIV in 2021 by David Jonathan Fulop Cohen, Natalie C. Li, and Mamadou Diop.

2.1 Abstract

Time-resolved Near-Infrared Spectroscopy (TR-NIRS) methods typically use multiple wavelengths and source-detector distances in conjunction with a solution of the diffusion approximation to quantify tissue blood content and oxygenation. This approach can be both computationally intensive and costly, as multiple detectors are required. We propose a novel two-layer fitting approach for multi-wavelength TR-NIRS, which uses a single detector while providing accurate estimates of cerebral oxygen saturation (ScO_2) and hemoglobin content. The method uses a multi-step fitting algorithm to establish rough estimates of the absorption and scattering coefficients in the extracerebral layer and the brain, and subsequently refine those estimates, to improve accuracy while reducing crosstalk and complexity. Validation was conducted using Monte Carlo simulations in a realistic adult head model with appropriate optical properties at 680nm, 750nm, 800nm, and 830nm. The detector was located 30 mm anteriorly from the source, which was placed 50 mm above the right temple. Scalp oxygen saturation (SO_2) (50%, 60%, and 70%) and ScO_2 (40%-80%, 2% increments) were varied independently. The recovered ScO_2 had a difference (mean \pm standard deviation) of $2.31\pm 2.93\%$ from inputted values, and cerebral total hemoglobin was recovered with a difference of $2.94\pm 3.47\%$. Such high accuracy demonstrates the robustness of this computationally efficient two-layer fitting approach for analyzing multi-wavelength TR-NIRS measurements acquired with a single

detector. Future work will involve validating the technique in tissue mimicking phantoms and animal studies.

2.2 Introduction

Intraoperative brain injury is a serious complication of cardiac surgery that is currently difficult to detect since there are few clinically significant signs or symptoms while the patient is under general anesthesia¹⁻⁴. Time-resolved near-infrared spectroscopy (TR-NIRS) could address this clinical need, as it is sensitive to cerebral oxygen saturation (ScO₂), an important biomarker for brain health⁵⁻⁸. Additionally, because TR-NIRS measures regional ScO₂ rather than specifically arterial or venous oxygen saturation, it can be used to assess regional tissue wellbeing⁹.

TR-NIRS measurements are typically analyzed using simple analytical solutions of the diffusion approximation (DA) to the radiative transport equation, which assumes that the head is a homogenous medium¹⁰. While this assumption is reasonable for neonates¹¹, given the smaller contribution of their thin extracerebral layers (ECL) to the optical signal, it is inappropriate for adults where skull thickness can reach more than 10 mm¹². More advanced algorithms use a two-layer approach to distinguish the ECL and brain signals¹³; however, they often require fitting many source-detector distances simultaneously to better constrain the estimation of ScO₂ and cerebral blood content^{13, 14}. Given the complexity and cost of current TR-NIRS devices, it is desirable to minimize the number of detectors required to achieve accurate estimates of ScO₂ and blood content. In this work, we propose a two-layer fitting approach for multi-wavelength TR-NIRS, capable of recovering ScO₂ and total hemoglobin concentration in the brain with high accuracy using a single source detector distance. The accuracy of this method was tested using *in silico* data generated from a segmented adult head model to closely mimic tissue geometry and optical properties. The reduction in the number of detectors required to achieve high accuracy makes this method very attractive compared to the multi-detector methods commonly reported in the literature.

2.3 Methods

2.3.1 Monte Carlo Simulations

Monte-Carlo simulations were conducted to validate the two-layer fitting method described below. A four-layer head model, consisting of scalp, skull, cerebrospinal fluid (CSF), and brain tissue, was previously segmented from a 3D MRI of an adult human head¹⁵. Each layer was assigned optical properties (absorptions, scattering, anisotropic factor, and refractive index) characteristic of the tissue they represent and were adjusted appropriately depending on the simulated wavelength¹⁶. For the scalp and brain tissues, the absorption coefficients (μ_a) were calculated using Equation 2.1¹⁶, where λ is the wavelength of light, ε_{Water} , ε_{Hb} , and ε_{HbO_2} are the extinction coefficients of water, deoxyhemoglobin, and oxyhemoglobin, respectively, and WF (water fraction), C_{Hb} , and C_{HbO_2} were their respective tissue concentrations.

$$\mu_a(\lambda) = \varepsilon_{Water}(\lambda) * WF + \varepsilon_{Hb}(\lambda) * C_{Hb} + \varepsilon_{HbO_2}(\lambda) * C_{HbO_2}, \quad (2.1)$$

This allowed for the generation of a wide range of brain-scalp oxygen saturation (SO₂) pairs. Notably, Monte Carlo simulations^{17, 18} were conducted with ScO₂ ranging from 40% to 80% in 2% increments, with three distinct scalp oxygen saturations (50%, 60%, and 70%) simulated for each ScO₂. For each brain-scalp SO₂ pair, the wavelengths simulated were 680 nm, 750 nm, 800 nm, and 830 nm. These wavelengths were chosen due to their wide coverage of the first optical window, wide availability for experimental implementation, and prevalence in the literature for monitoring oxy- and deoxyhemoglobin¹⁹⁻²¹. Each simulation used 3 billion photons to obtain a realistic signal-to-noise ratio. In all simulations, the source was located 50 mm above the right temple, where the mean extracerebral thickness is approximately 12 mm, and a detector was positioned 30 mm anteriorly, as shown in Figure 2.1. Due to GPU memory limitations, only one octant of the full head volume was simulated.

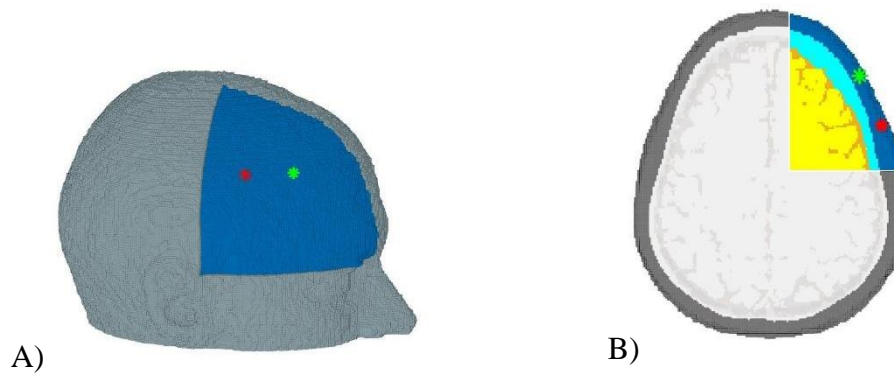


Figure 2.1: Four-layer adult head model used for the Monte Carlo simulations: A) full head model and B) cross-section along the source-detector plane. The four layers are the scalp (dark blue), skull (cyan), cerebrospinal fluid (orange), and brain tissue (yellow). Though the full head was segmented, only the portion shown in colour was used in the simulations due to GPU memory limitations. The source (red star) and the detector (green star) are located 3 cm apart.

2.3.2 Data Analysis

The two-layer analysis is prone to crosstalk because of the larger number of fitting parameters (five). As such, a multi-step approach is implemented to reduce crosstalk between the variables. The first step is to obtain a rough estimate of the optical properties in both layers, while the second step refines those initial estimates.

The rough estimates of the optical properties are obtained using two techniques. The first approach is a two-stage homogenous fitting of each temporal point-spread function (TPSF) to recover the absorption coefficient of the extracerebral layer (ECL) and the mean reduced scattering coefficient of the entire volume of tissue probed by the optical signal. Note that even at a 30 mm source-detector distance, the ECL contribution dominates the TPSF in the region of interest (50% of the maximum signal before the peak, to 5% after). As such, fitting the TPSFs with a homogenous model²² to obtain a rough estimate of the optical properties of the ECL is reasonable. The first stage of the homogenous fitting is used to calculate the mean amplitude (i.e., the multiplication factor that is used to account for the variable number of detected photons in the Monte Carlo

simulations) of the optical signal for the four wavelengths. Fixing the amplitude to the mean value for a second homogenous fitting of the same four TPSFs reduces the crosstalk between the amplitude term and the other fitting parameters, and results in more stable estimates of the absorption coefficients of the ECL and scattering coefficients. Assuming an average scattering for the whole head rather than unique scatterings for the top and bottom layers of the two-layer fitting reduces the complexity of the fitting algorithm and computation time and did not impact accuracy.

The TPSFs are then fit between 5% and 1% of the maximum signal after the peak using Equation 2.2; R is the reflectance, t is time, c is the speed of light in a vacuum, and n is the refractive index of the tissue, which was set to 1.4. Equation 2.2 is used to estimate the absorption coefficients of the brain tissue because the tail of the TPSF is more sensitive to the bottom layer (brain) absorption coefficient; late-arriving photons have a longer pathlength and are therefore more likely to have interrogated deeper tissue²³.

$$\mu_a(\lambda) = -\frac{\frac{\partial(R(\lambda,t))}{\partial t}}{\frac{c}{n}} \quad (2.2)$$

Once the initial estimate of the absorption coefficients in both layers and the homogenous reduced scattering coefficients are obtained, the two-layer fitting algorithm is used to refine the estimates. The two-layer fitting algorithm uses the two-layer solution to the DA developed by Kienle *et al.* in 1998²⁴. To leverage the spectral information provided by the four wavelengths, the concentrations of oxy- and deoxyhemoglobin are calculated from the absorption coefficients of the ECL and brain, using Eq. 1 and assuming 80% water fraction. Similar to the two-stage homogenous fitting routine, the two-layer fitting is conducted in two stages. The first stage refines the concentrations in the ECL, while the second refines the concentrations in the brain tissue. In the first stage, the concentrations, amplitude, and reduced scattering coefficient estimated from the homogenous fitting are assigned as the initial values, and the top layer (ECL) thickness is set to a known *a priori* value obtained from the head segmentation. In a clinical setting, such information can be obtained from a prior MRI or CT scan. During the first stage of the fitting the ECL concentrations are constrained to vary within $\pm 10\%$ from the initial

estimate. The refined ECL concentrations are then fixed during the second stage of the fitting for which the concentrations of oxy- and deoxyhemoglobin in the brain are the only fitting parameters.

Once refined estimates of the brain oxy- and deoxyhemoglobin have been calculated, Equations 2.3 and 2.4 are used to compute the total hemoglobin and ScO₂, respectively:

$$C_{HbT} = C_{HbO_2} + C_{Hb} \quad (2.3)$$

$$ScO_2 = \frac{C_{HbO_2}}{(C_{Hb} + C_{HbO_2})} * 100\% \quad (2.4)$$

2.4 Results

2.4.1 Simulations

A total of 264 simulations were conducted in the four-layer head model to validate the TR-NIRS data analysis algorithm. To test the validity of the semi-infinite medium assumption, the trajectories of the photons which reached the detector were analyzed in a sample (20) of the simulations. Since no photons that made it to the detector had interacted with the simulation boundary, it was concluded that the assumption was valid despite simulating an octant rather than the full volume of the head. Additionally, a negligible number of photons reached the simulation boundary in the first 1.5 ns after the simulated photon pulse (the maximum time of interest), which further supports our postulate that using only one octant of the full head does not impact the validity of the simulations.

2.4.2 Data analysis

The two-layer multi-wavelength analysis takes approximately 27.8 seconds per set of four TPSFs. The recovered cerebral oxy- and deoxyhemoglobin concentrations are displayed in Figure 2.2. The difference (mean± standard deviation) between the simulated and recovered oxyhemoglobin is 4.64±5.68% with a very strong correlation coefficient of 0.9976 between the estimated values and the ground truth. The minimum and maximum percent differences for the recovered oxyhemoglobin are 0.0% and 14.1%,

respectively. Deoxyhemoglobin was recovered with a similar accuracy (mean± standard deviation) of $2.88\pm 3.03\%$, and a correlation coefficient of 0.9993 when compared to the true values. The percent differences for the deoxyhemoglobin ranged from 0.1% and 10.0%.

The ScO₂ and total cerebral hemoglobin calculated from the cerebral concentrations of oxy- and deoxyhemoglobin are summarized in Figure 2.3. The recovered ScO₂ is strongly correlated with the simulated ScO₂ (0.9987), with a difference (mean± standard deviation) of $2.31\pm 2.93\%$, with a minimum and maximum difference of 0.1% and 7.7%, respectively. Similarly, the cerebral total hemoglobin was recovered with a difference (mean± standard deviation) of $2.94\pm 3.47\%$, with a minimum difference of 0.2% and maximum difference of 7.1%.

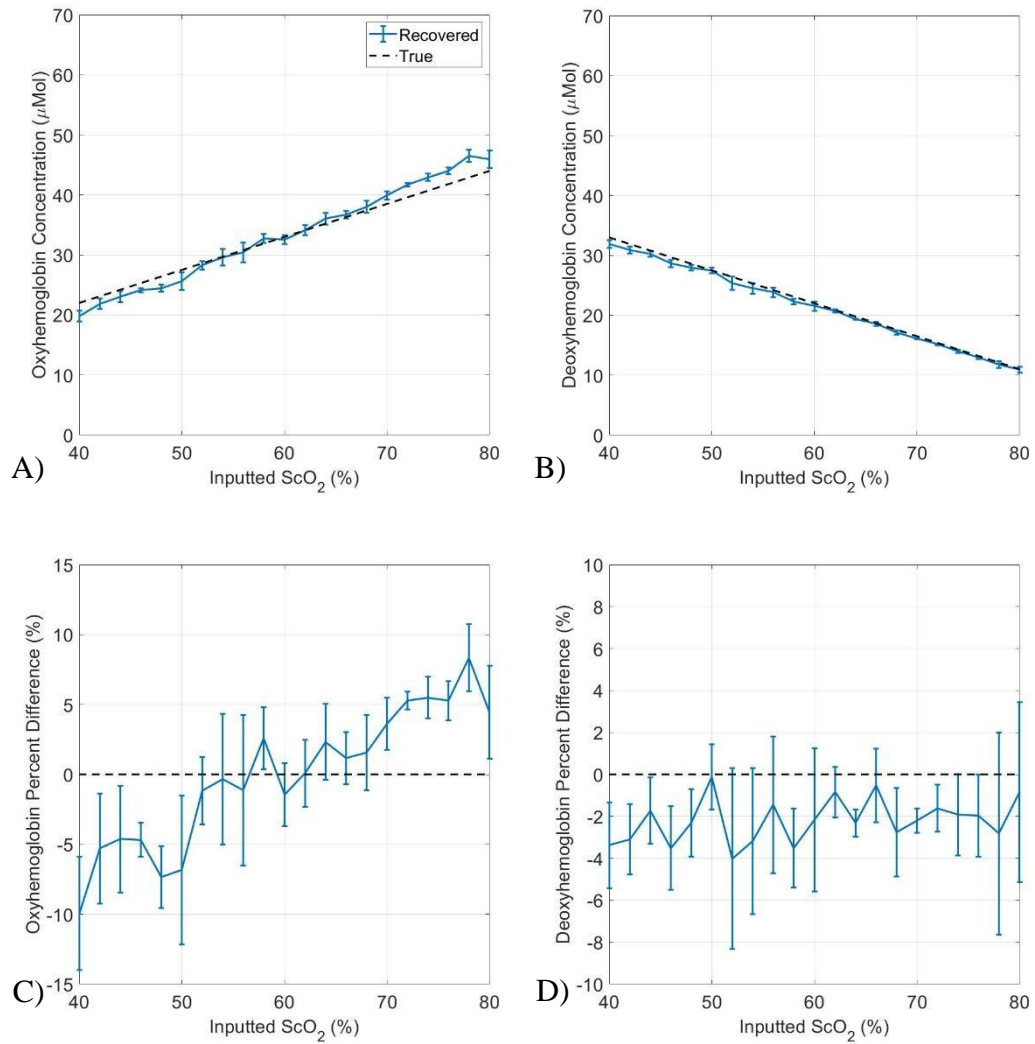


Figure 2.2: Recovered cerebral oxy- (A) and deoxyhemoglobin (B) concentrations for each ScO_2 . The values plotted in blue are the recovered values, while the dotted black line represents the inputted concentrations. (C) and (D) show the percent differences between the recovered concentrations and the simulated values.

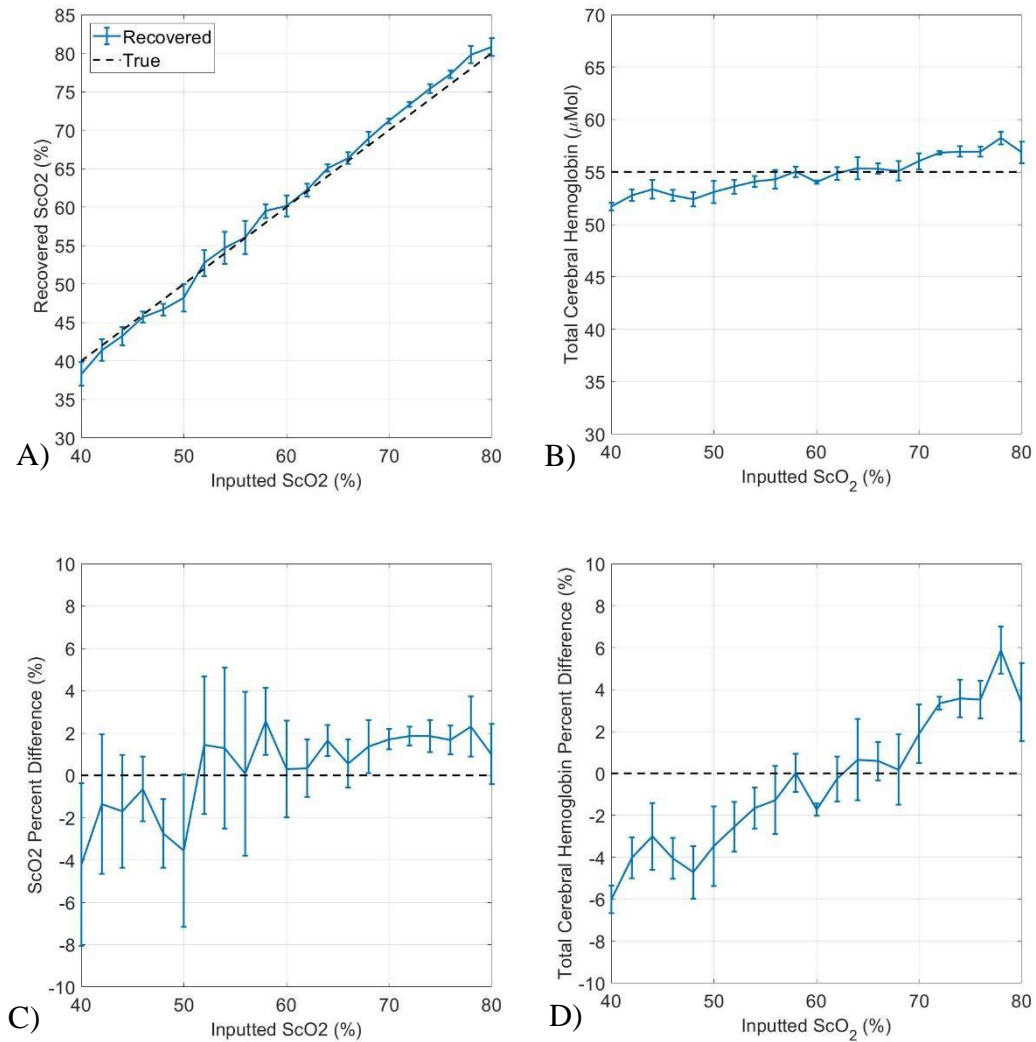


Figure 2.3: Recovered ScO₂ (A) and total hemoglobin concentration (B) for each simulated ScO₂. In both cases, the mean and standard deviation values are calculated across skin oxygenation, for each inputted ScO₂. The recovered values are plotted in blue, while the dotted black line represents the true values. (C) and (D) show the percent differences between the recovered values and the ground truth.

2.5 Discussion

In this study, a two-layer fitting algorithm that can recover *adult* cerebral oxygen saturation and total hemoglobin from multi-wavelength TR-NIRS measurements, acquired from a single detector, was developed and evaluated using Monte-Carlo

simulations. The analysis reveals a strong correlation between the recovered and the simulated values, with sub 5% mean percent differences. This method has greater accuracy for deoxyhemoglobin than for oxyhemoglobin. This is further shown examining the absolute concentrations, where deoxyhemoglobin is recovered with a mean absolute difference of $0.61 \pm 0.66 \mu\text{Mol}$, while oxyhemoglobin is recovered with a mean absolute difference of $1.53 \pm 1.83 \mu\text{Mol}$. As shown in Figure 2.2, the recovery of oxyhemoglobin is overestimated when ScO_2 is high, while underestimated when ScO_2 is low. This is likely a result of the wavelengths selected for the analysis; two wavelengths (680 nm and 750 nm) correspond to the region where deoxyhemoglobin has a higher extinction coefficient, while only one wavelength (830 nm) is in the region where oxyhemoglobin has stronger absorption. The same trend is observed for ScO_2 and total hemoglobin, as the concentration of oxyhemoglobin is used in their estimation. The mean absolute differences for ScO_2 and cerebral total hemoglobin are $1.31 \pm 1.57\%$ and $1.62 \pm 1.91 \mu\text{Mol}$, respectively.

The high accuracy of this method should allow for non-invasive measurement of ScO_2 and blood content at the bedside. With the average age of the population continuing to increase, an increasing number of seniors will require heart surgery, which is associated with a high risk of intraoperative brain injury. Previous studies have shown that modifying cerebral oxygen delivery to maintain intraoperative cerebral oximeter values at the preoperative baseline significantly reduces instances of permanent post-operative stroke (0.97% vs 2.5%)²⁵. Thus, bedside neuromonitoring could enable real-time detection of oxygen desaturation events to allow timely initiation of treatment.

A potential limitation of this work is that the simulations did not include an instrument response function (IRF)²⁶. As such, we can only speculate on the potential effects of the IRF on the accuracy of the method; however, beside a slight increase in computational time needed for convolving the IRFs with the theoretical model, we do not anticipate significant differences from the findings of the current study. A second limitation is that the method requires *a priori* knowledge of the ECL thickness. This may be an issue in emergency situations where it will not be possible to measure the ECL thickness before surgery via MRI or CT imaging. However, with the additional spectral information

available from an increased number of wavelengths, it may be possible to estimate the ECL thickness which will increase the robustness of the method. Future work will involve evaluating this method with hyperspectral TR-NIRS data to test this hypothesis.

2.6 Conclusion

We have developed a robust method for accurate recovery of adult ScO₂ and hemoglobin content using a multi-wavelength two-layer analysis of TR-NIRS data acquired at a single detector. The method reliably recovers the absolute oxy- and deoxyhemoglobin concentrations, enabling accurate calculation of ScO₂ and total hemoglobin. Future work will involve further validation of this method in an animal model of the adult head, as well as expanding the number of wavelengths (i.e., hyperspectral TR-NIRS) to permit estimation of the ECL directly from the TR-NIRS measurements.

2.7 Acknowledgements

The authors would like to thank Dr. Vladislav Toronov for his insightful discussion about the two-layer analytical model. This work was supported by Start-Up Funds from the Schulich School of Medicine & Dentistry and the Lawson Health Research Institute, and an NSERC Discovery grant (06337-2017 RGPIN) and NSERC CGS-M scholarship.

2.8 References

1. Roach, G.W., et al., "Adverse cerebral outcomes after coronary bypass surgery. Multicenter Study of Perioperative Ischemia Research Group and the Ischemia Research and Education Foundation Investigators," *N Engl J Med.* 335(25), 1857-63 (1996).
2. Newman, M. F., et al., "Report of the substudy assessing the impact of neurocognitive function on quality of life 5 years after cardiac surgery," *Stroke* 32(12), 2874-81 (2001).
3. McKhann, G. M., et al., "Stroke and encephalopathy after cardiac surgery: an update," *Stroke* 37(2), 562-71 (2006).
4. Hogue, C. W. Jr., Palin, C. A., Arrowsmith, J. E., "Cardiopulmonary bypass management and neurologic outcomes: an evidence-based appraisal of current practices," *Anesth Analg.* 103(1), 21-37 (2006).
5. Cubeddu, R., et al., "Compact tissue oximeter based on dual-wavelength multichannel time-resolved reflectance," *Appl. Opt.* 38, 3670-3680 (1999).
6. Eda, H., et al., "Multichannel time-resolved optical tomographic imaging system," *Rev. Sci. Instrum.* 70(9), 3595-3602 (1999).
7. Schmidt, F. E., et al., "A 32-channel time-resolved instrument for medical optical tomography," *Rev. Sci. Instrum.* 71(1), 256-265 (2000).
8. Heise, H. M., [Medical Applications of NIR Spectroscopy. In: *Near-Infrared Spectroscopy*], Springer, Singapore, 437-473 (2020).
9. Diop, M., et al., "Comparison of time-resolved and continuous-wave near-infrared techniques for measuring cerebral blood flow in piglets," *J. Biomed. Opt.* 15(5), 057004 (2010).
10. Haskell, R. C. et al., "Boundary conditions for the diffusion equation in radiative transfer," *J. Opt. Soc. Am. A* 11, 2727-2741 (1994).
11. Ijichi, S, et al. "Developmental Changes of Optical Properties in Neonates Determined by Near-Infrared Time-Resolved Spectroscopy," *Pediatr Res* 58, 568–573 (2005).

12. De Boer, H. H. H., et al., "Human cranial vault thickness in a contemporary sample of 1097 autopsy cases: relation to body weight, stature, age, sex and ancestry." *Int. J. Legal Med.* 130(5), 1371-7 (2016).
13. Gagnon, L., et al., "Double-layer estimation of intra- and extracerebral hemoglobin concentration with a time-resolved system," *J. Biomed. Opt.* 13(5) 054019 (2008).
14. Martelli, F., Del Bianco, S. and Zaccanti, G., "Procedure for retrieving the optical properties of a two-layered medium from time-resolved reflectance measurements," *Opt. Lett.* 28(14), 1236-8 (2003).
15. Cohen, D. J. F. and Diop, M. "Late-Photons Hyperspectral Near-Infrared Spectroscopy Improves the Sensitivity to Cerebral Oxygenation in Adults," *Optics and the Brain, BTh3C.* 2 (2020).
16. Jacques, S. L., "Optical properties of biological tissues: a review," *Phys Med Biol.* 58(11), R37-61 (2013)
17. Yan, S. and Fang, Q., "Hybrid mesh and voxel based Monte Carlo algorithm for accurate and efficient photon transport modeling in complex bio-tissues," *Biomed. Opt. Express* 11(11), 6262-6270 (2020).
18. Fang, Q. and Boas, D., "Monte Carlo Simulation of Photon Migration in 3D Turbid Media Accelerated by Graphics Processing Units," *Opt. Express* 17(22), 20178-20190 (2009).
19. Sato, H., Kiguchi, M. and Maki, A. "Wavelength dependence of effective pathlength factor in noninvasive optical measurements of human brain functions," *Jpn. J. Appl. Phys.* 45(4L), L361 (2006).
20. Strangman, G., Franceschini, M. A. and Boas D. A., "Factors affecting the accuracy of near-infrared spectroscopy concentration calculations for focal changes in oxygenation parameters," *Neuroimage* 18(4), 865-79 (2003).
21. Scholkmann, F., et al., "A review on continuous wave functional near-infrared spectroscopy and imaging instrumentation and methodology," *Neuroimage* 85(Pt 1), 6-27 (2014).
22. Kienle, A. and Patterson, M. S., "Improved solutions of the steady-state and the time-resolved diffusion equations for reflectance from a semi-infinite turbid medium," *J. Opt. Soc. Am. A* 14, 246-254 (1997).

23. Diop, M. and St. Lawrence, K., "Improving the depth sensitivity of time-resolved measurements by extracting the distribution of times-of-flight." *Biomed. Opt. Express.* 4(3), 447-459 (2013).
24. Kienle, A., et al., "Investigation of two-layered turbid media with time-resolved reflectance," *Appl. Opt.* 37, 6852-6862 (1998).
25. Goldman, S., et al., "Optimizing intraoperative cerebral oxygen delivery using noninvasive cerebral oximetry decreases the incidence of stroke for cardiac surgical patients," *Heart Surg Forum* 7(5), E376-81 (2004)
26. Diop, M. and St. Lawrence, K., "Deconvolution method for recovering the photon time-of-flight distribution from time-resolved measurements." *Opt. Lett.* 37(12), 2358-2360 (2012).

Chapter 3

3 Fast Estimation of Adult Cerebral Oxygen Saturation and Total Hemoglobin using Hyperspectral Time-Resolved Near-Infrared Spectroscopy

This chapter features unpublished work in preparation for submission by David Jonathan Fulop Cohen, Natalie C. Li, Seva Ioussoufovitch, Vladislav Toronov, and Mamadou Diop.

3.1 Introduction

Near-infrared spectroscopy (NIRS) is a portable technology that uses safe (i.e., non-ionizing) near-infrared light to noninvasively probe living tissue¹. NIRS has high sensitivity to key biomarkers of brain health such as cerebral blood content and oxygenation², and is now widely used for neuromonitoring in both pre-clinical and clinical research³⁻⁵. Several NIRS methods have been developed over the years, but the most widely used devices are based on continuous-wave NIRS (CW-NIRS) technology. CW-NIRS is the simplest NIRS technology and is based on sending a constant beam of light into the tissue and monitoring for changes in its intensity^{6,7}. By using a CW-NIRS technique that can measure light attenuation at many wavelengths, rather than just a few (e.g., 2-3), the spectral features of the main light absorbers in the brain (e.g., water, oxy- and deoxyhemoglobin) can be leveraged to improve the accuracy of CW-NIRS. This approach is often called hyperspectral CW-NIRS and has been shown to provide reliable results in neonates^{8,9}; however, hyperspectral CW-NIRS neuromonitoring in adults remains a challenge due to significant contamination from their thicker skin and skull^{8,10}.

To mitigate this challenge, alternative NIRS methods that are more sensitive to the adult brain have been investigated, and the most advanced of such techniques are based on time-resolved NIRS (TR-NIRS)^{11,12}. In TR-NIRS neuromonitoring, short pulses of light are sent into the brain and the time it takes for the photons to arrive at the detector is precisely measured to generate a temporal point-spread function (TPSF). This allows for the differentiation of early-arriving photons – that have only passed through the

extracerebral layers (ECL; scalp, skull, and cerebrospinal fluid) – from late-arriving photons that are more likely to interrogate the brain. Several studies have demonstrated the superior brain sensitivity of TR-NIRS^{13–16}; however, analyzing TR-NIRS brain measurements is challenging, and measurements are often analyzed by assuming that the brain is a homogeneous medium^{17–19}. While such an approach may work in neonates, given their thin ECL, modelling the adult head as a homogeneous medium is obviously an oversimplification. Notably, when interrogating the brain non-invasively – with probes positioned on the scalp – NIRS measurements contain significant contribution from the ECL since light must travel through the skin (1.2-1.5 mm) and skull (~10 mm) before reaching the brain²⁰.

A simple, yet more accurate, approach to account for the ECL contribution is to divide the head into two compartments: brain and ECL¹². This permits the use of analytical solutions of light propagation in two-layer turbid media to analyze adult TR-NIRS brain measurements²¹. Nevertheless, traditional TR-NIRS analyses with a two-layer analytical solution are prone to crosstalk because of the increased number of fitting parameters (from three, for a homogeneous medium, to six); 4 parameters for the absorption and scattering coefficients of both layers, the thickness of the top layer, and an amplitude term that accounts for the unknown gain of the TR-NIRS system. We posit that acquiring TR-NIRS measurements at many wavelengths, similar to hyperspectral CW-NIRS, will allow for the use of the spectral features of the tissue chromophores to better constrain the fitting and reduce crosstalk.

To test this hypothesis, we developed a two-phase fitting algorithm – based on a two-layer analytical model of light propagation in diffuse media – that leverages the spectral features of oxy- and deoxyhemoglobin to estimate their concentration in the adult brain from hyperspectral TR-NIRS data acquired with probes positioned on the surface of the scalp. In the first phase of the analysis, all the TPSF curves are fit to the two-layer analytical model to estimate the absolute concentrations of oxy- and deoxyhemoglobin in the brain. These initial concentrations are used in the second phase to rapidly recover changes from subsequent measurements; this significantly reduces the computational time while accounting for the ECL contribution to the optical signal. The accuracy of the

algorithm was tested with *in silico* data from Monte-Carlo simulations of hyperspectral TR-NIRS in a model of the adult head obtained from a high-resolution 3D MRI image. The estimated concentrations were compared using Pearson's correlation against the known inputted parameters for validation.

3.2 Methods

The different steps of the two-phase fitting algorithm are depicted in Figure 3.1. The first phase uses data from two source-detector distances (2 and 3 cm) and the solution to the diffusion approximation (DA) for a two-layer semi-infinite medium to recover the *absolute* concentrations of oxy- and deoxyhemoglobin in the brain tissue (i.e., baseline concentrations)²¹. The second phase focuses on the rapid recovery of brain chromophore concentrations once their baseline values are known. As detailed in Section 2.2, the latter was accomplished by using data from the shorter source-detector distance (2 cm) to account for the ECL contamination of the absorption coefficient recovered using late-photon analysis of the tail of the TPSFs from the long source-detector distance (3 cm).

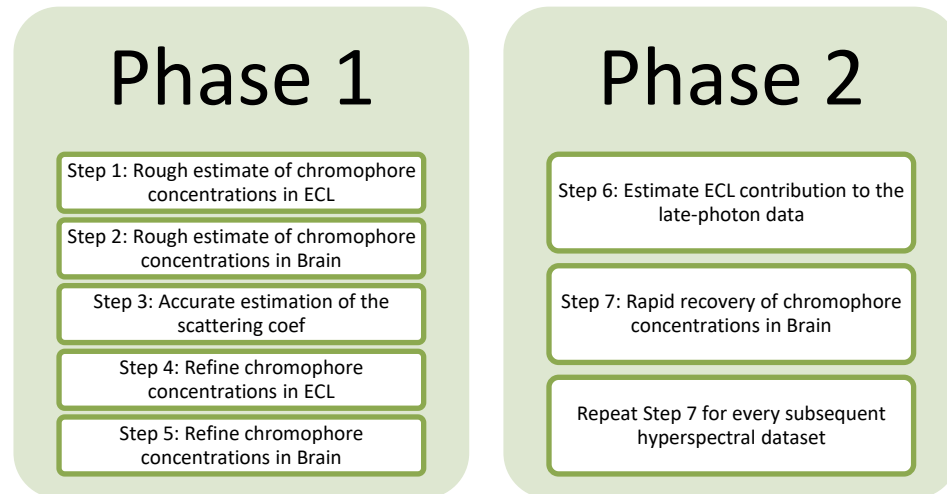


Figure 3.1: Flowchart of the two-phase hyperspectral TR-NIRS algorithm: Phase 1 revolves around the recovery of the absolute chromophore concentrations in the deep tissue (brain) using a two-layer analytical model of light transport in diffuse media. Phase 2 uses the absolute concentrations, estimated from Phase 1, to correct for the contribution of the ECL to late-arriving photon (from the tail of the TPSFs), allowing for quasi-real-time monitoring of cerebral blood content and oxygenation.

3.2.1 Phase 1: Estimation of baseline chromophore concentrations

There are typically six fitting parameters when TR-NIRS data are analyzed with a two-layer analytical model: the scattering and absorption coefficients in both layers, top layer thickness, and an amplitude term. Such a procedure is known to be prone to parameter crosstalk¹². To address this challenge, the algorithm introduced in this paper was designed to estimate the brain chromophore concentrations in five steps: i) rough estimation of the ECL chromophore concentrations, ii) rough estimation of the brain chromophore concentrations, iii) accurate estimation of the scattering coefficients, iv) refine the ECL concentrations, and v) refine the brain concentrations. By breaking the estimation of the baseline concentrations into five steps and establishing rough estimates of concentrations in the ECL and the brain, the algorithm reduces crosstalk and improves the robustness of the data analysis. Further, the algorithm leverages the spectral information provided by the hyperspectral TR-NIRS to constrain the fitting parameters, thereby further reducing crosstalk. The details of each step are provided in the following sections.

Step 1: Estimating the ECL oxy- and deoxyhemoglobin concentrations

The goal of this step is to calculate a rough estimate of the concentrations of oxy- and deoxyhemoglobin in the ECL using the shorter source-detector distance (2 cm). Note that these estimates are used as the initial guess of the ECL chromophore concentrations in the fitting of the 3 cm distance data with the two-layer analytical model; this provided an objective means of constraining the possible values of the ECL concentrations. At this source-detector distance the ECL dominates the NIRS signal¹⁰. The chromophore concentrations obtained by analyzing the data with a solution to the DA for a semi-infinite *homogeneous* medium will be heavily weighted toward the ECL values. The homogeneous fitting was implemented using a bounded least-squares regression method (*fminsearchbnd*²²) to minimize the difference between the one-layer DA and the TPSF for every wavelength. The TPSFs were fit from 50% of the max on the leading edge to 5% of the max after the peak. The three fitting parameters in the homogeneous fitting were the absorption coefficient, scattering coefficient, and amplitude. The 2 cm data were

first fit by allowing all three parameters to vary freely. Thereafter, the data were fit a second time – with the amplitude at all wavelengths fixed to the mean amplitude – to obtain an estimate of the wavelength-dependent scattering and absorption coefficients. The wavelength-dependent scattering coefficients recovered from this round were then fit with a model of Mie Scattering (Eq. 3.1) to further reduce the noise in the estimated scattering coefficient. Note that in Equation 3.1, a and b are fitting parameters which depend on the scattering of the tissue, λ is the wavelength in nm, and $\mu'_s(\lambda)$ is the wavelength-dependent reduced scattering coefficient (mm^{-1}). The data is fit a third time – with both the amplitude and scattering values fixed – to obtain an estimate of the wavelength dependent absorption coefficient (Figure 3.2).

$$\mu'_s(\lambda) = a\left(\frac{\lambda}{800}\right)^{-b} \quad (3.1)$$

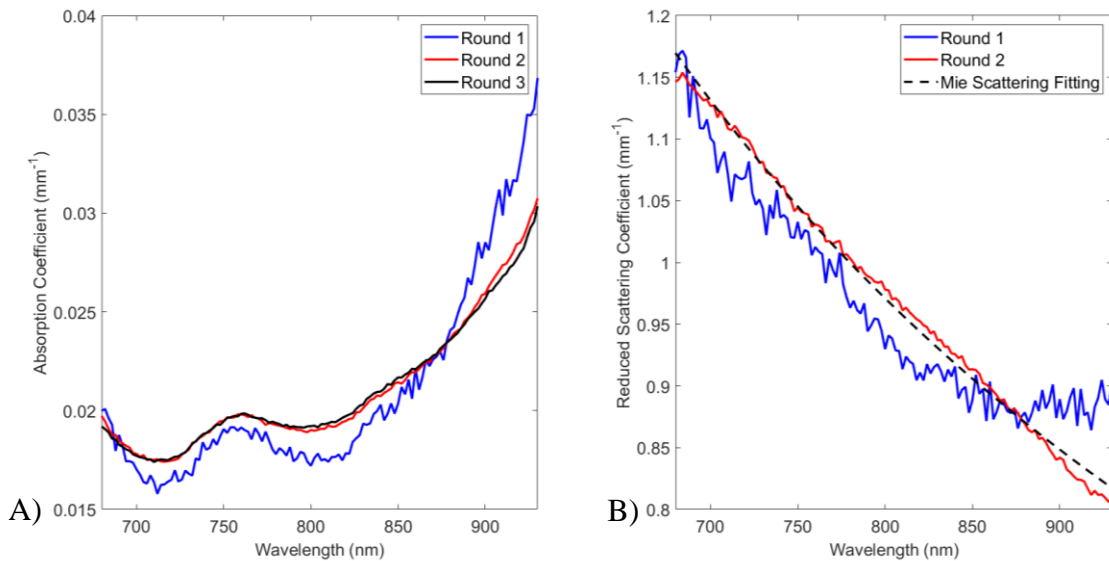


Figure 3.2: The outputs of the three rounds of homogenous fitting on the absorption (A) and scattering (B) coefficients.

The absorption coefficient of a tissue is dependent on its chromophore concentrations (C) and their wavelength-dependent extinction coefficients (ϵ), as shown in Equation 3.2:

$$\mu_a(\lambda) = \sum_i C_i \epsilon_i(\lambda) \quad (3.2)$$

This relationship can be used to recover the concentrations of oxy- (HbO₂) and deoxyhemoglobin (Hb) from the recovered absorption coefficients by solving a system of linear equations (Eq. 3.3):

$$\begin{aligned} \mu_a(\lambda_1) &= WF\varepsilon_{Water}(\lambda_1) + C_{Hb}\varepsilon_{Hb}(\lambda_1) + C_{HbO_2}\varepsilon_{HbO_2}(\lambda_1) \\ \mu_a(\lambda_2) &= WF\varepsilon_{Water}(\lambda_2) + C_{Hb}\varepsilon_{Hb}(\lambda_2) + C_{HbO_2}\varepsilon_{HbO_2}(\lambda_2) \\ &\vdots \\ \mu_a(\lambda_n) &= WF\varepsilon_{Water}(\lambda_n) + C_{Hb}\varepsilon_{Hb}(\lambda_n) + C_{HbO_2}\varepsilon_{HbO_2}(\lambda_n) \end{aligned} \quad (3.3)$$

where WF is the water fraction and is assumed to be 80%.

Step 2: Estimating the brain oxy- and deoxyhemoglobin concentrations

Step 2 establishes a preliminary estimate of the concentrations of oxy- and deoxyhemoglobin in the brain. One of the benefits of using TR-NIRS is that the tail of the TPSF is more sensitive to absorption. As such, late-photon analysis, also known as tail-fitting, can extract the absorption coefficient from the Reflectance (R) measurements (i.e., TPSFs) using Equation 3.4:

$$\mu_a(\lambda) = -\frac{\frac{\partial \ln(R(\lambda, t))}{\partial t}}{\frac{c}{n}} \quad (3.4)$$

where c is the speed of light in a vacuum, and n is the refractive index of the tissue. The TPSFs were fit between 5% and 1% of the max after the peak. All wavelengths from the long source-detector distance (3 cm) were analyzed using Equation 3.4, and the results were used to calculate the initial estimate of oxy- and deoxyhemoglobin concentrations in the brain. These concentrations are used to constrain the fitting of the 3 cm data against the two-layer analytical model.

Step 3: Scattering Coefficient Estimation

Step 3 calculates the wavelength-dependent scattering coefficient of the head as if it were a homogenous tissue. The wavelength-dependent scattering coefficient is recovered from the 3 cm source-detector distance using the process outlined in Section 3.2.1 up until using Equation 3.1 to fit the scattering data. The recovered scattering coefficients are

assigned to both tissues in the two-layer analytical fitting. Using a homogenous scattering instead of layer specific scattering had negligible impact on the final results, but reduced the complexity and fitting time.

Step 4: Refining the Extracerebral Concentrations

Step 4 refines the estimates of oxy- and deoxyhemoglobin concentration in the ECL using a two-layer analytical fitting²¹. For this step, the fitting parameters are the concentrations of oxy- and deoxyhemoglobin in both layers, the ECL thickness, and the amplitude of the TPSFs. The fitting algorithm calculates the wavelength-dependent absorption coefficients using Equation 3.2 before using those properties in the two-layer analytical model. A fitting algorithm built using the MATLAB function *fminsearchbnd* adjusts the fitting parameters to minimize the difference between the analytical models and the TPSFs for the full spectrum.

The brain concentrations of oxy- and deoxyhemoglobin are fixed to the values found in Step 3 for this fitting to reduce crosstalk between the tissues. The ECL concentrations found in Step 1 are assigned as the initial values and allowed to vary $\pm 50\%$, while the ECL thickness is assigned an initial value that is an average from the segmented MRI and can vary $\pm 10\%$. Finally, the amplitude is assigned an appropriate value based on the amplitude from the homogenous fitting in Step 3. The fitting is conducted on the 3 cm source-detector distance TPSFs from 50% of the maximum on the leading edge to 5% after the peak. The refined ECL concentrations and thickness are then used in Step 5 to refine the brain concentrations.

Step 5: Refining the Cerebral Concentrations

The final step of Phase 1 uses the two-layer fitting algorithm from step 4 to refine the estimates of cerebral oxy- and deoxyhemoglobin concentrations. The parameters recovered in Step 4 are fixed, and the cerebral concentrations of oxy- and deoxyhemoglobin can vary between 0 and 80 μM , with an initial value of 30 μM . The fit is conducted from 5% to 1% of the maximum on the tailing edge for all TPSFs from the 3 cm source-detector distance. The outputted concentrations are the baseline brain oxy- and

deoxyhemoglobin concentrations which will be used in Phase 2 for real-time brain monitoring.

3.2.2 Phase 2: Rapid Cerebral Concentration Recovery

Phase 2 corrects for the ECL contamination of the absorption coefficients recovered using late-photon analysis of the 3 cm source-detector distance by leveraging the absolute concentrations of oxy- and deoxyhemoglobin in the brain and ECL measured in Phase 1. Phase 2 has two steps: estimate ECL contribution to the absorption coefficient calculated using late-photon analysis (step 6), and rapid recovery of chromophore concentrations in the brain (step 7). Step 7 can be repeated for all subsequent dataset (i.e., spectral TPSFs), enabling quasi real-time monitoring. Note that while phase 1 uses a spectral resolution of 10 nm, phase 2 requires a spectral resolution of 2 nm between 680 nm and 930nm. The increased spectral resolution is required for the late-photon analysis due to the decrease in the signal-to-noise ratio (SNR) inherent to the late-arriving photons when compared to earlier arriving photons.

Step 6: Calculate Extracerebral Contribution

Step 6 calculates the contribution of the ECL to the absorption coefficients recovered from the late-photon analysis of the 3 cm TPSFs, allowing for correction of the contamination in subsequent hyperspectral TR-NIRS datasets. The absorption coefficient of a heterogeneous medium such as the adult head can be expressed as a weighted average of the absorption coefficients of its different compartments (Equation 3.5)²³:

$$\mu_{a_{LP}}(t, \lambda) = f_{ECL}(\lambda) \times \mu_{a_{ECL}}(t, \lambda) + f_{Brain}(\lambda) \times \mu_{a_{Brain}}(t, \lambda) \quad (3.5)$$

In this two-layer head model, the fraction of one tissue is written in terms of the other, in the form of $f_{Brain} = 1 - f_{ECL}$, where f_{Brain} is the fraction of the absorption coefficient coming from the brain tissue and f_{ECL} is the fraction from the ECL. The ECL fraction is a measure of the ECL contamination because the tissue of interest is the brain. Equation 3.5 can be rearranged to isolate the ECL fraction:

$$f_{ECL}(\lambda) = \frac{\mu_{a_{LP}}(t=0, \lambda) - \mu_{a_{Brain}}(t=0, \lambda)}{\mu_{a_{ECL}}(t=0, \lambda) - \mu_{a_{Brain}}(t=0, \lambda)} \quad (3.6)$$

where $\mu_{a_{Brain}}(t = 0, \lambda)$ and $\mu_{a_{ECL}}(t = 0, \lambda)$ are the initial brain and ECL absorption coefficients calculated using Equation 3.2 and the absolute concentrations recovered in Phase 1, and $\mu_{a_{LP}}(t = 0, \lambda)$ is the absorption coefficients recovered using late-photon analysis.

Step 7: Rapid Deep Tissue Recovery

Step 7 focuses on the rapid recovery of oxy- and deoxyhemoglobin concentrations. Equation 3.7 was established from Equation 3.5 and the percent change equation, and uses the baseline absorption coefficients in each layer, the ECL fraction, and the baseline late-photon absorption coefficient to remove the ECL contamination from subsequent late-photon derived absorption coefficient:

$$\mu_{a_{Brain}}(t, \lambda) = \mu_{a_{Brain}}(t = 0, \lambda) * \left(1 + \frac{\mu_{a_{LP}}(t, \lambda) - \mu_{a_{LP}}(t = 0, \lambda)}{\mu_{a_{LP}}(t = 0, \lambda) - f_{ECL}(\lambda) \mu_{a_{ECL}}(t = 0, \lambda)} \right) \quad (3.7)$$

The outputted absorption coefficients are the absorption coefficients of the brain.

Using Equation 3.2, assuming a water concentration of 80%, converts the wavelength-dependent absorption coefficient into concentrations of oxy- and deoxyhemoglobin in the brain. Cerebral oxygen saturation and total hemoglobin are then computed using Equations 3.8 and 3.9, respectively.

$$SO_2 = \frac{C_{HbO_2}}{C_{HbO_2} + C_{Hb}} \quad (3.8)$$

$$HbT = C_{HbO_2} + C_{Hb} \quad (3.9)$$

3.2.3 Validation

Validation was conducted *in silico* using Monte-Carlo Extreme (MCX) in a four-layer adult head model at various skin and brain oxygen saturations^{24,25}. Conducting the validation *in silico* instead of *in vivo* allows for better control of the experimental environment while maintaining realistic geometry and optical properties. To better mimic experimental conditions, we segmented a 3D MRI of an adult human head into four layers; skin, skull, cerebrospinal fluid (CSF), and brain tissue using 3DSlicer. Brain

oxygen saturation ranged from 40% to 82% in 2% increments, repeating each brain saturation three times with varying skin oxygen saturations (50%, 60%, and 70%). There is considerable debate concerning therapeutic thresholds for cerebral oxygen saturation; however, the proposed thresholds are typically absolute values of 40% to 50% or decreases of 20% to 30% from baseline^{26–29}. The simulated brain oxygen saturations were chosen to encompass these therapeutic thresholds. 126 simulations were conducted for each brain-skin pair, corresponding with the wavelengths ranging from 680 nm to 930 nm at 2 nm increments. In total, we completed 8,316 simulations for this validation. The source was positioned on the right side of the head with the detectors placed 2 cm and 3 cm towards the forehead, as shown in Figure 3.3. Each simulation had a total of 3 billion photons simulated with random seeds, ensuring realistic photon simulation with a good SNR at both detectors. All the optical properties for bone and CSF, as well as the scattering, anisotropic factor, and refractive index of the skin and brain, are from literature^{23,30}. Because the absorption coefficient is dependent on the chromophore concentration, we calculated the absorption coefficient of the skin and brain using Equation 3.2 for the beforementioned oxygen saturation ranges. The total hemoglobin concentrations in the skin and brain for all simulations were 12.4 μMol and 55 μMol , respectively^{31–34}.

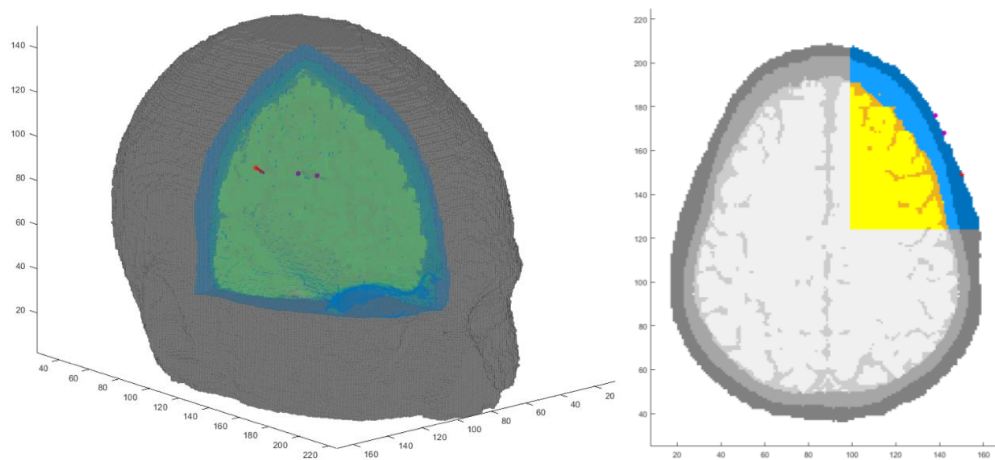


Figure 3.3: Adult head with source (red) and detectors (purple). The detectors are 2 cm and 3 cm away from the source. The tissues shown are skin (dark blue), skull (light blue), cerebrospinal fluid (orange), and brain (yellow). Due to GPU limitations, only the right

upper octant of the head was simulated, as shown above (grey tissues not simulated). The voxel size in the model is 1 mm^3 .

3.3 Results

The algorithm was validated using a hyperspectral dataset of 66 brain-skin oxygen saturation pairs. Accuracy and robustness of the method were evaluated by calculating the percent differences between the recovered oxy- and deoxyhemoglobin concentrations and the simulated values for the chromophore concentrations in the brain. Estimating the baseline chromophore concentrations from a full spectrum required an average of 4.7 minutes (282 seconds) for Phase 1, while Phase 2 only takes 0.22 seconds, representing a five orders of magnitude increase in speed (CPU: Intel Core i7-6800K @ 3.4GHz, using parallel computing with 6 cores, GPU: EVGA NVIDIA GEFORCE GTX 1080 8GB, RAM: 4 Kingston HyperX 32GB, totaling 128GB).

3.3.1 Phase 1: Baseline chromophore concentrations

Estimated absorption spectra and the corresponding expected spectra for four brain and three skin oxygen saturations are shown in Figure 3.4 to illustrate the qualitative similarity between the recovered and input spectra. As oxygen saturation decreases, the error between the recovered and inputted spectra increases; this trend is particularly obvious above 800 nm and is a result of the error in the recovered oxyhemoglobin concentration (Figure 3.4A). Figure 3.4B shows that the ECL oxygen saturation has minor impact on the accuracy of the brain parameter recovery. Further, the largest error occurred in the analysis of the 50% skin - 70% brain oxygen saturation simulation set and is the result of the method failing to accurately estimate the ECL thickness.

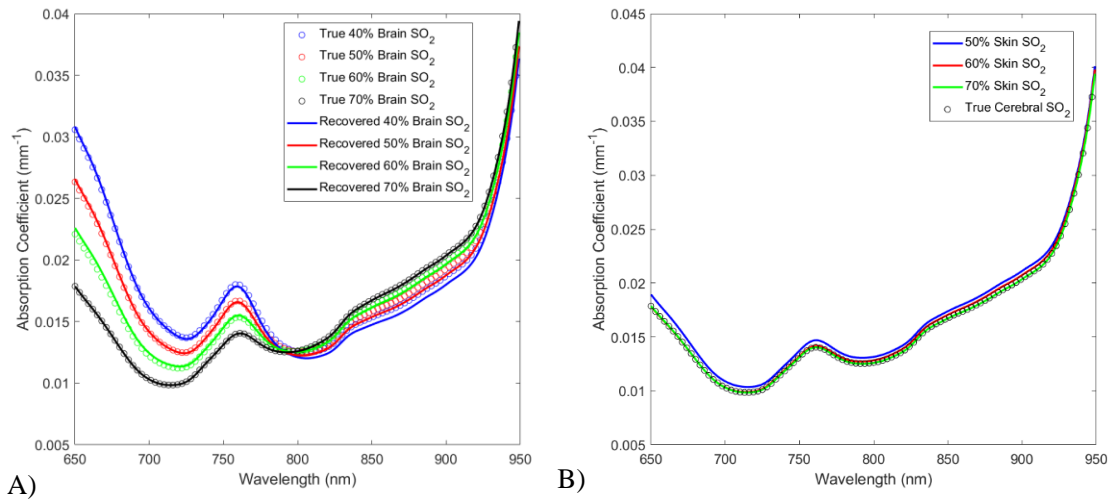


Figure 3.4: A) Recovered absorption coefficient from the 40%, 50%, 60%, and 70% brain oxygen saturations with skin oxygen saturation set to 70% and the true (inputted) values. B) Recovered and true (inputted) absorption coefficient spectra from 50%, 60%, and 70% skin oxygen saturation at 70% brain oxygen saturation.

The results of the quantitative analysis are shown in Figure 3.5. The mean (\pm standard deviation) percent difference between the recovered brain oxygen saturation and the true values is $2.4 \pm 2.1\%$, and the correlation coefficient between the true and recovered values is 0.9993. For total hemoglobin, the mean (\pm standard deviation) percent difference between the recovered concentration and the simulated concentration of $55 \mu\text{Mol}$ was $2.4 \pm 1.4\%$.

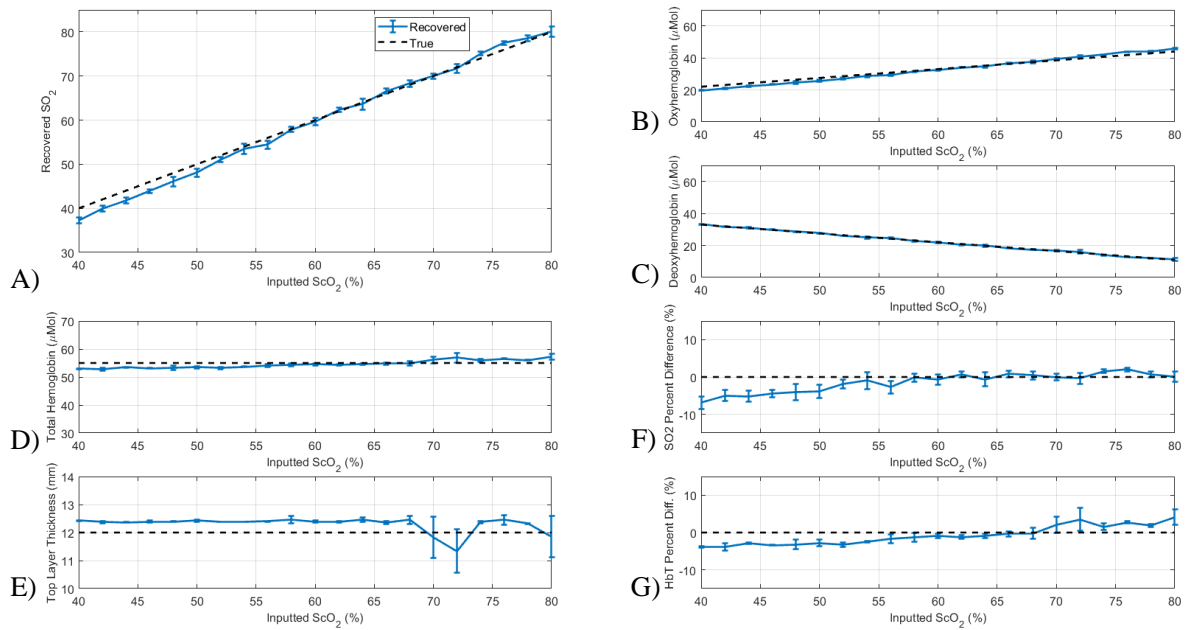


Figure 3.5: Results from Phase 1; for every cerebral oxygen saturation, three skin saturations were evaluated. A) The recovered brain SO₂, B) recovered oxyhemoglobin, C) recovered deoxyhemoglobin, and D) recovered total hemoglobin plotted versus the inputted ScO₂. The dotted black lines are the expected values. E) The recovered top layer thickness versus the inputted ScO₂. The true thickness of the ECL is approximately 12 mm. F) and G) show the percent difference for SO₂ and total hemoglobin.

The results are further improved when the ECL thickness is known (Figure 3.6). The mean (\pm standard deviation) percent difference between the recovered brain oxygen saturation and the true values becomes $1.3\pm 1.1\%$, and the correlation coefficient becomes 0.9996. For total hemoglobin, the mean (\pm standard deviation) percent difference becomes $1.7\pm 1.1\%$.

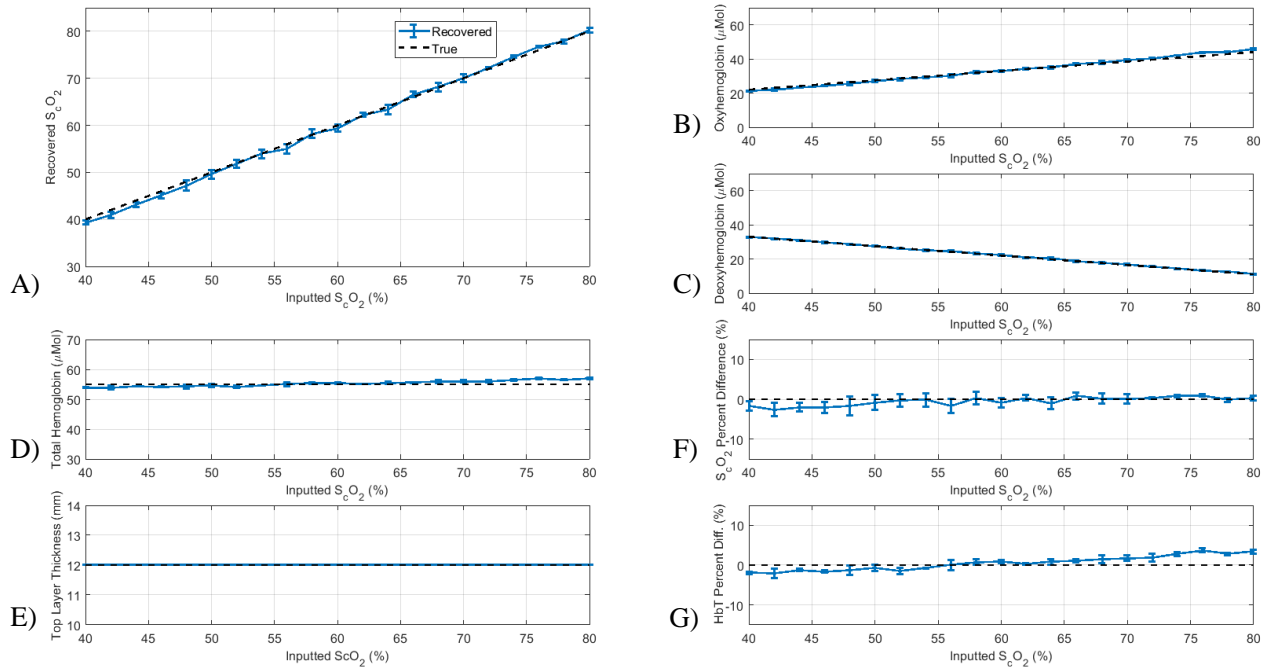


Figure 3.6: Results from Phase 1 with known ECL thickness; for every cerebral oxygen saturation, three skin saturations were evaluated. A) The recovered brain SO_2 , B) recovered oxyhemoglobin, C) recovered deoxyhemoglobin, and D) recovered total hemoglobin plotted versus the inputted ScO_2 . The dotted black lines are the expected values. E) and F) show the percent difference for SO_2 and total hemoglobin.

3.3.2 Phase 2: Active Monitoring

The recovered cerebral oxygen saturations from Phase 2 are shown in Figure 3.7. Once the baseline chromophore concentrations are estimated, the subsequent TR-NIRS spectra can be quickly analyzed to determine the cerebral blood content and oxygenation with high accuracy. Notably, the mean (\pm standard deviation) percent difference between the recovered and expected brain oxygen saturation and total hemoglobin are $1.5 \pm 1.1\%$ and $1.9 \pm 1.2\%$, respectively. Further, there is a very strong agreement between the recovered and simulated values with a Pearson's correlation coefficient of 0.999.

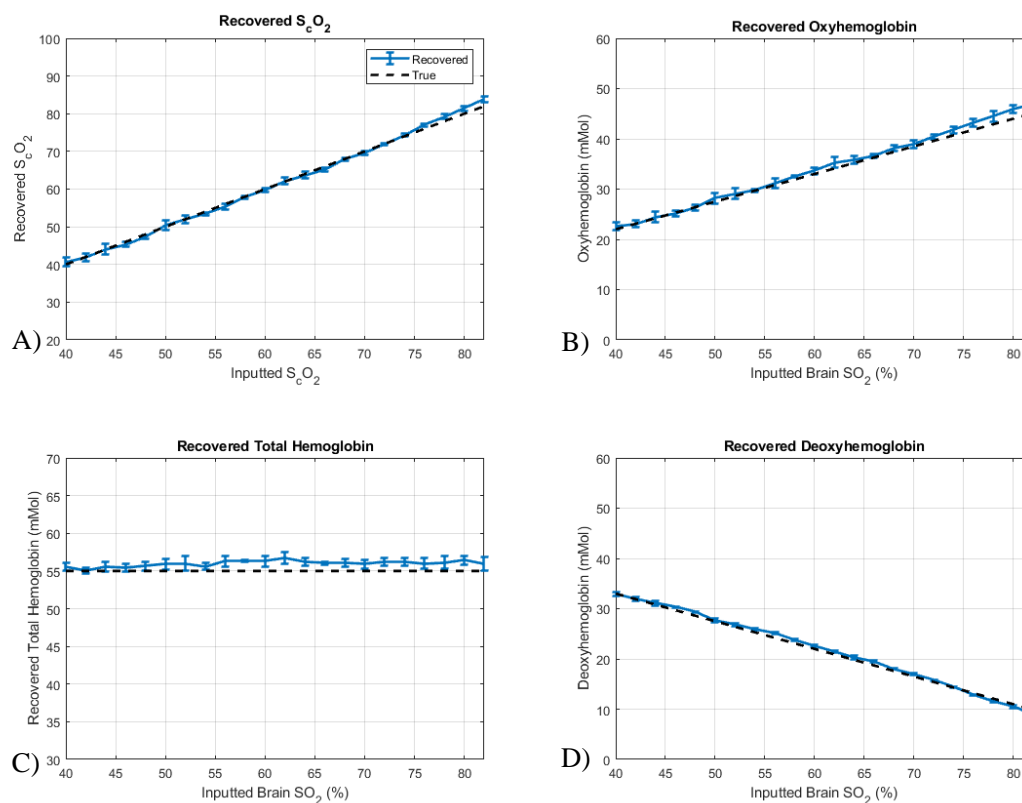


Figure 3.7: Results of Phase 2 analysis when using the concentrations estimated from Phase 1 for brain and skin oxygen saturation at 70%. A) The recovered brain S_cO_2 , B) recovered oxyhemoglobin, C) recovered deoxyhemoglobin, and D) recovered total hemoglobin plotted versus the inputted S_cO_2 . The dotted black lines are the expected values.

3.4 Discussion and Conclusion

Continuous bedside monitoring of cerebral blood content and oxygenation in adults requires both accuracy and speed for reliable real-time assessment. In this work, we developed a multi-step hyperspectral TR-NIRS data analysis algorithm that can quickly and reliably estimate cerebral concentrations of cerebral oxy- and deoxyhemoglobin. Both phases of the algorithm show high accuracy for estimating cerebral oxygen saturation and total hemoglobin concentration. While it takes 4.2 minutes to analyze a full TR-NIRS spectrum with Phase 1, which is too slow for real-time monitoring, it is

only needed once per subject to establish the baseline concentrations of oxy- and deoxyhemoglobin. Once this initial analysis is complete, all subsequent TR-NIRS spectra are analyzed using Phase 2, which takes only 0.22 seconds. This significant increase in speed would allow for quasi real-time neuromonitoring, while maintaining high accuracy. This approach could be used for cerebral monitoring in brain-at-risk patients such as those undergoing cardiac surgery³⁵.

One of the main challenges when using NIRS for adult neuromonitoring is significant signal contamination by the ECL. Previous studies have reported contamination from the ECL is responsible for between 52% and 88% of detector readings at 2 and 3cm, posing a significant issue when trying to obtain accurate estimates of brain chromophore concentrations^{10,36}. To investigate the potential confounding effects of changes in skin oxygen saturation on accuracy, three scalp blood oxygenations were simulated for every brain oxygen saturation. As shown in Figure 3.5 and Figure 3.7, the algorithm is capable of estimating cerebral oxygenation with high accuracy despite the change in scalp oxygen saturation. The reliability of the method under a variety of ECL conditions bodes well for its use in cardiac surgery and other high-risk for hypoxia procedures, as the brain is considered an index organ for oxygen supply to other organs; if the oxygen supply to the brain is compromised, it is likely that there is a larger systemic issue³⁷.

A major benefit of this method is that the exact ECL thickness does not need to be precisely known prior to analysis, as the fitting algorithm (in Step 4) estimates the ECL thickness within 10% of a prior estimate. During emergencies it is not always possible for the patient to get an MRI or CT; nevertheless, this method will allow them to receive intraoperative neuromonitoring. Additionally, not requiring the exact ECL thickness be known *a priori* reduces the specificity of where the probes must be placed; the minor variations that are present in the ECL thickness are accounted for by this algorithm.

To improve robustness and reduce crosstalk, we assumed a cerebral water concentration of 80%. Since the water concentrations in our simulations were 80% as well, we conducted additional analyses by assuming cerebral water concentration between 70% and 90% (true value 80%). The analysis revealed that an error of $\pm 10\%$ in the assumed

concentration of water has a negligible impact on the accuracy of the recovered oxy- and deoxyhemoglobin. In addition, given the water concentration in the brain is relative stable, assuming an 80% cerebral water concentration is a reasonable approach.

To reduce the computational burden, Phase 1 uses a sparse spectrum (every 10nm), instead of the dense spectrum (2 nm resolution) used for Phase 2. The sparse sampling had negligible effects on accuracy; however, accuracy dropped when the spectral sampling was further reduced (i.e., more than 10nm separation between consecutive wavelengths). Further, the algorithm can be modified to recover other chromophores by increasing the number of chromophores in the fitting parameters and changing the wavelength region of interest to cover the optical spectral range of the target chromophores. Notably, future work will include adapting the algorithm to monitor the redox state of Cytochrome C Oxidase (CCO), a key biomarker of brain health³⁸.

A potential limitation of this work is that we did not include the effects of the instrument response function (IRF). To analyze experimental data, the theoretical model of light propagation in a two-layer medium would be convolved with the measured IRF at each wavelength before fitting to the measured TR-NIRS data. While this correction has not yet been tested with this method, we believe this modification will have a negligible impact on the conclusions of this work, as similar corrections have previously been accomplished in our lab with minimal variations in the results³⁹. Another potential limitation of this work is that simulations were conducted on one octant of the full head due to GPU memory limitations. To assess the potential impact of this approach, we randomly picked 20 simulations and analyzed the photon trajectories. We found that no photons reached the volume boundaries; thus, it is reasonable to treat the volume used in the simulations as an optically semi-infinite medium.

An additional potential limitation is that all validations were conducted in a single geometry. While the oxygen saturations in the scalp and brain were varied extensively, the medium was kept constant throughout. However, we expect the algorithm to work with other ECL thicknesses since this parameter is estimated in Step 4 and thus does not

need to be perfectly known. Future work will include validation of the algorithm in tissue mimicking phantoms and in an animal model of an adult human head.

The multi-step hyperspectral TR-NIRS data analysis algorithm developed in this work allows for the quasi-real-time monitoring of the brain in adult subjects. The approach does not require the ECL thickness to be precisely known *a priori*, increasing the usability of this method. Combined with the rapid recovery of cerebral oxygen saturation and total hemoglobin content, this method will have valuable applications in a wide variety of settings for adult cerebral monitoring, including during cardiac surgery.

3.5 References

1. Denault AY, Shaaban-Ali M, Cournoyer A, Benkreira A, Mailhot T. Near-Infrared Spectroscopy. In: *Neuromonitoring Techniques*. Elsevier; 2018:179-233. doi:10.1016/B978-0-12-809915-5.00007-3
2. Durduran T, Zhou C, Buckley EM, et al. Optical measurement of cerebral hemodynamics and oxygen metabolism in neonates with congenital heart defects. *Journal of Biomedical Optics*. 2010;15(3):037004. doi:10.1117/1.3425884
3. Brown DW, Picot PA, Naeini JG, Springett R, Delpy DT, Lee TY. Quantitative near infrared spectroscopy measurement of cerebral hemodynamics in newborn piglets. *Pediatric Research*. 2002;51(5):564-570. doi:10.1203/00006450-200205000-00004
4. Lewis C, Parulkar SD, Bebawy J, Sherwani S, Hogue CW. Cerebral Neuromonitoring During Cardiac Surgery: A Critical Appraisal With an Emphasis on Near-Infrared Spectroscopy. *Journal of Cardiothoracic and Vascular Anesthesia*. 2018;32(5):2313-2322. doi:10.1053/j.jvca.2018.03.032
5. Goldman S, Sutter F, Ferdinand F, Trace C. Optimizing intraoperative cerebral oxygen delivery using noninvasive cerebral oximetry decreases the incidence of stroke for cardiac surgical patients. *Heart Surgery Forum*. 2004;7(5):392-397. doi:10.1532/HSF98.20041062
6. Wojtkiewicz S, Sawosz P, Milej D, Treszczanowicz J, Liebert A. Development of a Multidistance Continuous Wave Near-Infrared Spectroscopy Device with Frequency Coding. In: *Biomedical Optics 2014 (2014), Paper BM3A.24*. The Optical Society; 2014:BM3A.24. doi:10.1364/biomed.2014.bm3a.24
7. Scholkmann F, Kleiser S, Metz A, et al. A review on continuous wave functional near-infrared spectroscopy and imaging instrumentation and methodology. *NeuroImage*. Published online 2014:6-27. doi:10.1016/j.neuroimage.2013.05.004

8. Kewin M, Rajaram A, Milej D, et al. Evaluation of hyperspectral NIRS for quantitative measurements of tissue oxygen saturation by comparison to time-resolved NIRS. *Biomedical Optics Express*. 2019;10(9). doi:10.1364/BOE.10.004789
9. Rajaram A, Bale G, Kewin M, et al. Simultaneous monitoring of cerebral perfusion and cytochrome c oxidase by combining broadband near-infrared spectroscopy and diffuse correlation spectroscopy. *Biomedical Optics Express*. 2018;9(6):2588. doi:10.1364/boe.9.002588
10. Milej D, Abdalmalak A, Rajaram A, et al. Lawrence K. Direct assessment of extracerebral signal contamination on optical measurements of cerebral blood flow, oxygenation, and metabolism. *Neurophotonics*. 2020;7(04). doi:10.1117/1.nph.7.4.045002
11. Kacprzak M, Liebert A, Sawosz P, Żolek N, Maniewski R. Time-resolved optical imager for assessment of cerebral oxygenation. *Journal of Biomedical Optics*. 2007;12(3):034019. doi:10.1117/1.2743964
12. Gagnon L, Gauthier C, Hoge RD, Lesage F, Selb J, Boas DA. Double-layer estimation of intra- and extracerebral hemoglobin concentration with a time-resolved system. *Journal of Biomedical Optics*. 2008;13(5):054019. doi:10.1117/1.2982524
13. Selb J, Stott JJ, Franceschini MA, Sorensen AG, Boas DA. Improved sensitivity to cerebral hemodynamics during brain activation with a time-gated optical system: analytical model and experimental validation. *Journal of Biomedical Optics*. 2005;10(1):011013. doi:10.1117/1.1852553
14. Chance B, Leigh JS, Miyake H, et al. Comparison of time-resolved and -unresolved measurements of deoxyhemoglobin in brain. *Proceedings of the National Academy of Sciences of the United States of America*. 1988;85(14):4971-4975. doi:10.1073/pnas.85.14.4971
15. Steinbrink J, Fischer T, Kuppe H, et al. Relevance of depth resolution for cerebral blood flow monitoring by near-infrared spectroscopic bolus tracking during cardiopulmonary

- bypass. *Journal of Thoracic and Cardiovascular Surgery*. 2006;132(5):1172-1178.
doi:10.1016/j.jtcvs.2006.05.065
16. Liebert A, Wabnitz H, Grosenick D, Möller M, Macdonald R, Rinneberg H. Evaluation of optical properties of highly scattering media by moments of distributions of times of flight of photons. *Applied Optics*. 2003;42(28):5785. doi:10.1364/ao.42.005785
 17. Patterson MS, Chance B, Wilson BC. Time resolved reflectance and transmittance for the noninvasive measurement of tissue optical properties. *Applied Optics*. 1989;28(12):2331. doi:10.1364/ao.28.002331
 18. Baker WB, Balu R, He L, et al. Continuous non-invasive optical monitoring of cerebral blood flow and oxidative metabolism after acute brain injury. *Journal of Cerebral Blood Flow and Metabolism*. 2019;39(8):1469-1485. doi:10.1177/0271678X19846657
 19. Gerega A, Milej D, Weigl W, Kacprzak M, Liebert A. Multiwavelength time-resolved near-infrared spectroscopy of the adult head: assessment of intracerebral and extracerebral absorption changes. *Biomedical Optics Express*. 2018;9(7):2974. doi:10.1364/boe.9.002974
 20. Selb J, Ogden TM, Dubb J, Fang Q, Boas DA. Comparison of a layered slab and an atlas head model for Monte Carlo fitting of time-domain near-infrared spectroscopy data of the adult head. *Journal of Biomedical Optics*. 2014;19(1):016010. doi:10.1117/1.JBO.19.1.016010
 21. Kienle A, Glanzmann T, Wagnières G, van den Bergh H. Investigation of two-layered turbid media with time-resolved reflectance. *Applied Optics*. 1998;37(28):6852. doi:10.1364/ao.37.006852
 22. D'Errico J. fminsearchbnd, fminsearchcon. MATLAB Central File Exchange. Published 2021. Accessed May 5, 2021.
<https://www.mathworks.com/matlabcentral/fileexchange/8277-fminsearchbnd-fminsearchcon>

23. Jacques SL. Optical properties of biological tissues: A review. *Physics in Medicine and Biology*. 2013;58(11):R37. doi:10.1088/0031-9155/58/11/R37
24. Yan S, Fang Q. Hybrid mesh and voxel based Monte Carlo algorithm for accurate and efficient photon transport modeling in complex bio-tissues. *Biomedical Optics Express*. 2020;11(11):6262. doi:10.1364/boe.409468
25. Fang Q, Boas DA. Monte Carlo Simulation of Photon Migration in 3D Turbid Media Accelerated by Graphics Processing Units. *Optics Express*. 2009;17(22):20178. doi:10.1364/oe.17.020178
26. Hirofumi O, Otone E, Hiroshi I, et al. The effectiveness of regional cerebral oxygen saturation monitoring using near-infrared spectroscopy in carotid endarterectomy. *Journal of Clinical Neuroscience*. 2003;10(1):79-83. doi:10.1016/S0967-5868(02)00268-0
27. Samra SK, Dy EA, Welch K, Dorje P, Zelenock GB, Stanley JC. Evaluation of a cerebral oximeter as a monitor of cerebral ischemia during carotid endarterectomy. *Anesthesiology*. 2000;93(4):964-970. doi:10.1097/00000542-200010000-00015
28. Slater JP, Guarino T, Stack J, et al. Cerebral Oxygen Desaturation Predicts Cognitive Decline and Longer Hospital Stay After Cardiac Surgery. *Annals of Thoracic Surgery*. 2009;87(1):36-45. doi:10.1016/j.athoracsur.2008.08.070
29. Murkin JM, Adams SJ, Novick RJ, et al. Monitoring brain oxygen saturation during coronary bypass surgery: A randomized, prospective study. *Anesthesia and Analgesia*. 2007;104(1):51-58. doi:10.1213/01.ane.0000246814.29362.f4
30. Firbank M, Hiraoka M, Essenpreis M, Delpy DT. Measurement of the optical properties of the skull in the wavelength range 650-950 nm. *Physics in Medicine and Biology*. 1993;38(4):503-510. doi:10.1088/0031-9155/38/4/002
31. Kanti V, Bonzel A, Stroux A, et al. Postnatal maturation of skin barrier function in premature infants. *Skin Pharmacology and Physiology*. 2014;27(5):234-241. doi:10.1159/000354923

32. Farzam P, Buckley EM, Lin PY, et al. Shedding light on the neonatal brain: Probing cerebral hemodynamics by diffuse optical spectroscopic methods. *Scientific Reports*. 2017;7(1):1-10. doi:10.1038/s41598-017-15995-1
33. Luttkus A, Fengler TW, Friedmann W, Dudenhausen JW. Continuous monitoring of fetal oxygen saturation by pulse oximetry. *Obstetrics and Gynecology*. 1995;85(2):183-186. doi:10.1016/0029-7844(94)00353-F
34. Auger H, Bherer L, Boucher É, Hoge R, Lesage F, Dehaes M. Quantification of extra-cerebral and cerebral hemoglobin concentrations during physical exercise using time-domain near infrared spectroscopy. *Biomedical Optics Express*. 2016;7(10):3826. doi:10.1364/boe.7.003826
35. Nenna A, Barbato R, Greco SM, et al. Near-infrared spectroscopy in adult cardiac surgery: Between conflicting results and unexpected uses. *Journal of Geriatric Cardiology*. 2017;14(11):659-661. doi:10.11909/j.issn.1671-5411.2017.11.001
36. Selb J, Boas DA, Chan S-T, Evans KC, Buckley EM, Carp SA. Sensitivity of near-infrared spectroscopy and diffuse correlation spectroscopy to brain hemodynamics: simulations and experimental findings during hypercapnia. *Neurophotonics*. 2014;1(1):015005. doi:10.1117/1.NPh.1.1.015005
37. Murkin JM. Cerebral oximetry: Monitoring the brain as the index organ. *Anesthesiology*. 2011;114(1):12-13. doi:10.1097/ALN.0b013e3181fef5d2
38. Lange F, Dunne L, Hale L, Tachtsidis I. MAESTROS: A Multiwavelength Time-Domain NIRS System to Monitor Changes in Oxygenation and Oxidation State of Cytochrome-C-Oxidase. *IEEE Journal of Selected Topics in Quantum Electronics*. 2019;25(1). doi:10.1109/JSTQE.2018.2833205
39. Diop M, Tichauer KM, Elliott JT, Migueis M, Lee T-Y, Lawrence K st. Comparison of time-resolved and continuous-wave near-infrared techniques for measuring cerebral blood flow in piglets. *Journal of Biomedical Optics*. 2010;15(5):057004. doi:10.1117/1.3488626

Chapter 4

4 Conclusion

This final chapter reviews the primary objectives of this thesis and summarizes the major findings. The limitations of the research are presented, and potential solutions are explored. Finally, the future work and the potential impact of this research are discussed.

4.1 Research Objectives

Perioperative brain injury is a major complication during cardiac surgery, effecting between 6% and 62% of patients who undergo a CABG, depending on their risk factors¹⁻⁵. Cardiac operations can be extremely traumatic for brain tissue due to disruptions in blood flow and the dislodging of plaque from vessel walls, resulting from tissue and vessel manipulation^{6,7}. Cerebral injuries that occur during cardiac surgeries, such as stroke, seizure, and encephalopathy, often go undiagnosed until after the surgery has completed⁸. This is a major limitation as treatment is most effective when intervention is started as soon as the injury occurs, in hopes of preventing further damage. With over a million cardiac surgeries per year worldwide, there is a clear need for intraoperative brain monitoring⁹.

MRI, CT, and neurocognitive assessment are the best methods currently available for detecting brain injury¹⁰. Unfortunately, these methods are unsuitable for use in the OR due to their size (MRI), the radiation dose the patient would receive (CT), or the use of general anaesthesia reducing (or eliminating) the patient's response (neurocognitive assessment)¹⁰⁻¹³. Other options for intraoperative neuromonitoring include TCD ultrasound and EEGs, however these methods require a skilled interpreter to be used effectively and are user dependent¹⁴⁻¹⁶. A final alternative – and the one explored in this thesis – is the use of NIRS, which is capable of directly measuring cerebral oxygen saturation¹⁷⁻²¹.

As mentioned in Chapter 1, NIRS uses near-infrared light to non-invasively probe a tissue. TR-NIRS, the NIRS method explored throughout this thesis, creates photon time-

of-flight curves by recording how long the photons take to reach the detector^{18,22–24}. The shape of that curve is dependent on the optical properties of the tissues. Of note is the absorption coefficient, a measure of the absorption of light as it passes through a medium, which is directly related to the concentration of chromophores – light absorbing chemicals²⁵. NIRS can be used for neuromonitoring by measuring the concentrations of oxy- and deoxyhemoglobin in the brain, which are then used to calculate the cerebral oxygen saturation and total hemoglobin content^{26,27}.

A major limitation to using NIRS for adult patients is that the ECL is highly absorbing, leading to contamination of the optical signal²⁸. While this contamination can be negligible in neonates, the adult ECL can be over 1 cm thick in many regions resulting in the contamination dominating the optical signal^{28,29}. Additionally, the majority of commercial NIRS devices use CW-NIRS, focusing on tracking changes in oxygen saturation and total hemoglobin rather than absolute values³⁰. While monitoring changes is an important first step, the absolute and baseline values of these parameters are important factors in ensuring sufficient cerebral oxygen supply¹⁸.

The focus of this thesis was to develop a method which can quickly and accurately recover absolute adult ScO₂ and total hemoglobin concentration from TR-NIRS data, despite the ECL contamination. This was accomplished by addressing our two primary objectives:

1. Develop a reliable two-layer fitting approach for few-wavelength TR-NIRS to recover ScO₂ and total hemoglobin in adults using a single source-detector pair.
2. Develop a hyperspectral TR-NIRS fitting algorithm using a two-layer approach and late-photon analysis to achieve quasi real-time adult neuromonitoring with high accuracy.

4.2 Summary of Chapters

4.2.1 Chapter 2: Estimating adult cerebral oxygen saturation from time-resolved near-infrared spectroscopy measurements with few discrete wavelengths at a single source-detector distance

Chapter 2 focused on developing a reliable method for estimating ScO₂ and total hemoglobin content from adult subjects. This method fits few-wavelength TR-NIRS data from a single source-detector pair against a two-layer analytical model of light propagation in highly scattering medium, to recover the concentrations of oxy- and deoxyhemoglobin. The wavelengths used were 680 nm, 750 nm, 800 nm, and 830 nm. This method was validated using Monte Carlo simulations in a realistic head model with three scalp oxygen saturations (50%, 60%, and 70%) and ScO₂ ranging from 40% to 80% in 2% increments. The recovered ScO₂ had a mean \pm standard deviation percent difference of $2.31 \pm 2.93\%$ from inputted values, and cerebral total hemoglobin was recovered with a percent difference of $2.94 \pm 3.47\%$. The correlation coefficient for the recovered ScO₂ versus the inputted values was 0.9987. The high accuracy of this few-wavelength method showed that it is possible to overcome the ECL contamination in adult subjects by dividing the head into two layers (ELC and brain).

4.2.2 Chapter 3: Fast Estimation of Adult Cerebral Oxygen Saturation and Total Hemoglobin using Hyperspectral Time-Resolved Near-Infrared Spectroscopy

Chapter 3 focused on developing a quasi-real-time method for accurate estimation of adult ScO₂ and total hemoglobin using Hyperspectral TR-NIRS. The method uses a two-phase approach; Phase 1 establishes the baseline cerebral hemoglobin concentrations using a two-layer approach, while Phase 2 conducts a rapid concentration recovery by using late-photon analysis and leveraging the calculated ECL contamination fraction. This method was also validated using Monte Carlo simulations in a four-layer adult head model. The mean (\pm standard deviation) percent difference between the recovered ScO₂ and the inputted values for Phases 1 and 2 were $2.4 \pm 2.1\%$ and $1.5 \pm 1.1\%$, respectively. Their respective correlation coefficients are 0.9993 and 0.9990. Similarly, the mean

(\pm standard deviation) percent difference between the recovered total hemoglobin concentrations and the inputted values for Phases 1 and 2 were $2.4\pm 1.4\%$ and $1.7\pm 1.1\%$, respectively. This two-phase method enables quasi real-time monitoring once the baseline has been established; Phase 1 requires 4.2 minutes to analyze a full Hyperspectral TR-NIRS spectrum, while Phase 2 only requires 0.22 seconds to complete the same analysis.

4.3 Limitations

There are several limitations to this work. The first one is that analysis methods were validated *in silico* rather than *in vivo*. Choosing an *in silico* method for validation allowed us to compare our estimated values against the true baseline, granted us greater control of the experimental environment, and allowed for a greater number of cerebral oxygen saturations to be tested as is often difficult to precisely control the ScO₂ *in vivo*. However, the Monte Carlo simulations do not have an Instrument Response Function (IRF), which characterizes the temporal dispersion of the TR-NIRS system³¹. Monte Carlo simulations treat all simulated photons as if they have been released using a delta function; that is to say, they are all instantaneously released at the same timepoint. In an *in vivo* setting the measured distribution of time-of-flight (DTOF) is in fact a convolution of the TPSF with the IRF²². There are two options available to correct for the IRF: either removing the IRF from the DTOF, or accounting for the IRF in the analytical model. The former of these options is extremely difficult (involving a deconvolution)²², thus the second option is preferred^{18,23}. While this has not yet been tested with our method, we do not expect any major challenge in implementing it in an *in vivo* setting by convolving the two-layer analytical model with the IRF to fit the measured DTOFs.

Another potential limitation common to both studies is that while the ScO₂ and scalp oxygenation were varied extensively, the validations were conducted in a single head geometry. Despite this, we predict both methods presented in this work will work with other head geometries; the method presented in Chapter 2 requires the ECL thickness to be known *a priori*, while the method from Chapter 3 is able to tolerate error in the ECL

estimation because it solves for the ECL thickness as part of the algorithm. As will be discussed in Section 4.4, conducting *in vivo* validations will address this limitation.

A final potential limitation is that the simulations used only one octant of the full head due to GPU memory limitations. To assess the potential impact of this limitation on the validation, we sampled the photon trajectories of 20 simulations and found that no detected photons reached the volume boundaries (where the head was truncated). This showed that the head is sufficiently large that it is reasonable to treat the volume as a semi-infinite medium, and thus this should not impact the validity of the results.

4.4 Future Work

The results of this work are promising but require further validation before these techniques can be deployed in the clinic for patient bedside monitoring. The next step in the validation process will be to test the chromophore recovery capabilities of the methods presented in Chapter 2 and 3 on a tissue mimicking phantom. The phantom will likely be a two-layer box with a top layer thickness comparable to that of an adult ECL³². Both layers will contain intralipid, to mimic the scattering properties of tissue, and blood of various oxygen saturations.

Following the successful completion of the phantom study, both methods will be further validated using an animal model. A juvenile pig will be used because at that stage of development it will have an ECL thickness comparable to that of an adult human³³. The methods from Chapters 2 and 3 will be compared to measurements acquired with a NIRS device whose probes will be placed directly on the pig's brain. Should these ScO₂ recovery methods continue to perform as well as they have *in silico*, they will be deployed in the operating room to monitor patient ScO₂ and total hemoglobin.

4.5 Conclusion

The high prevalence of patients who undergo cardiac surgery suffering a perioperative neurological complication shows the clear need for intraoperative neuromonitoring^{1-5,34}. The methods presented in this thesis show great promise for the quick and accurate estimation of ScO₂ and total hemoglobin concentrations in adult patients from TR-NIRS

data. The methods presented have been validated *in silico*, revealing that they are robust and capable of accurately recovering cerebral concentrations of oxy- and deoxyhemoglobin in adults. While the two methods show comparable accuracy, the more advanced method in Chapter 3 has the added benefit of not requiring the exact ECL thickness to be known *a priori*, which provides greater flexibility. With further development we believe these methods could be utilized during cardiac surgeries to inform physicians of neurological injuries as they occur, allowing doctors to administer treatment as soon as possible and improve patient outcomes^{8,35-37}.

4.6 References

1. Roach GW, Kanchuger M, Mangano CM, et al. Adverse Cerebral Outcomes after Coronary Bypass Surgery. *New England Journal of Medicine*. 1996;335(25):1857-1864. doi:10.1056/NEJM199612193352501
2. Bendszus M, Reents W, Franke D, et al. Brain damage after coronary artery bypass grafting. *Archives of Neurology*. 2002;59(7):1090-1095. doi:10.1001/archneur.59.7.1090
3. Floyd TF, Shah PN, Price CC, et al. Clinically Silent Cerebral Ischemic Events After Cardiac Surgery: Their Incidence, Regional Vascular Occurrence, and Procedural Dependence. *Annals of Thoracic Surgery*. 2006;81(6):2160-2166. doi:10.1016/j.athoracsur.2006.01.080
4. Djaiani G, Fedorko L, Borger M, et al. Mild to moderate atheromatous disease of the thoracic aorta and new ischemic brain lesions after conventional coronary artery bypass graft surgery. *Stroke; a journal of cerebral circulation*. 2004;35(9). doi:10.1161/01.str.0000138783.63858.62
5. Knipp SC, Matatko N, Wilhelm H, et al. Evaluation of brain injury after coronary artery bypass grafting. A prospective study using neuropsychological assessment and diffusion-weighted magnetic resonance imaging. In: *European Journal of Cardio-Thoracic Surgery*. Vol 25. Oxford Academic; 2004:791-800. doi:10.1016/j.ejcts.2004.02.012
6. Hogue CW, Gottesman RF, Stearns J. *Mechanisms of Cerebral Injury from Cardiac Surgery*. Vol 24.; 2008.
7. Hogue CW, Palin CA, Arrowsmith JE. Cardiopulmonary Bypass Management and Neurologic Outcomes: An Evidence-Based Appraisal of Current Practices. *Anesthesia & Analgesia*. 2006;103(1):21-37. doi:10.1213/01.ANE.0000220035.82989.79

8. Zhou Z bin, Meng L, Gelb AW, Lee R, Huang WQ. Cerebral ischemia during surgery: An overview. *Journal of Biomedical Research*. 2016;30(2):83-87. doi:10.7555/JBR.30.20150126
9. Veluz JS, Leary MC. Cerebrovascular Complications of Cardiac Surgery. In: *Primer on Cerebrovascular Diseases: Second Edition*. Elsevier Inc.; 2017:650-655. doi:10.1016/B978-0-12-803058-5.00126-0
10. Ahonen J, Salmenperä M. Brain injury after adult cardiac surgery. *Acta Anaesthesiologica Scandinavica*. 2004;48(1):4-19. doi:10.1111/j.1399-6576.2004.00275.x
11. Harvey PD. Clinical applications of neuropsychological assessment. *Dialogues in Clinical Neuroscience*. 2012;14(1):91-99. doi:10.31887/dcns.2012.14.1/pharvey
12. Wityk RJ, Goldsborough MA, Hillis A, et al. Diffusion- and perfusion-weighted brain magnetic resonance imaging in patients with neurologic complications after cardiac surgery. *Archives of Neurology*. 2001;58(4):571-576. doi:10.1001/archneur.58.4.571
13. Smith-Bindman R, Lipson J, Marcus R, et al. Radiation dose associated with common computed tomography examinations and the associated lifetime attributable risk of cancer. *Archives of Internal Medicine*. 2009;169(22):2078-2086. doi:10.1001/archinternmed.2009.427
14. Grocott HP. Monitoring the brain in cardiac surgery - an evolving area for research. *Anaesthesia*. 2012;67(3):216-219. doi:10.1111/j.1365-2044.2012.07076.x
15. Grocott HP, Amory DW, Croughwell ND, Newman MF. Transcranial Doppler blood flow velocity versus ¹³³Xe clearance cerebral blood flow during mild hypothermic cardiopulmonary bypass. *Journal of Clinical Monitoring and Computing*. 1998;14(1):35-39. doi:10.1023/A:1007493422230

16. Lewis C, Parulkar SD, Bebawy J, Sherwani S, Hogue CW. Cerebral Neuromonitoring During Cardiac Surgery: A Critical Appraisal With an Emphasis on Near-Infrared Spectroscopy. *Journal of Cardiothoracic and Vascular Anesthesia*. 2018;32(5):2313-2322. doi:10.1053/j.jvca.2018.03.032
17. Diop M, Elliott JT, Tichauer KM, Lee TY, Lawrence K. A broadband continuous-wave multichannel near-infrared system for measuring regional cerebral blood flow and oxygen consumption in newborn piglets. *Review of Scientific Instruments*. 2009;80(5):054302. doi:10.1063/1.3123347
18. Kewin M, Rajaram A, Milej D, et al. Evaluation of hyperspectral NIRS for quantitative measurements of tissue oxygen saturation by comparison to time-resolved NIRS. *Biomedical Optics Express*. 2019;10(9). doi:10.1364/BOE.10.004789
19. Brown DW, Hadway J, Lee TY. Near-Infrared Spectroscopy Measurement of Oxygen Extraction Fraction and Cerebral Metabolic Rate of Oxygen in Newborn Piglets. *Pediatric Research*. 2003;54(6):861-867. doi:10.1203/01.PDR.0000090928.93045.BE
20. Brown DW, Picot PA, Naeini JG, Springett R, Delpy DT, Lee TY. Quantitative near infrared spectroscopy measurement of cerebral hemodynamics in newborn piglets. *Pediatric Research*. 2002;51(5):564-570. doi:10.1203/00006450-200205000-00004
21. Tichauer KM, Hadway JA, Lee TY, Lawrence KS. Measurement of cerebral oxidative metabolism with near-infrared spectroscopy: A validation study. *Journal of Cerebral Blood Flow and Metabolism*. 2006;26(5):722-730. doi:10.1038/sj.jcbfm.9600230
22. Diop M, Lawrence K. Deconvolution method for recovering the photon time-of-flight distribution from time-resolved measurements. *Optics Letters*. 2012;37(12):2358. doi:10.1364/ol.37.002358

23. Milej D, Abdalmalak A, McLachlan P, Diop M, Liebert A, St. Lawrence Keith. Subtraction-based approach for enhancing the depth sensitivity of time-resolved NIRS. *Biomedical Optics Express*. 2016;7(11):4514. doi:10.1364/boe.7.004514
24. McManus R, Ioussoufovitch S, Froats E, St Lawrence K, van Uum S, Diop M. Dynamic response of cerebral blood flow to insulin-induced hypoglycemia. *Scientific Reports*. 2020;10(1):1-10. doi:10.1038/s41598-020-77626-6
25. Jacques SL. Optical properties of biological tissues: A review. *Physics in Medicine and Biology*. 2013;58(11):R37. doi:10.1088/0031-9155/58/11/R37
26. Rajaram A, Bale G, Kewin M, et al. Simultaneous monitoring of cerebral perfusion and cytochrome c oxidase by combining broadband near-infrared spectroscopy and diffuse correlation spectroscopy. *Biomedical Optics Express*. 2018;9(6):2588. doi:10.1364/boe.9.002588
27. Mawdsley L, Abayomi N, Rajaram A, et al. Using near infrared spectroscopy and diffuse correlation spectroscopy to determine the microvascular effects of phenylephrine in vivo. In: Fantini S, Taroni P, eds. *Optical Tomography and Spectroscopy of Tissue XIV*. Vol 11639. SPIE; 2021:31. doi:10.1117/12.2577237
28. Milej D, Abdalmalak A, Rajaram A, St. Lawrence K. Direct assessment of extracerebral signal contamination on optical measurements of cerebral blood flow, oxygenation, and metabolism. *Neurophotonics*. 2020;7(04). doi:10.1117/1.nph.7.4.045002
29. Selb J, Ogden TM, Dubb J, Fang Q, Boas DA. Comparison of a layered slab and an atlas head model for Monte Carlo fitting of time-domain near-infrared spectroscopy data of the adult head. *Journal of Biomedical Optics*. 2014;19(1):016010. doi:10.1117/1.JBO.19.1.016010
30. Denault AY, Shaaban-Ali M, Cournoyer A, Benkreira A, Mailhot T. Near-Infrared Spectroscopy. In: *Neuromonitoring Techniques*. Elsevier; 2018:179-233. doi:10.1016/B978-0-12-809915-5.00007-3

31. Pirovano I, Re R, Candeo A, Contini D, Torricelli A, Spinelli L. Instrument response function acquisition in reflectance geometry for time-resolved diffuse optical measurements. *Biomedical Optics Express*. 2020;11(1):240. doi:10.1364/boe.380996
32. Diop M, Lawrence K. Improving the depth sensitivity of time-resolved measurements by extracting the distribution of times-of-flight. *Biomedical Optics Express*. 2013;4(3):447. doi:10.1364/boe.4.000447
33. Elliott JT, Diop M, Tichauer KM, Lee T-Y, Lawrence K. Quantitative measurement of cerebral blood flow in a juvenile porcine model by depth-resolved near-infrared spectroscopy. *Journal of Biomedical Optics*. 2010;15(3):037014. doi:10.1117/1.3449579
34. Mangano DT, Mangano CM. Perioperative Stroke, Encephalopathy, and Central Nervous System Dysfunction. *Journal of Intensive Care Medicine*. 1997;12(3):148-160. doi:10.1177/088506669701200305
35. A Neurosurgeon's Guide to Stroke Symptoms, Treatment and Prevention. Accessed April 28, 2021. <https://www.aans.org/en/Patients/Neurosurgical-Conditions-and-Treatments/Stroke>
36. Hood R, Budd A, Sorond FA, Hogue CW. Peri-operative neurological complications. *Anaesthesia*. 2018;73:67-75. doi:10.1111/anae.14142
37. Mashour GA, Woodrum DT, Avidan MS. Neurological complications of surgery and anaesthesia. *British Journal of Anaesthesia*. 2015;114(2):194-203. doi:10.1093/bja/aeu296

Appendices

Appendix A: Permission for Reproduction of Scientific Articles

Copyright Agreement for the Proceedings of SPIE (Chapter 2)

RE: Permission to use copyrighted material in a Masters Thesis



Katie Sinclair [REDACTED]
2021-05-07 5:19 PM



To: David Jonathan Fulop Cohen

Dear David,

Thank you for seeking permission from SPIE to reprint material from our publications. SPIE shares the copyright with you, so as author you retain the right to reproduce your paper in part or in whole.

Publisher's permission is hereby granted under the following conditions:

- (1) the material to be used has appeared in our publication without credit or acknowledgment to another source; and
- (2) you credit the original SPIE publication. Include the authors' names, title of paper, volume title, SPIE volume number, and year of publication in your credit statement.

Best wishes on your thesis! Please let me know if I may be of any further assistance.

Best,
Katie Sinclair
Editorial Assistant, Publications
SPIE – the international society for optics and photonics



SPIE.

From: David Jonathan Fulop Cohen [REDACTED]
Sent: Tuesday, May 4, 2021 2:40 PM
To: [REDACTED]
Subject: Permission to use copyrighted material in a Masters Thesis

Hello,

I am a University of Western Ontario graduate student completing my Masters thesis in Medical Biophysics. My thesis will be available in full-text on the internet for reference, study and/or copy. Except in situations where a thesis is under embargo or restriction, the electronic version will be accessible through the Western Libraries web pages, the Library's web catalogue, and also through web search engines. I will also be granting Library and Archives Canada and ProQuest/UMI a non-exclusive license to reproduce, loan, distribute, or sell single copies of my thesis by any means and in any form or format. These rights will in no way restrict republication of the material in any other form by you or by others authorized by you.

I would like permission to allow inclusion of the following material in my thesis:

David Jonathan Fulop Cohen, Natalie C. Li, Mamadou Diop, "Estimating adult cerebral oxygen saturation from time-resolved near-infrared spectroscopy measurements with few discrete wavelengths at a single source-detector distance," Proc. SPIE 11639, Optical Tomography and Spectroscopy of Tissue XIV, 116390U (5 March 2021); <https://doi.org/10.1117/12.2577340>

The material will be attributed through a citation.

Please confirm in writing or by email that these arrangements meet with your approval.

Sincerely,
David Jonathan Fulop Cohen

Appendix B: Curriculum Vitae

Name:	David Jonathan Fulop Cohen
Post-secondary Education and Degrees:	<p>The University of Western Ontario London, Ontario, Canada 2019-2021 M.Sc.</p> <p>The University of Western Ontario London, Ontario, Canada 2015-2019 B.MSc.</p>
Honours and Awards:	<p>Natural Sciences and Engineering Council (NSERC) Canadian Graduate Scholarship - Masters (CGS-M) 2020-2021 <i>National (\$17,500)</i></p> <p>The Government of Ontario Ontario Graduate Scholarship 2020-2021 <i>Provincial (\$15,000 – Declined)</i></p> <p>The Government of Ontario Queen Elizabeth II Graduate Scholarship in Science and Technology 2019-2020 <i>Provincial (\$15,000)</i></p> <p>Western Graduate Scholarship (WGRS) Western University 2019-2021 <i>Institutional (\$10,000)</i></p> <p>Global Undergraduate Awards Regional Winner for US and Canada – Medical Sciences Category 2019 <i>International</i></p> <p>Medical Biophysics Undergraduate Research Day First Place Oral Presentation 2019 <i>Institutional</i></p> <p>Natural Sciences and Engineering Council (NSERC) Undergraduate Summer Research Award (USRA) 2018 and 2019 <i>Institutional</i></p>

The University of Western Ontario
 Dean's Honor List
 2015-2019
Institutional

The University of Western Ontario
 The Western Scholarship of Excellence Award
 2015-2016
Institutional

**Related Work
 Experience**

Teaching Assistant
 The University of Western Ontario
*MEDBIO 3507G: Analysis of Oxygen Transport in Biological
 Systems*
 2020-2021

Research Assistant
 The University of Western Ontario
Translational Biophotonics Lab
 2018-2019

**Committees and
 Memberships**

Student Representative
 Medical Biophysics Graduate Student Association
 2020-2021

Co-Chair
 Medical Biophysics Academic Mentorship Program
 2020-2021

Planning Committee
 Let's Talk Cancer
 2019-2021

Member
 The Optical Society (OSA)
 2019-2021

Planning Committee
 Medical Biophysics Research Symposium
 2018-2021

Student Representative
 Biophysics Network of Students (BONeS)
 2017-2019

Conference Proceedings and Publications:

Cohen, David J. F., Li, N. C., & Diop, M. (2021). Estimating adult cerebral oxygen saturation from time-resolved near-infrared spectroscopy measurements with few discrete wavelengths at a single source-detector distance. In S. Fantini & P. Taroni (Eds.), *Optical Tomography and Spectroscopy of Tissue XIV* (Vol. 11639, Issue 5, p. 26). SPIE. <https://doi.org/10.1117/12.2577340>

Abdalmalak, A., Milej, D., **Cohen, D. J. F.**, Anazodo, U., Ssali, T., Diop, M., Owen, A. M., & St. Lawrence, K. (2020). Using fMRI to investigate the potential cause of inverse oxygenation reported in fNIRS studies of motor imagery. *Neuroscience Letters*, 714, 134607. <https://doi.org/10.1016/j.neulet.2019.134607>

Cohen, David J. F., & Diop, M. (2020). Late-photons hyperspectral near-infrared spectroscopy improves the sensitivity to cerebral oxygenation in adults. *Optics InfoBase Conference Papers, Part F176-BRAIN-2020*, BTh3C.2. <https://doi.org/10.1364/BRAIN.2020.BTh3C.2>

Cohen, David J. F. (2019). Monte-Carlo Simulations of Near-infrared Light Propagation in the Adult Human Head. *2019 Undergraduate Awards*. https://ir.lib.uwo.ca/undergradawards_2019/8

Cohen, David J. F., & Diop, M. (2019). In silico investigation of near-infrared light propagation in the joints of the human hand. In S. Fantini, P. Taroni, B. J. Tromberg, & E. M. Sevick-Muraca (Eds.), *Optical Tomography and Spectroscopy of Tissue XIII* (Vol. 10874, p. 78). SPIE. <https://doi.org/10.1117/12.2508933>

Conference Presentations:

Cohen, David J. F., Li, N. C., & Diop, M. Estimating adult cerebral oxygen saturation from time-resolved near-infrared spectroscopy measurements with few discrete wavelengths at a single source-detector distance. *SPIE Photonics West 2021*. Oral Presentation. Virtual.

Cohen, David J. F., & Diop, M. Late-photons hyperspectral near-infrared spectroscopy improves the sensitivity to cerebral oxygenation in adults. *Biophotonics Congress: Biomedical Optics 2020*. Oral Presentation. Virtual.

Cohen, David J. F. Monte-Carlo Simulations of Near-infrared Light Propagation in the Adult Human Head. *Global Undergraduate Awards Summit 2019*. Oral Presentation. Dublin, Ireland.

Cohen, David J. F., & Diop, M. *In Silico* Investigation of Near-Infrared Light Propagation in the Human Wrist Joint. *SPIE Photonics West 2019*. Poster Presentation. San Francisco, California, United States of America.

Cohen, David J. F. An analysis of Near-infrared Light Propagation in the Adult Human Head. *Global Undergraduate Awards Summit 2019*. Oral Presentation. Dublin, Ireland.

Cohen, David J. F. Monte-Carlo Simulations of Near-infrared Light Propagation in the Adult Human Head. *Medical Biophysics Undergraduate Research Day*. Oral Presentation. London, Ontario, Canada.

Adbalmalak, A., Milej, D., **Cohen, David J. F.**, Ssali, T., Diop M., Owen, A. M., & St. Lawrence, K. Are partial volume errors the cause of inverse oxygenation during fNIRS studies of motor-imagery? *fNIRS 2018*. Oral Presentation. Tokyo, Japan.

Cohen, David J. F., Tse, J., Holdsworth, D., & Diop, M. In Silico Investigation of Near-Infrared Photon Propagation in Bones. *Canadian Bone and Joint Conference 2018*. Poster Presentation. London, Ontario, Canada.